# Chemical Structure and Upconversion Enhancement of NaYF$_4$ Nanocrystals and Nanosheets

## Christian Clarke

### BSc (Hons)

A thesis submitted in partial fulfilment of requirements for the degree of Doctor of Philosophy

School of Mathematical and Physical Sciences

University of Technology Sydney

July 2020

# Declaration of Authorship

I, Christian Clarke, declare that the work in this thesis has not previously been submitted for a degree nor has it been submitted as part of the requirements for a degree except as fully acknowledged within the text.

I also declare that the work presented is my own and the thesis has been written by me. Any help that I have received in my research work and the preparation of the thesis has been acknowledged. In addition, I declare that all information sources and literature used are indicated in the thesis.

Signature of Candidate: Production Note:
Signature removed prior to publication.

Date: 2/7/2020

# Acknowledgements

Finally, to my friends and family Alex Gee, Ling Ling Chan, Allen Zhou, Matt Cappadonna, Ziqing Miriam Du and my parents Anthony Clarke and Kathryn Clarke, thank you for your unconditional support throughout this time.

# Contents

# List of Figures

# List of Tables

# List of Acronyms

AFM          Atomic Force Microscopy

CCD          Charged Couple Device

CET          Cooperative Energy Transfer

CS          Core Shell

DFT          Density Functional Theory

EDS          Energy-dispersive X-ray Spectroscopy

| | |
|---|---|
| EMU | Energy Migration Upconversion |
| ESA | Excited State Absorption |
| ETU | Energy Transfer Upconversion |
| FFT | Fast Fourier Transform |
| HTCP | High Temperature Co-Precipitation |
| ICP-AES | Inductively Coupled Plasma Atomic Emission Spectroscopy |
| ICP-MS | Inductively Coupled Plasma Mass Spectrometry |
| IMFP | Inelastic Mean Free Path |
| LSPR | Local Surface Plasmon Resonance |
| ML | Monolayer |
| NaYF$_4$ | Sodium Yttrium Fluoride |
| NEXAFS | Near Edge X-ray Adsorption Fine Structure |
| NIR | Near-infrared |
| OA | Oleic Acid |
| ODE | 1-Octadecene |
| OM | Oleylamine |
| PA | Photon Avalanche |
| PDOS | Partial Density of States |
| PEY | Partial Electron Yield |
| PL | Photoluminescence |
| PMMA | Poly(methyl methacrylate) |
| RE | Rare Earth |
| SCCM | Standard Cubic Centimetre per Minute |
| SEM | Scanning Electron Microscopy |
| SLTD | Solid-Liquid-Thermal-Decomposition |
| SPAD | Single Photon Avalanche Diode |
| TCD | Thermal Co-Decomposition |

| | |
|---|---|
| TEA | Triethylamine |
| TEM | Transmission Electron Microscopy |
| TEY | Total Electron Yield |
| TFY | Total Fluorescent Yield |
| UCNP | Upconversion Nanoparticle |
| UV-Vis | Ultraviolet Visible |
| VASP | Vienna Ab initio Simulation Package |
| XRD | X-ray Powder Diffraction |
| XPS | X-ray Photoelectron Spectroscopy |

# List of Publications

## Journal Publications

1.      Xiaoxue Xu, **Christian Clarke**, Chenshuo Ma, Gilberto Casillas, Minakshi Das, Ming Guan, Deming Liu, Li Wang, Anton Tadich, Yi Du, Cuong Ton-That, Dayong Jin. "*Depth-profiling of $Yb^{3+}$ sensitizer ions in $NaYF_4$ upconversion nanoparticles*" 2017, Nanoscale 9 (23) 7719-7726. [1]

2.      Jiajia Zhou, Shihui Wen, Jiayan Liao, **Christian Clarke**, Sherif Abdulkader Tawfik, Wei Ren, Chao Mi, Fan Wang, Dayong Jin. "*Activation of the surface dark-layer to enhance upconversion in a thermal field*" 2018, Nature Photonics 12 (3), 154. [2]

3.      **Christian Clarke**, Deming Liu, Fan Wang, Yongtao Liu, Chaohao Chen, Cuong Ton-That, Xiaoxue Xu, Dayong Jin. "*Large-scale dewetting assembly of gold nanoparticles for plasmonic enhanced upconversion nanoparticles*" 2018, Nanoscale 10 (14), 6270-6276. [3]

4.     Wei Ren, Gungun Lin, **Christian Clarke**, Jiajia Zhou, Dayong Jin. "*Optical Nanomaterials and Enabling Technologies for High-Security-Level Anticounterfeiting*" 2019, Advanced Materials 32(18), 1901430. [4]

5.     Du Ziqing, Abhishek Gupta, **Christian Clarke**, Matt Cappadona, David Clases, Deming Liu, Zhuoqing Yang, Shawan Karan, William Price, Xiaoxue Xu. "*Porous upconversion nanostructures as bimodal biomedical imaging contrast agents*" 2020, Journal of Physical Chemistry C, 124, 22, 12168–12174. [5]

6.     Noushin Nasiri, **Christian Clarke**. "*Nanostructured Chemiresistive Gas Sensors for Medical Applications*" 2019, Sensors 19.3: 462. [6]

7.     Noushin Nasiri, **Christian Clarke**. "*Nanostructured Gas Sensors for Medical and Health Applications: Low to High Dimensional Materials*" 2019, Biosensors 9(1), 43. [7]

(1 - 5 are closely related to my PhD program)

## Oral Presentations

Xiaoxue Xu, **Christian Clarke**, Chenshuo Ma, Gilberto Casillas, Minakshi Das, Ming Guan, Deming Liu, Li Wang, Anton Tadich, Yi Du, Cuong Ton-That, Dayong Jin. "Depth-profiling of $Yb^{3+}$ sensitizer ions in $NaYF_4$ upconversion nanoparticles" ICONN 2018, Wollongong, February 2018.

# Abstract

The ability of lanthanide ions to convert lower energy photons to higher energy photons through the process known as upconversion presents as an opportunity to overcome limitations in sensitivity, efficiency and selectivity present for a wide variety of applications such as bio-imaging, photovoltaics and anti-counterfeiting.

Sodium Yttrium Fluoride ($NaYF_4$) is an inorganic insulator with low phonon energy ($360$ cm$^{-1}$ $\approx 45$ meV), wide band gap ($8.5$ eV) and high chemical stability. These properties make $NaYF_4$ an ideal optical host crystal for lanthanide dopants to produce upconversion nanoparticles (UCNPs). The shape, size and structure of UCNPs can be highly controlled allowing them to be tailored to the requirements of specific applications.

Key challenges of concentration quenching and low quantum yield still confront UCNPs before their potential can be fully realised. Accordingly, enhancing the efficiency of UCNPs and their brightness has been the focus of numerous studies. In this project these challenges facing UCNPs are addressed by material characterisation and optimisation based on a comprehensive understanding of the chemical and optical properties of the material.

Firstly, synchrotron-based XPS and NEXAFS along with EDS and ICP-MS characterisation techniques were employed on a range of UCNPs with sizes from 13 nm - 51 nm and different lanthanide ($Ln^{3+}$) concentrations of 20% - 60% to determine how lanthanides are distributed within each nanocrystal. This analysis reveals a radial gradient distribution of $Yb^{3+}$ and $Tb^{3+}$ exists from the core to the surface of the $NaYF_4$ UCNPs, regardless of their size or lanthanide dopant concentration. The active core structure of this distribution was then systematically correlated to the optical properties of UCNPs with different sizes revealing a trend of increased optical upconversion emission efficiency by smaller sized UCNPs.

Secondly, surface plasmon coupling was achieved between core-shell UCNPs and dewetted gold nanoparticles by precisely growing $NaYF_4$ shell coatings of varied thickness from 5 nm - 15 nm around the optically active core UCNPs. The local

surface plasmon of the gold nanoparticles could be controlled and coupled with the internal transitions of the $Er^{3+}$ ions. Combining these inert shelled UCNPs and plasmonic gold nanoparticles produced a shell thickness dependent enhancement with five times enhanced upconversion emission from the core-shell UCNPs with a shell thickness of 10 nm.

Thirdly, bulk $NaYF_4$ microparticles were successfully exfoliated to make 2D $NaYF_4$ nanosheets. By using a simple soft exfoliation method without the need for intensive ultrasonication atomically flat optically active nanosheets down to a single monolayer were produced. Extensive characterisation of the nanosheets supported by DFT calculations reveals a phase change and 1 eV band gap reduction for this new 2D material compared to the bulk.

Finally, in an appendix to demonstrate a massive three orders of magnitude increase in emission from ultra-small $Tm^{3+}$ doped UCNPs an anti-counterfeiting mark was designed and fabricated. This enhancement only occurs at high temperature as activated surface phonons become efficient energy pathways for energy migration. The temperature dependence of the enhancement allowed the anti-counterfeiting mark to be temperature responsive.

# Chapter 1

# Introduction to NaYF$_4$ UCNPs

## 1.1        Motivation

By combining photon sensitizers (i.e., Nd$^{3+}$ and Yb$^{3+}$) and activators ions (i.e., Tm$^{3+}$ and Er$^{3+}$) into an energy transfer network within a single nanoparticle, lanthanide doped upconversion nanoparticles (UCNPs) can upconvert low energy near infrared radiation into higher energy visible emission [8]. This property originates from the electron transitions of the ladder like energy levels of the lanthanides' fourth partially filled 4f$^n$ shell (n = 0 - 14) shown in Figure 1.1. This electronic structure allows excitation within a lanthanide ion to occur through charge transfer, 4f-5d transitions and 4f-4f transitions. Upconversion in lanthanides results from the 4f-4f transitions resulting in advantageous properties including both tuneable multicolour emission under single-wavelength excitation and long μs emission lifetimes with high chemical/photo stabilities [9-11].
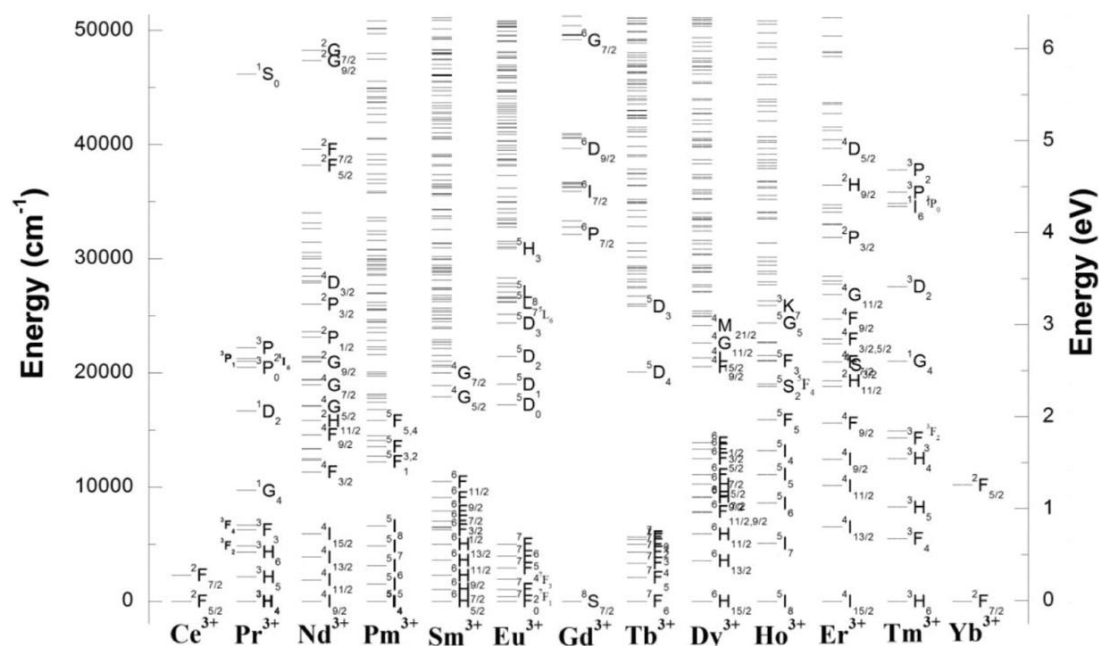


**Figure 1.1** Free 4f$^n$ energy levels of trivalent lanthanide ions. Reproduced from [12].

The choice of host material to dope with these lanthanide sensitizers and activators greatly effects the upconversion process and so considering requirements like lattice mismatch, spatial position, dopant distance and phonon energy is crucial [13]. At its most fundamental the host material should maximise radiative emission and minimise non-radiative losses. One key host property to achieve this is the phonon energy the intrinsic vibrational energy of the lattice. As phonons are directly engaged with the relaxation pathways of lanthanides it is ideal to use a host material having as low phonon energy as possible.

As highlighted in Table 1.1 halides have a low phonon energy but are highly hydroscopic which is detrimental to lanthanide emission processes. Oxides have closely matching ionic radii with lanthanide ions promoting doping but have a much higher phonon energy. Semiconductor sulphides are also possible for use as a host material with low phonon energies, yet issues with inhomogeneous doping from substantial lattice mismatch restrict them for use an alternative. Glasses have low phonon energies without any of the previous issues of the other host materials however they have restricted morphology at the nanoscale. Regardless, macroscale lanthanide doped glasses are widely used in optical fiber fabrication for medical diagnostics, optical sensors and communications [14, 15].

Finally, there are fluoride materials which are the most ideal and popular host material for lanthanide UCNPs [16]. Apart from their low phonon energy, optical transparency and wide band gap compared to other potential host materials it is the closely matching ionic size of $Li^+$, $Na^+$, $K^+$, $Ca^{2+}$, $Sr^{2+}$, $Ba^{2+}$, $Sc^{3+}$, $Y^{3+}$, $La^{3+}$ and $Lu^{3+}$ etc based fluoride crystals, to the trivalent lanthanides, that distinguishes them, minimising defects and stress within the crystal.

Table 1.1 Comparison of upconversion host materials' phonon energy and lanthanide stability [17, 18].

| Host Material | Phonon Energy ($cm^{-1}$) | Lanthanide Stability |
|---|---|---|
| Chlorides/Bromides/Iodides ($CsPbX_3$, $K_2LaX_5$) (X = Cl,Br,I) | < 300 | Hygroscopic |

| | | |
|---|---|---|
| Oxides (Y$_2$O$_3$, YVO$_4$) | > 500 | Matching ionic radius |
| Sulphides (ZnS, MoS$_2$, Y$_2$O$_2$S) | > 400 | Inhomogeneous doping |
| Glasses (Chalcogenide, Fluoride) | > 400 | Limited morphology |
| Fluorides (NaYF$_4$, LuF$_3$) | < 400 | Matching ionic radius |

For fluoride host UCNPs, NaYF$_4$ is commonly reported as one of the most efficient hosts for upconversion luminescence. By doping NaYF$_4$ with 18% - 25% of Yb$^{3+}$ sensitizers and 0.3% - 2% of Tm$^{3+}$ or Er$^{3+}$ activators bright emission under low laser excitation can be generated [19-22], while higher Yb$^{3+}$ ($\leq$ 100%) [23-26] and Tm$^{3+}$ or Er$^{3+}$ concentrations ($\leq$ 20%) are able to achieve super bright emissions under intense focused laser excitation [27, 28].

The focus of current upconversion research is based on developing UCNPs, in the size range of 5 nm - 100 nm for applications in bioimaging [29-32], biosensing [33-35], drug delivery [36, 37], cancer therapy [38], anti-counterfeiting [39], photovoltaics [40], 3D volumetric displays [41, 42] and super resolution nanoscopy applications [43, 44]. However, even the most efficient β-NaYF$_4$ crystal phase has a low quantum yield ($\varphi \ll 5\%$) [45]. This value is an order of magnitude lower than the theoretical value for two photon upconversion ($\varphi = 50\%$) [21], limiting the practical applications of UCNPs.

To mitigate this problem numerous methods have been applied to enhance UCNP emission which can be assigned to the six categories of host lattice manipulation, surface passivation, energy transfer modulation, broadband sensitization, surface plasmon coupling and photonic crystal engineering [46]. All methods within these categories of enhancement are based and rely on an understanding of the chemical and optical properties of the upconversion nanocrystals.

## 1.2      Aims of Research

The aim of this thesis is to design, simulate, fabricate and characterise $NaYF_4$ in order to optimise its upconversion properties while investigating the chemical, optical and morphological properties. Then demonstrate the enhanced $NaYF_4$ UCNPs in tailored applications.

The specific aims are summarized below:

- Determine the concentration gradient of lanthanide dopants within UCNPs for a better understanding of internal chemical structure.
- Investigate the application of host lattice manipulation, surface plasmon coupling, surface passivation and broadband sensitization enhancement methods on UCNP properties to overcome the low emission efficiency.

## 1.3      Thesis Structure

This thesis is divided into seven sections and an appendix:

- Chapter 1: A concise introduction to $NaYF_4$ UCNPs to provide background and context for this project and thesis chapters.
- Chapter 2: Comprehensive review of $NaYF_4$ for use as a host material for upconversion.
- Chapter 3: Overview of the experimental materials and methods used in this project.
- Chapter 4: Synchrotron depth profiling characterisation of UCNPs.
- Chapter 5: Investigation into the plasmonic enhancement of UCNPs.
- Chapter 6: Fabrication and properties of 2D $NaYF_4$ nanosheets.
- Chapter 7: A conclusion and outlook for future work.
- Appendix: A proof of concept application of phononic UCNP enhancement for anti-counterfeiting.

# Chapter 2

# NaYF₄: An Efficient Material for Upconversion

This chapter reviews the chemical, optical and morphological properties of NaYF₄ UCNPs and the current methods that can be used to enhance the optical upconversion properties.

## 2.1      Fundamental Properties

### 2.1.1      Crystal Structure

The hexagonal beta (β) phase and cubic alpha (α) phase are the two most common crystal structures for NaYF₄ UCNPs. The parameters of these phase structures are summarised in Table 2.1. As shown in Figure 2.1 the crystal structure for both phases clearly shows that upon doping it is the $Y^{3+}$ ion with its closely matching ionic radius that is substituted in the lattice for the trivalent lanthanide ions [47]. However, it is also clear that the α-NaYF₄ has the $Na^+$ and lanthanide cations randomly distributed in the lattice. This distribution explains the denser distribution of vibrational modes for the α phase of the crystal. These vibrational modes tend to become non-harmonic hence the higher maximum phonon energy of this phase. Phonon energy transitions can act as a source of non-radiative energy loss causing the excited lanthanide ions to relax to lower energy levels or ground state without radiative emission. Therefore, in contrast, the β-phase with a more ordered structure and sparser distribution of vibrational modes resulting in a lower phonon energy allows less non-radiative

relaxation with excited electrons diminishing more effectively [16]. These differences explain why the photoluminescence quantum yield in the β-phase is higher and justifies the upconversion emission intensity of β-NaYF$_4$ UCNPs being one order of magnitude higher than that of α-NaYF$_4$ UCNPs [48].

**Table 2.1** Summary of crystal structure parameters for β-NaYF$_4$ and α-NaYF$_4$.

| Parameter | Hexagonal (β) | Cubic (α) |
|---|---|---|
| Lattice constants [49] | | |
| a (Å) | 5.96 | 5.51 |
| c (Å) | 3.51 | - |
| Maximum phonon energy (cm$^{-1}$) [50] | 360 | 400 |
| Band gap (eV) [51, 52] | 8.5 | 8.0 |
| Dimorphic phase change (°C) [50] | α to β >300<br>β to α >500 | |
| Polymorphic transition (°C) [53] | 705 | |
| Melting point (°C) [53] | 950 | |
| Molecular weight (g/mol) vs Diameter (nm) [49] | $10^6$ - $10^8$ = 10 - 50 | |
| Refractive index [54] | 1.47 @ λ = 589 nm | |
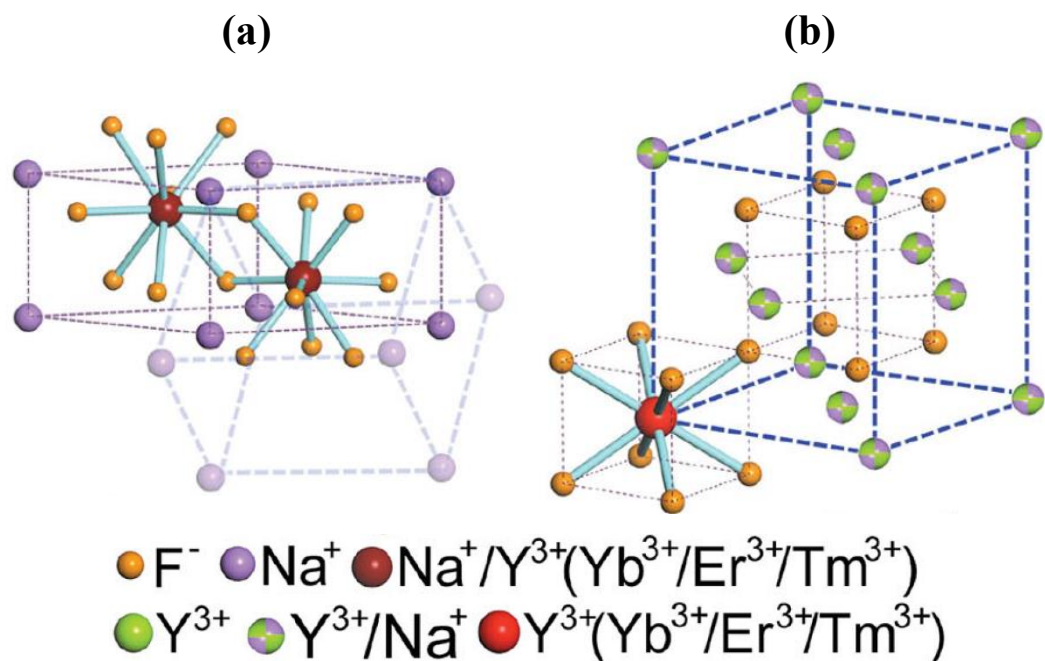
**Figure 2.1** Crystal lattice model for hexagonal β-NaYF$_4$ (a) and cubic α-NaYF$_4$ (b). Reproduced from [48].

## 2.1.2    Morphology

NaYF$_4$ nanocrystal synthesis methods allow for a wide variety of UCNP morphologies with exact control of size and shape.    The most widely used upconversion synthesis procedures are variations of the thermal co-decomposition (TCD) and high temperature co-precipitation (HTCP) methods [55, 56]. However, these methods result in less than 100 mg of final product, this single issue leading to the related problem of reproducibility with unwanted variation between different batches of synthesised UCNPs caused from the time-consuming, long reaction and multistep nature of both the HTCP and TCD methods. This outstanding challenge has been attempted by many groups. Yao et al. reported a facile hydrothermal method to produce NaYF$_4$ on a large-scale [57]. The method produced uniform high quality upconversion particles that were demonstrated in an anti-counterfeiting application through screen-printing however only 500 mg was produced of the greater than 1 µm

sized plate shaped particles. You et al. has recently demonstrated the ability of their solid-liquid-thermal-decomposition (SLTD) method that allows for true large-scale synthesis of uniform $\beta$-NaYF$_4$ UCNPs [58]. The SLTD method is a combination of the HTCP and TCD methods with the addition of NaHF$_2$ a low-cost reagent acting as the precursor for the source of fluoride and sodium. During the high temperature reaction NaHF$_2$ decomposes to NaF and HF which then reacts with liquid phase rare earth (RE) compounds in oleic acid/1-octadecene (OA/ODE) causing the nucleation and growth of Ln$^{3+}$-NaREF$_4$ UCNPs. The method allows for the adjustment of the reaction temperature and addition of sodium acetate to tune important staple characteristics of UCNPs such as crystal structure, particle size and morphology. Most impressively the SLTD method allows from a single one-pot synthesis a record 63 g production of 24 nm $\beta$-NaYF$_4$ UCNPs.

Smaller UCNPs are preferred for biological applications to allow for more efficient cell uptake and clearance leading many to pursue the synthesis of increasingly smaller UCNPs [59]. A common method to produce smaller UCNPs is to control the reaction temperature and time. Using the TCD synthesis method and prolonging the reaction time smaller $\alpha$-NaYF$_4$ UCNPs from 14 nm - 5 nm can be achieved or similarly by increasing the reaction temperature a wide range of $\beta$-NaYF$_4$ UCNPs from 20 nm - 300 nm are also possible [60]. Additionally, fine control of size is available from manipulation of synthesis surfactants. During synthesis the surface of the UCNP becomes capped with long chain hydrocarbon surfactants that are present in the reaction stabilizing and preventing aggregation of the nanoparticles an example in Figure 2.2 displays the commonly used surfactant OA. The size of $\beta$-NaYF$_4$ can be precisely controlled from 50 nm - 30 nm via an increase in the concentration of OA [61] and even sub 10 nm $\beta$-NaYF$_4$ UCNPs are possible using both oleylamine (OM) and OA [62].
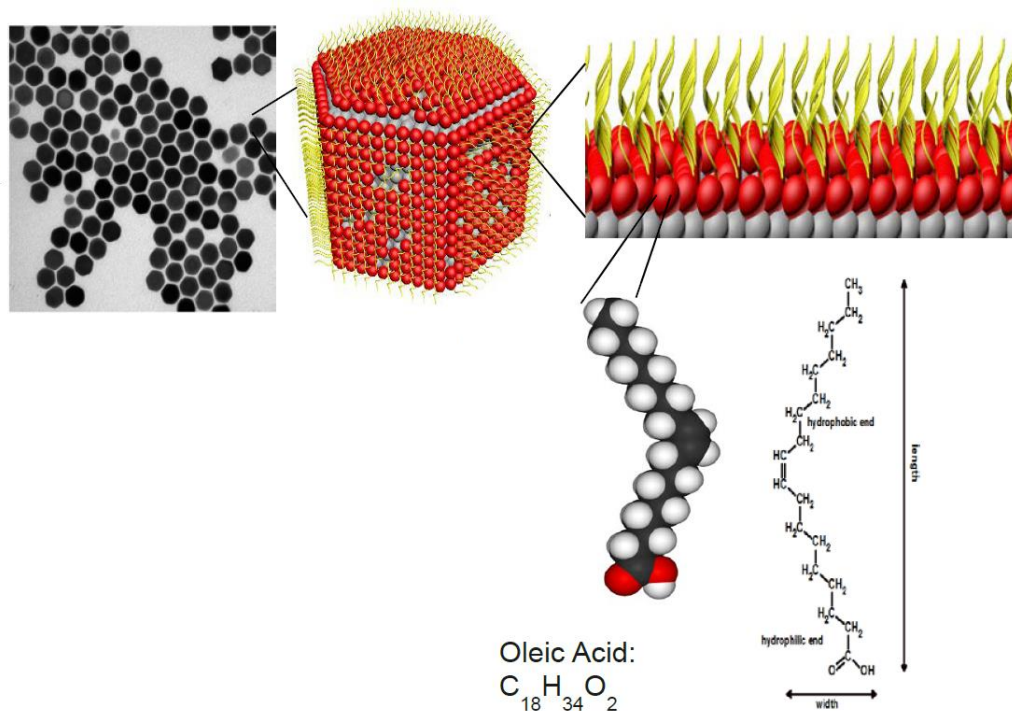
**Figure 2.2** Typical UCNP morphology with representation of surface for as synthesised UCNPs capped with oleic acid molecules. Reproduced from [63].

Recently sub 6 nm β-NaYF$_4$ UCNPs have been produced by controlling the ratio of starting precursors NH$_4$F and NaOH via their addition to the reaction using two automatic liquid samplers [64]. However, decreasing the particle size of UCNPs results in emission decrease due to the lower number of lanthanide dopants per particle available to participate in upconversion. This combined with the massive surface-area-to-volume ratio at this scale a source of non-radiative energy loss through surface defects results in a non-linear luminescence decrease as size decreases [59]. Additionally, it is understood that the sensitizer and activator lanthanide ions are uniformly distributed within the NaYF$_4$ crystal. This assumption has developed due to the similarity in properties among the rare earth ions, with minor differences in ionic radius and electronic polarity being overlooked to effect distributions across single UCNPs. The inability of initial studies to determine the sharpness of the interface between core/shell UCNPs reinforced this notion [65] leading to unsupported claims of homogeneous shell or homogeneous doping in NaREF$_4$ UCNPs [66, 67]. Follow up and counter studies using synchrotron energy dependent XPS, EDS and ICP-MS/AES methods revealed non-uniform distributions of Y$^{3+}$, Nd$^{3+}$ and Tb$^{3+}$ in NaGdF$_4$ UCNPs and heterogeneous distributions of Yb$^{3+}$ in NaGdF$_4$ UCNPs [66]. These results directly related to the differences in ionic radii

between $Gd^{3+}$ and other lanthanide dopants [68]. Similar analysis of $NaYF_4$ core/shell UCNPs by electron energy loss spectroscopy and EDS revealed anisotropic shell growth [69]. Even luminescence spectroscopy studies have clearly shown that a significant amount of $Eu^{3+}$ ions from a $NaEuF_4$ core particle become incorporated into $NaGdF_4$ during shell formation [70].

To overcome these issues researchers have also begun to investigate controlling the shape of UCNPs allowing for the growth of hybrid UCNPs for better spatial control of dopant distribution along with the possibility of multiple functions. A sophisticated map of routes for the synthesis of fluoride UCNP nano-architectures including hourglass, nanoflowers, nanocylinders and nano-dumbbells are shown in Figure 2.3. These structures fabricated from control over the ratio of oleate anions and oleate molecules on the crystallographic surface facets of the UCNPs.
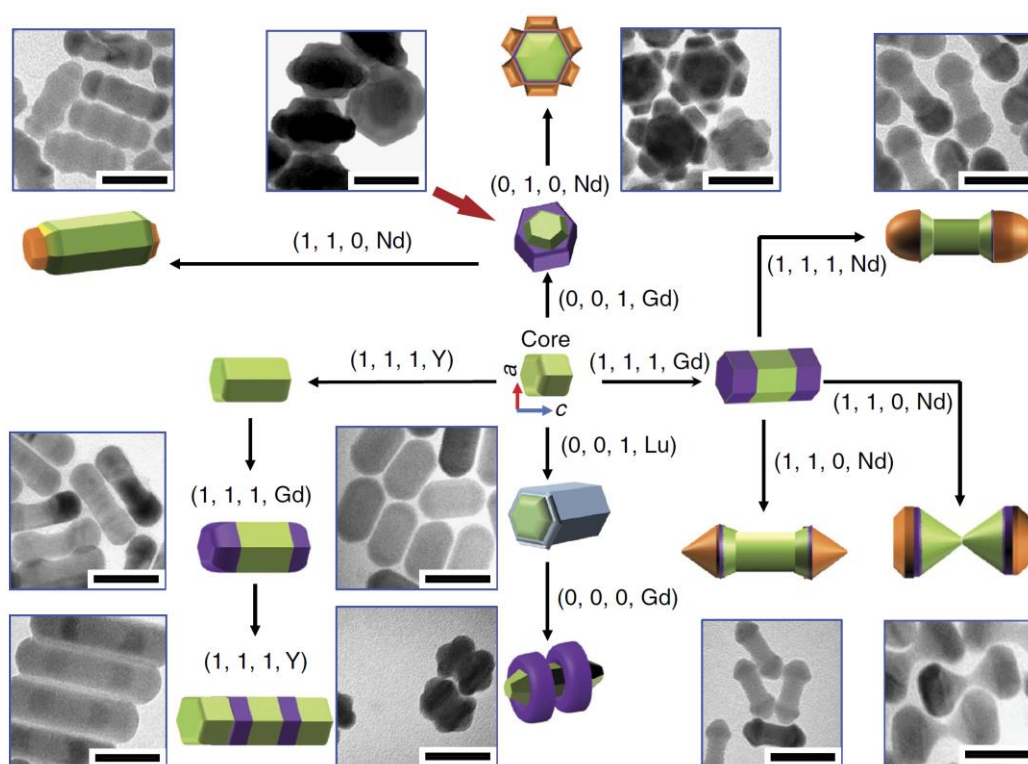


**Figure 2.3** Wide variety of UCNP morphologies available through control of growth mechanisms (scale bar, 50 nm). Reproduced from [71].

## 2.1.3    Upconversion Optical Process

Upconversion is an anti-Stokes' emission process which is contrary to Stokes' Law which states that photons absorbed by fluorescence light emitters are at a higher energy than emitted photons. Upconversion as a concept was first proposed by Bloembergen in 1959 [72] and was first experimentally realised independently by Auzel [73] and Ovsyakin & Feofilov [74] in 1966 demonstrating lanthanide sensitizer/activator systems of Ytterbium/Erbium and Ytterbium/Thulium could upconvert near infrared light into visible light via the excited sensitizer transferring energy to the activator which would then emit photons when relaxing. The intensity ($I$) of this $Ln^{3+}$ upconversion emission can be estimated by equation (1)

$$I = \phi \sigma_S \eta_{ET} \varphi_A \qquad (1)$$

Where $\phi$ is the photon flux of the excitation radiation, $\sigma_S$ is the absorption cross section of the sensitizer ion, $\eta_{ET}$ is the energy transfer efficiency from the sensitizer to the activator and $\varphi_A$ is the quantum yield of the activator.

The mechanisms involved in upconversion can be separated into five different categories as shown in Figure 2.4 [75, 76]. Excited state absorption (ESA) represented in Figure 2.4 (a) involves a single ion reaching an excited state above the ground state from the sequential absorption of incident excitation which is followed by relaxation via radiative emission. ESA is effective for trivalent lanthanides which have both long lifetimes at intermediate metastable energy levels and ladder like uniformly separated energy levels that promote sequential absorption. Due to this, ESA can be achieved for trivalent lanthanides using weak photon flux excitation however the efficiency is limited by their weak absorption cross section.

In the excited state the ion or sensitizer can now transfer energy to another ion or activator that has an approximately matching energy level, as shown in Figure 2.4 (b). This radiative or non-radiative process is known as energy transfer upconversion (ETU). A process which is dependent on both the energy transfer efficiency between the activator and the sensitizer and the quantum yield of the activator. Both can be influenced by factors such as the distance between the ions and the concentration of activator and sensitizer.

If the concentration of ions is sufficient then energy migration upconversion (EMU) can occur where excitation energy is essentially donated from one ion to the next as shown in Figure 2.4 (e). While this process can allow energy to reach activators distanced from the point of excitation it also increases the likelihood of energy being lost non-radiatively by migrating to quenchers such as lattice defects.

Additionally, as portrayed in Figure 2.4 (d) an activator in the ground state can also be excited by two separate sensitizers in a process known as cooperative energy transfer (CET). However, due to this excitation occurring through virtual states it is usually less efficiency than both ESA and ETU.

The final process depicted in Figure 2.4 (c) is photon avalanche (PA) which involves a cyclic cross relaxation between a pair of ions. Cross relaxation (CR) is the process of an excited ion undergoing non-radiative decay with the energy being absorbed by an adjacent ion. For PA to occur, initially one already excited ion is excited further by additional excitation then by CR another ion absorbs this energy. Finally, the energy is reabsorbed by the first ion which is able to relax via radiative emission.
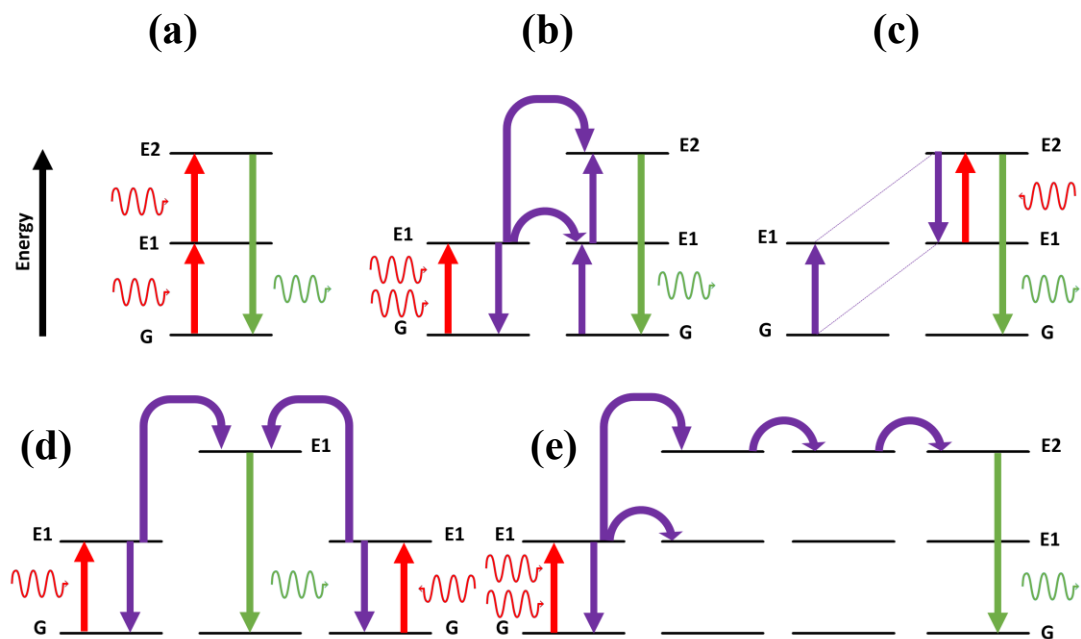


**Figure 2.4** Mechanisms of upconversion. Excited state absorption (ESA) (a), Energy Transfer Upconversion (ETU) (b), Photon Avalanche (PA) (c), Cooperative Energy Transfer (CET) (d) and Energy Migration Upconversion (EMU) (e). Red represents excitation, purple represents energy transfer and green represents emission.

In a typical system of a co-doped $Er^{3+}/Yb^{3+}$ $NaYF_4$ crystal under 980 nm laser excitation, as shown in Figure 2.5 (a) excitation absorption occurs via the $Yb^{3+}$ ion with its single energy level transition of $^2F_{7/2} \rightarrow \, ^2F_{5/2}$. This transition approximately matches the energy of the 980 nm photons and this along with the relativity large absorption cross section of $Yb^{3+}$ compared to other lanthanides explains why it is preferred as a sensitizer [77]. In the excited state the $Yb^{3+}$ ion disregarding other non-radiative losses such as lattice defects and surface quenchers can non-radiatively transfer energy to adjacent $Yb^{3+}$ ions via EMU allowing energy to migrate around the lattice or transfer energy to an $Er^{3+}$ ion via ETU for radiative visible upconversion emission to occur. For the optimal doping concentration of 2% $Er^{3+}$ and 20% $Yb^{3+}$ ETU results in the most prominent characteristic emission peaks of green at 550 nm and red at 660 nm shown in Figure 2.5 (b) resulting from the $^2H_{11/2}/^4S_{3/2} \rightarrow \, ^4I_{15/2}$ and $^4F_{9/2} \rightarrow \, ^4I_{15/2}$ $Er^{3+}$ transitions respectively. The visible distinctive green colour of this emission is pictured in the inset of Figure 2.5 (b).

$$\varphi = \frac{\text{No. photons emitted}}{\text{No. photons absorbed}} \qquad (2)$$

However, this process is restricted by the narrow and relatively low absorption cross-sections ($< 10$ $M^{-1}$ $cm^{-1}$) [78] of lanthanide ions which is the leading attribute to the low upconversion quantum yield and emission of lanthanide doped UCNPs. As equation (2) states the quantum yield of upconversion is the number of photons emitted divided by the number of photons absorbed. For ETU at its most basic two low energy photons are required to produce one higher energy photon which gives a theoretical upper limit for quantum yield of 50%. To date the record for reported UCNP upconversion quantum yield is 7.6% [79] though typical values are closer to ~0.1% [21]. As equation (1) states upconversion scales with excitation power, since a higher photon flux yields a higher probability of exciting an already excited electron. Using a high photon flux is a common method in studies to counteract the low quantum yield and weak upconversion emission. This has resulted in laser fluxes of ~$10^7$ $W/cm^2$ being used, which is seven orders of magnitude higher than the FDA-approved NIR irradiation levels of ~1 $W/cm^2$ [27, 28]. Thus, to make UCNPs effective for practical applications their emission intensity needs to be improved.

**(a)**
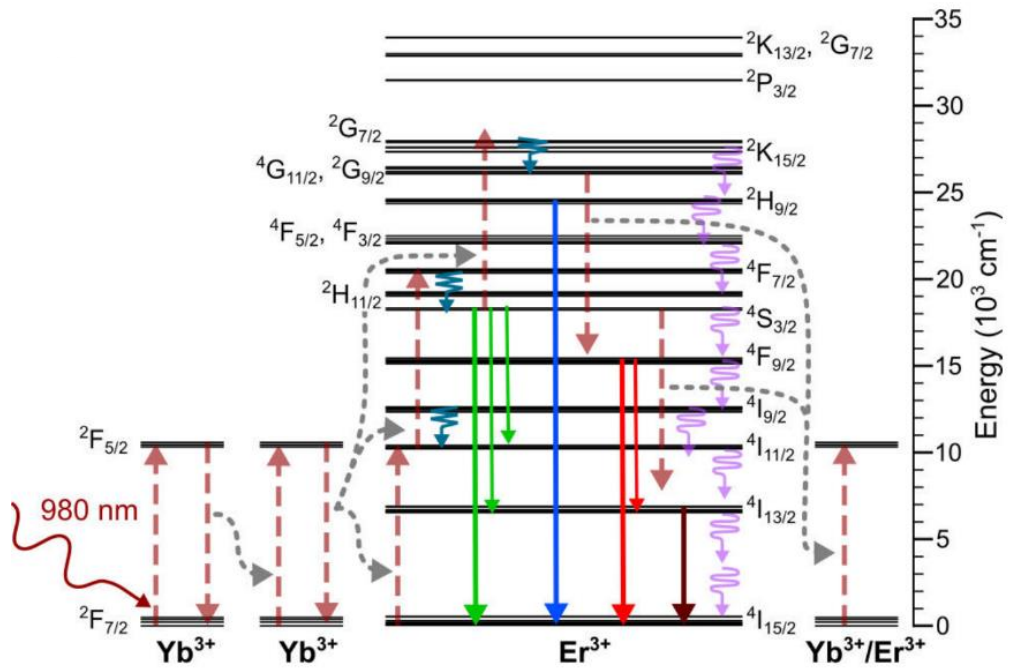


**(b)**
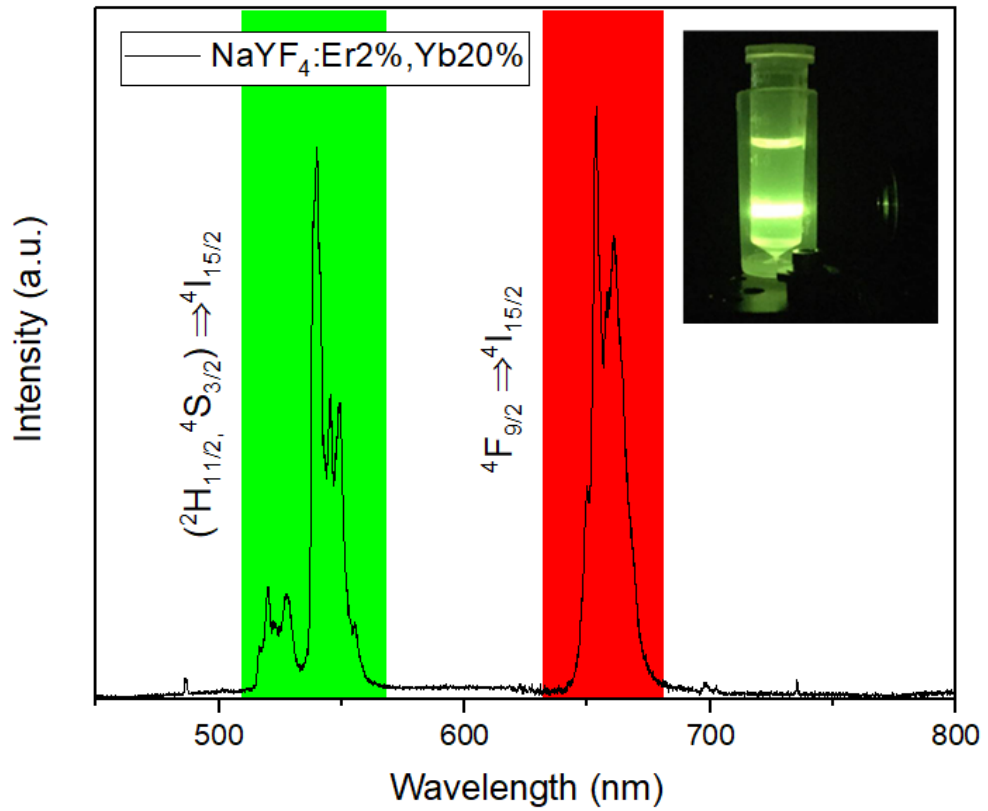
**Figure 2.5** Energy level representation of co-doped $Er^{3+}/Yb^{3+}$ NaYF$_4$ upconversion process under 980 nm laser excitation (a) Reproduced from [80]. Emission spectrum of 2% $Er^{3+}$/20% $Yb^{3+}$ NaYF$_4$ UCNPs under 980 nm excitation with inset photo of visible emission (b).

# 2.2 Approaches for Optical Enhancement

The emission performance of current state UCNPs is an area of research with the potential for enormous enhancement. This has led to many different methods of enhancement being applied that can fall into these six broad categories as shown in Figure 2.6 which are:

- Surface passivation: Coating the optically active UCNP core with a shell layer/s that can quench surface defects and impurities reducing unwanted energy loss at these sites.

- Broadband sensitization: Utilising ligands on the surface of the UCNP that are cooperative to the upconversion process increasing factors like absorption.

- Photonic crystal engineering: Producing artificial periodic structures that trap and guide light towards UCNPs for enhanced absorption.

- Surface plasmon coupling: A condition that occurs in nanoparticles of gold and silver which can be coupled with the internal transitions of lanthanide ions within UCNPs to enhance their emission and absorption.

- Energy transfer modulation: Optimizing the energy transfer between lanthanide ions by using optimal doping concentrations.

- Host lattice manipulation: Producing a more favourable environment for the lanthanide dopants within the host crystal by such methods as introducing

foreign elements into the crystal lattice to distort and lower symmetry around the lanthanide ions to enhance emission.

## Upconversion enhancement
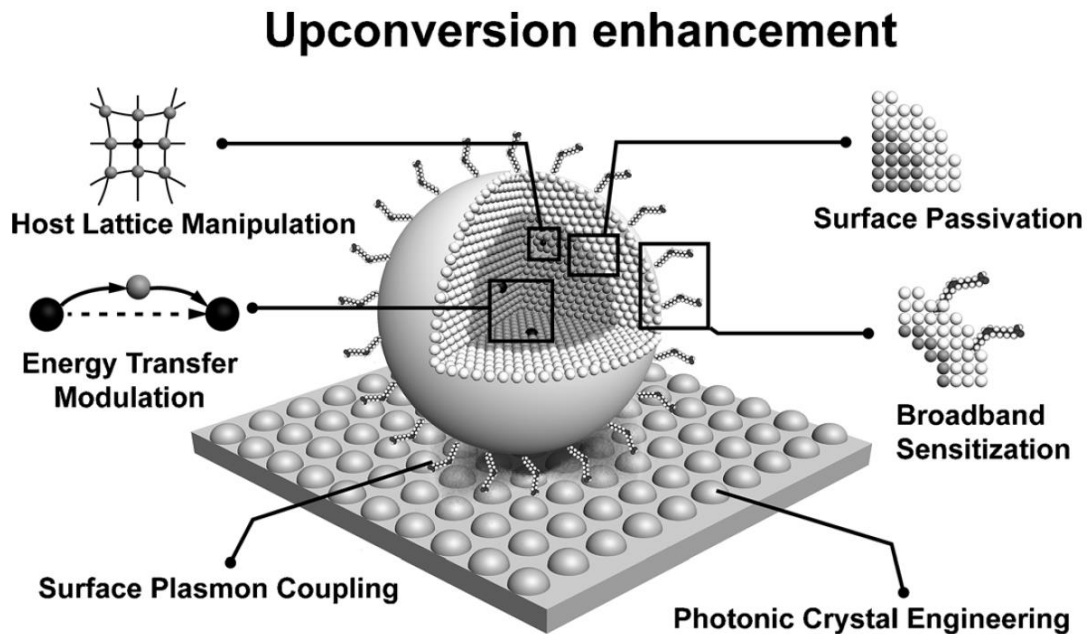


**Figure 2.6** Six categories of upconversion nanocrystal enhancement. Reproduced from [46].

The most effective reports of enhancement have been either synergic where two or more of these methods are combined and/or employed a unique design structure based upon careful consideration of theory and/or existing works. These strategies have delivered enhancement factors above what any method could achieve alone. For my research I decided to initially take the synergic strategy for enhancement and combine surface passivation and surface plasmon coupling enhancement methods. This was followed by an exploration into an emerging form of host lattice manipulation and an application of a new type of phononic broadband sensitization. These four enhancement categories are the focus of the following section.

## 2.2.1 Host Lattice Manipulation

A common manipulation of the $NaYF_4$ lattice involves annealing which can remove internal defects and induce phase change [50]. Several studies have reported both enhancement and quenching from the application of annealing which is highly

dependent on the phase and size of the pre-annealed UCNP, annealing temperature, annealing duration and annealing environment [81, 82]. A new phase of NaYF$_4$ termed the hex-to-cub phase has recently been discovered and synthesised with an even lower phonon energy than β-NaYF$_4$ [48]. This new hex-to-cub phase is described as a higher ordered cubic phase of NaYF$_4$ produced from exposing β-NaYF$_4$: Yb$^{3+}$/(Er$^{3+}$/Tm$^{3+}$) UCNPs to a 980 nm laser at a power density of 600 W/cm$^2$ for 40 minutes [48]. The laser treatment causes heating inside the crystal lattice localised at Yb$^{3+}$ ions due to their specific absorption of the 980 nm laser. Phononic coupling depletes this energy to heat, allowing direct atomic rearrangement towards the hex-to-cub phase. As a result of the lower phonon energy the hex-to-cub phase has overall upconversion emission enhanced by a factor of >700, as shown in Figure 2.7 (a,b).

Even though this new phase of NaYF$_4$ has a substantially enhanced emission compared to both the β and α phases the required laser annealing like other intense annealing procedures has detrimentally effects on the size and morphology of the UCNPs. After 40 minutes of laser annealing the UCNPs enlarged into irregular particles losing both their uniform particle size and morphology.
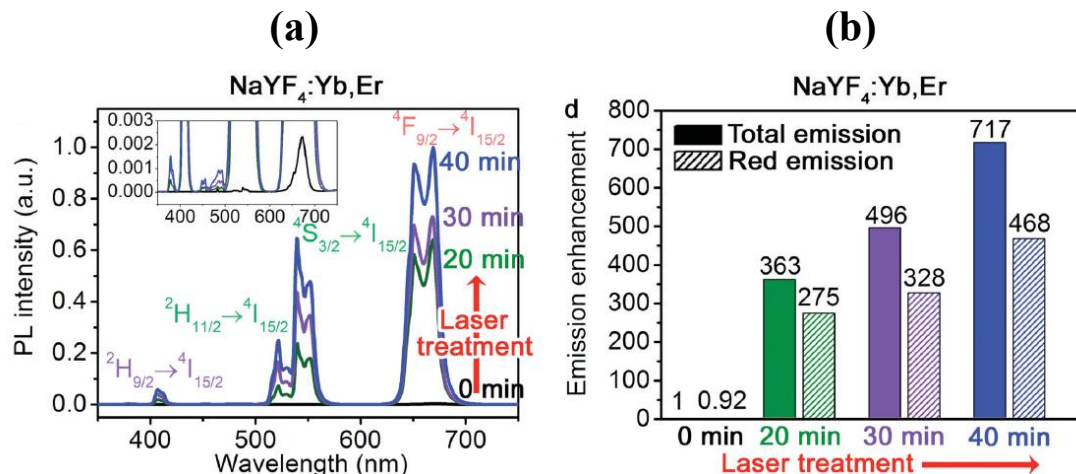


**Figure 2.7** Photoluminescence spectra (a) and emission enhancement (b) of upconversion from NaYF$_4$: Yb$^{3+}$, Er$^{3+}$ UCNPs after 40 minutes of laser annealing. Reproduced from [48].

As mentioned, the introduction of foreign elements into the NaYF$_4$ lattice is another strategy to enhance upconversion emission by manipulating the crystal which influences the coordination environment and crystal field splitting of the lanthanide

ions. Li$^+$ has been extensively incorporated into UCNPs with reported enhancement factors of eight times in Tm$^{3+}$ doped NaYF$_4$ UCNPs and up to 30 times in Er$^{3+}$ doped NaYF$_4$ UCNPs [83, 84]. By the method of ion exchange additional Na$^+$ has also been exchanged into NaYF$_4$: Yb$^{3+}$, Er$^{3+}$ UCNPs resulting in a massive ~4,200 times enhancement displayed in Figure 2.8 (a,b) [85]. This type of foreign ion enhancement in UCNPs is mainly attributed to a changing of the local crystal structure around the lanthanide dopants. It can also be attributed to a decrease of internal defects yet further exploration of this enhancement method is required to determine its exact mechanism.

**(a)**　　　　　　　　　　**(b)**
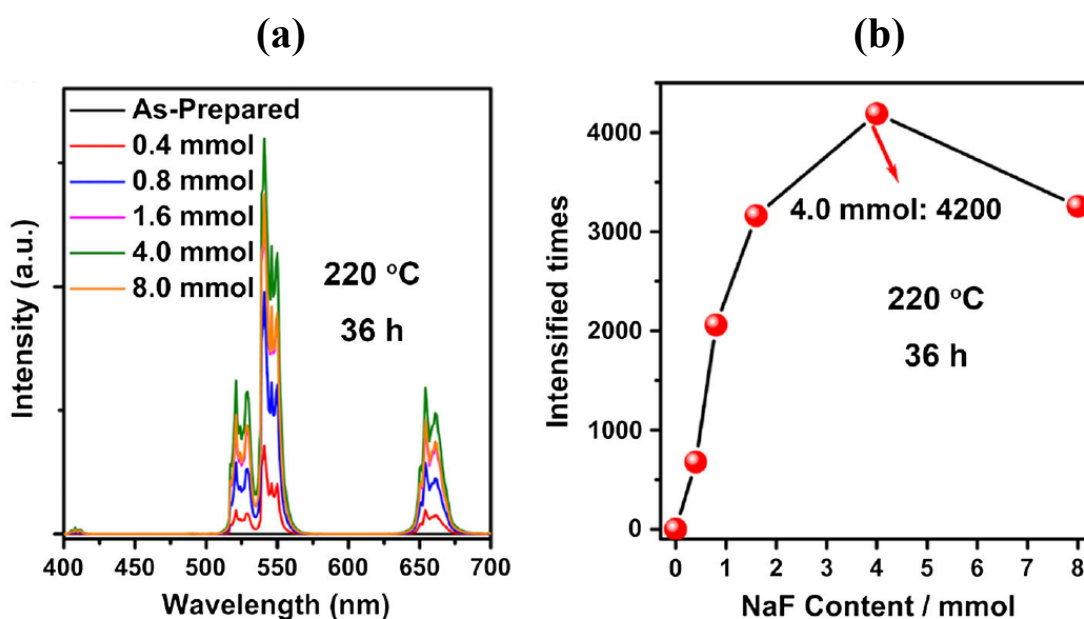


**Figure 2.8** Optimised emission enhancement spectra (a) and enhancement factor (b) from Na$^+$ doping of NaYF$_4$: Yb$^{3+}$, Er$^{3+}$ UCNPs. Reproduced from [85].

Restricting the dimensions of the host material is a new form of host manipulation that has recently attracted attention for upconversion with the development of 2D materials. The exciting enhanced quantum confined properties of 2D materials make them ideal for application in optoelectronics, photodetection, gas sensing, photocatalysis and photovoltaics [7, 86]. The large surface area of 2D nanosheets is advantageous for energy transfer. It can be functionalised with organic dye molecules to enhance absorption of NIR light or metal nanoparticles for surface plasmon coupling [87-89]. Two widely studied 2D materials h-BN and diamond have recently been found to display upconversion functionality through their respective defects [90, 91]. For lanthanide upconversion various 2D hosts doped with lanthanide ions

including $MoS_2$ [92], BiOBr [93] and $LaNb_2O_7$ [94] and even the fluoride $SrYbF_5$ [95] have been reported with upconversion emission. However, as stated previously, the preferred host material for lanthanide upconversion is $NaYF_4$. Producing 2D fluoride nanosheets of $LnF_3$ is more energetically favourable and controllable than $XLnF_4$ nanosheets due to their lower formation and stabilization energy [96]. Regardless 2D $NaYF_4$ nanosheets have been partially reported but only formed as an intermediate towards the formation of nanorod UCNPs [97]. The bottom up synthesis used to produce these intermediate nanosheets lacks control of the final material and a top down exfoliation synthesis of 2D $NaYF_4$ would be preferred to provide greater control over the size and doping concentration of the nanosheets. Producing a top down synthesis method for 2D $NaYF_4$ remains a challenge considering $NaYF_4$ is not a van der Waals crystal which is the ideal crystal for exfoliating due to the weak interlayer bonding [98]. However, if feasible 2D $NaYF_4$ could potential lead to enhanced upconversion emission properties due to quantum confinement effects.

## 2.2.2      Surface Plasmon Coupling

A surface plasmon is a collective oscillation of free electrons on the surface of a material that matches the frequency of incoming photons. Plasmonic nanostructures have been extensively investigated for enhancing the emission and absorption properties of luminescent nanomaterials [99]. Plasmonic nanoparticles specifically noble metal nanoparticles such as gold (Au) and silver (Ag) that have a tuneable localised surface plasmon resonance (LSPR) a bound non-propagating oscillation of free electrons at the surface [100], are ideal for coupling with UCNPs to enhance their upconversion emission. As shown in Figure 2.9 both Au and Ag have been used for plasmonic coupling in such forms as spherical nanoparticles [101], nanowires [102], nanoislands [103] and lithographically patterned nanoarrays [104] which have reached enhancement factors of almost three orders of magnitude.
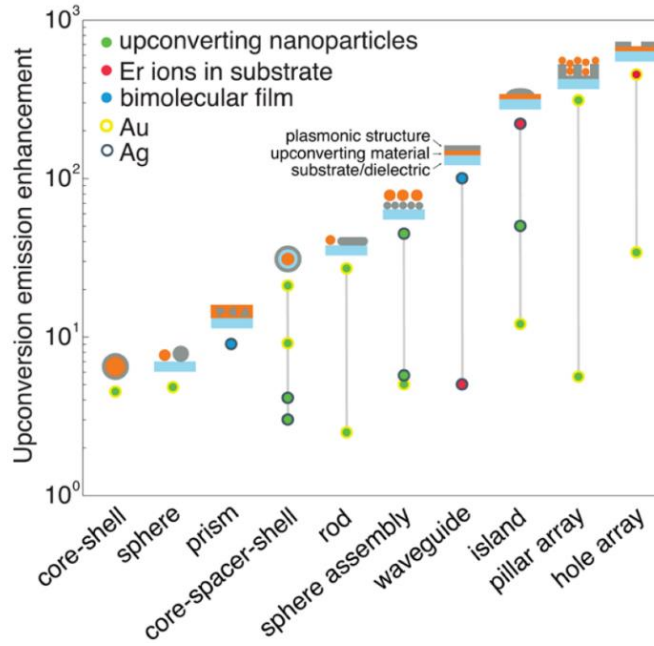
**Figure 2.9** Upconversion emission enhancement for a wide variety of plasmonic design structures. Reproduced from [88].

Plasmonic enhancement via the LSPR of noble metal nanoparticles can enhance the absorption and emission of both the sensitizer and activator. Under weak excitation before saturation in an environment that does not affect the polarizability of the ion the plasmonic excitation enhancement ($f_{ex}$) can be expressed by the following equation (3) [105].

$$f_{ex} = \frac{|\mu.E|^4}{|\mu.E_0|^4}\frac{\gamma_0}{\gamma} \qquad (3)$$

Where μ is the transition electric dipole moment, $E$ and $E_0$ are the localised E-field of the LSPR and incident E-field respectively and γ and $\gamma_0$ are the total decay rates in the presence and absence of the metallic nanoparticle respectively.

If the LSPR wavelength overlaps with the wavelength of the excitation for either the sensitizer and/or activator, then $E$ will become greatly enhanced causing an increase to the absorption of the sensitizers and/or activators within that region [88].

Under the same conditions and with an overlap with emission wavelength the LSPR due to the Purcell Effect can spontaneously enhance emission rate which can be expressed by the following plasmonic emission enhancement ($f_{em}$) equation (4) [106].

$$f_{em} = \frac{\eta}{\eta_0} \quad (4)$$

$$\eta_0 = \frac{\gamma_{rad}}{\gamma_{rad} + \gamma_{nonrad}} \qquad \eta = \frac{\gamma_{rad} + \gamma_{m\,rad}}{\gamma_{rad} + \gamma_{nonrad} + \gamma_{m\,rad} + \gamma_{m\,nonrad}}$$

Where $\eta$ and $\eta_0$ are the plasmonic modified emission efficiency and original quantum emission efficiency of the ion respectively which can be expressed in terms of decay rates where $\gamma_{rad}$ and $\gamma_{nonrad}$ are the radiative and non-radiative decay rates of the ion and $\gamma_{m\,rad}$ and $\gamma_{m\,nonrad}$ are the plasmonic modified radiative and non-radiative decay rates respectively.

Thus the total enhancement ($f_{tot}$) from both the excitation and emission enhancement can be expressed as a product of both equation (3) and equation (4) by equation (5) [107].

$$f_{tot} = f_{em}f_{ex} = \frac{|\mu.E|^4}{|\mu.E_0|^4} \frac{\gamma_0}{\gamma} \frac{\eta}{\eta_0} \quad (5)$$

This plasmonic enhancement is dependent on the intensity and position of the LSPR which can be designed by the plasmonic structure through control of the size, shape and composition of the noble metal nanoparticle. For example Au nanorods can produce a dual LSPR with one peak centred on the excitation of the sensitizer and one peak centred on the emission of the activator [108].

However, the metal nanoparticle can also act as a quencher with energy transfer between the UCNP and metal nanoparticle being lost non-radiatively [109, 110].

Non-radiative energy transfer can be explained by Förster Resonance Energy Transfer (FRET) [111] and Dexter Electron Transfer [112] mechanisms which can be expressed by equations (6) and (7) respectively.

$$k_{et} = \tau^{-1}\left(\frac{R_0}{r}\right)^6 \quad (6)$$

$$k_{et} \propto Je^{\frac{-2r}{L}} \quad (7)$$

Where $k_{et}$ is the energy transfer rate, $\tau$ is the donor lifetime, r is the distance between the donor and acceptor, J is the integrated spectral overlap between the donor and acceptor, L is the ratio of the separation between the donor and acceptor normalised to

their van der Waals radii and $R_0$ is the FRET distance between the donor and acceptor such that when $R_0 = r$, $k_{et} = k_r$ where $k_r$ is the radiative decay rate.

Dexter electron transfer is only efficient when the excited donor is < 1 nm from the acceptor allowing an overlap in electron wave functions between the two. However, because of the nature of the dipole-dipole coupling in FRET it can efficiently occur within distances of < ~10 nm.
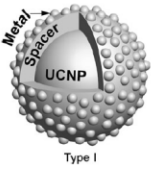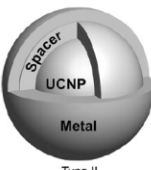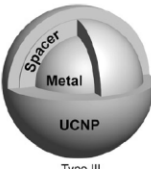
Therefore, it is critical to also control the distance between the plasmonic metal nanoparticle and UCNP to maximise enhancement and minimise quenching due to FRET. Simulations taking these factors into account shown in Figure 2.10 place this optimum distance at 10 nm – 35 nm.
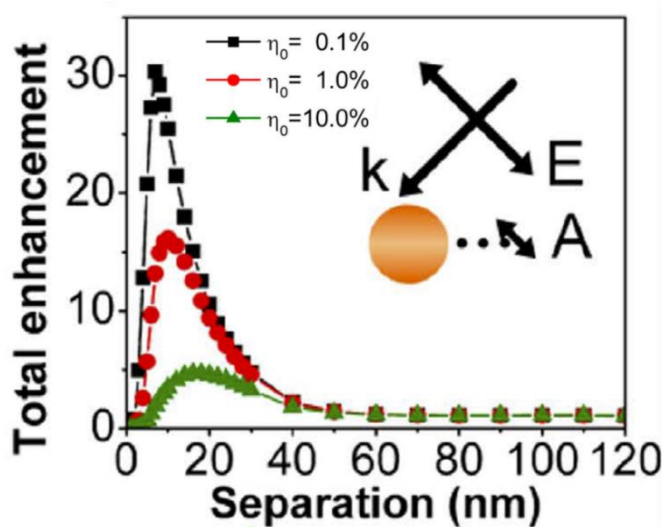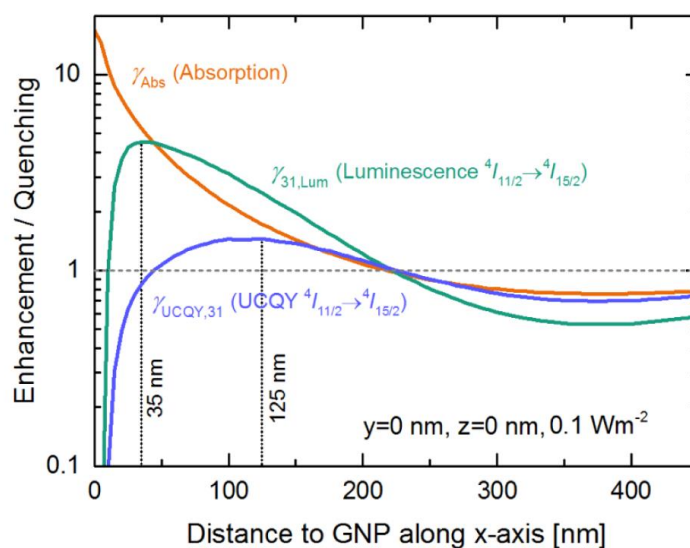
**Figure 2.10** Relationship between the plasmonic enhancement and distance between gold nanoparticle and UCNP. Reproduced from [110, 113].

Controlling the separation between the plasmonic nanostructure and UCNP is challenging particularly in the range required for optimum enhancement. This is particularly true for the core-spacer-shell design which has been extensively studied as Figure 2.11 highlights. In the reported types of this design the spacer is vital for minimising non-radiative FRET energy transfer which causes luminescent quenching due to the direct contact of the UCNP with the Au or Ag surface [101]. The core-spacer-shell design structures have been previously fabricated as shown in Figure 2.11 in either metal core-spacer-UC shell nanoparticles [114-116] or UC core-spacer-metal shell nanoparticles [117, 118]. However, a spacer of either metal, polymer or $SiO_2$ was applied in all these previous implementations for attaching the outer shell component. These materials are not ideal for use as the spacer as they inhibit the plasmonic enhancement of luminescence due to apparent parasitic absorption at thicknesses required for optimum plasmonic enhancement [119, 120].

| Structure Design | Core (size) | Building Block Spacer[a] (size) | Shell (size) | Enhancement Factor (Emission wavelength) |
|---|---|---|---|---|
| **Type I** | $NaYF_4$:Yb/Tm | PAA/PAH | Au (2 nm) | ≈2.5 (452 nm, 476 nm) |
| | $NaYF_4$:Yb/Er/Gd | – | Au sphere | 3.8 (540 nm); 4.0 (660 nm) |
| | $NaYF_4$:Yb/Er | $SiO_2$ (10 nm) | Ag (15 nm) | 14.4 (542 nm); 12.2 (656 nm) |
| | | | Ag (30 nm) | 9.5 (542 nm); 10.8 (656 nm) |
| | $NaYF_4$:Yb/Tm | – | Au (≈10 nm) | 73.7 (291 nm); 109.0 (345 nm); 44.9 (362 nm); 49.8 (450 nm); 29.9 (474 nm) |
| | $NaYF_4$:Yb/Tm | PAMAM (2.5 nm) | Au rod | 27 (805 nm); 6 (470, 550 nm) |
| | $NaYF_4$:Yb/Er | $SiO_2$ (11 nm) | Ag sphere | 4.4 (525 nm, 545 nm); 3.5 (660 nm) |
| **Type II** | $NaYF_4$:Yb/Er | $SiO_2$ (11 nm) | Au shell | 9.1 (525 nm, 545 nm); 6.75 (660 nm) |
| | $NaYF_4$:Yb/Er/Gd | – | Au shell | 3.2 (540 nm); 9.6 (660 nm) |
| | $NaYF_4$:Yb/Er/Tm | – | Au shell (4–8 nm) | 8 (646 nm) |
| | $NaYF_4$:Yb/Er | $SiO_2$ (18 nm) | Au shell (2.8 nm) | ≈4 (410 nm); ≈2.6 (545 nm); ≈2.3 (660 nm) |
| | $NaYF_4$:Yb/Er/Tm | PAMAM | Au shell (20 nm) | 20 (518 nm); 21 (540 nm) |
| | | | Ag shell (20 nm) | 20 (413 nm); 22 (452 nm) |
| **Type III** | Ag (130 nm) | $SiO_2$ (20 nm) | $Y_2O_3$:Er | 3.86 (550 nm); 3.39 (650 nm) |
| | Ag (50 nm) | $SiO_2$ (40 nm) | | 4.37 (550 nm); 3.06 (650 nm) |
| | Ag (50 nm) | $SiO_2$ (30 nm) | | 4.76 (550 nm); 3.26 (650 nm) |
| | Ag (20 nm) | $SiO_2$ (35 nm) | | 1.77 (550 nm); 2.08 (650 nm) |
| | Au (30 nm) | $SiO_2$ (25 nm) | $Y_2O_3$:Yb/Er (12 nm) | 1.51 (549 nm) |
| | | $SiO_2$ (30 nm) | | 2.14 (549 nm) |
| | | $SiO_2$ (40 nm) | | 9.59 (549 nm) |
| | | $SiO_2$ (45 nm) | | 3.51 (549 nm) |
| | Au nanorod | $SiO_2$ | $LaF_3$:Yb/Er | 6.5 (550 nm) |

[a] PAA: Poly(acrylic acid); PAH: Poly(allylamine hydrochloride); PAMAM: Polyamidoamine dendrimer.

**Figure 2.11** Plasmonic core shell designs sorted by structure design, core size, spacer size, shell size and emission enhancement. Reproduced from [46].

This issue has been addressed recently via a number of creative methods including that of the nanocap method [121]. In this method UCNPs are sputtered with gold at two complimentary angles to produce a 'nanocap' atop the UCNP as Figure 2.12 (a) displays. By adjusting the angle of the sputtering, the plasmon resonance of the gold nanocap can be shifted. Using this method, it was found that a greater emission enhancement was achieved with a larger sputtering angle as the plasmon resonance shifted closer to the excitation wavelength this dependence highlighted in Figure 2.12 (b). When optimised this method could deliver a 64 and 101 times enhancement to green and red emission respectively.

**(a)** **(b)**
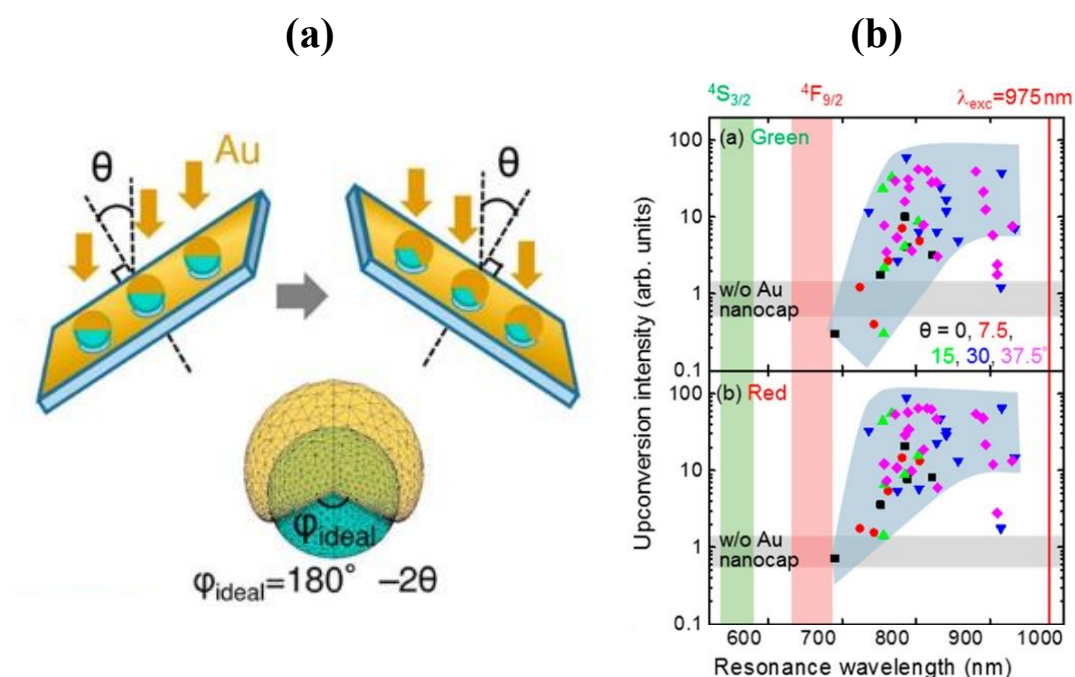


**Figure 2.12** Fabrication of gold nanocapped UCNP (a) and sputtering angle $\theta$ dependent enhancement to red and green emission (b). Reproduced from [121].

## 2.2.3    Surface Passivation

The surface of UCNPs contain multiple defects that can act as pathways for non-radiative relaxation. To passivate these defects, it is common practice to coat UCNPs with a shell layer. Inert shells around the UCNP comprising of the host crystal or other shell material with inaccessible electronic states are a popular choice. $NaYF_4$ or $NaGdF_4$ or $NaLuF_4$ are typically grown around the optically active UCNP core to avoid surface quenching. The choice effecting the morphology of the UCNP

depending on if the shell material is compressively or tensile strained to the core [122]. The influence of emission enhancement these shells have has been found to become insignificant above a thickness of 5 nm as Figure 2.13 (c) shows. A 5 nm shell thickness results in a two orders of magnitude increase in upconversion quantum yield according to Figure 2.13 (b) [80]. As Figure 2.13 (a) highlights this enhancement is dependent on the irradiance of the excitation used with thicker shells displaying higher enhancement factors for upconversion quantum yield at lower excitation power densities due to saturation effects.
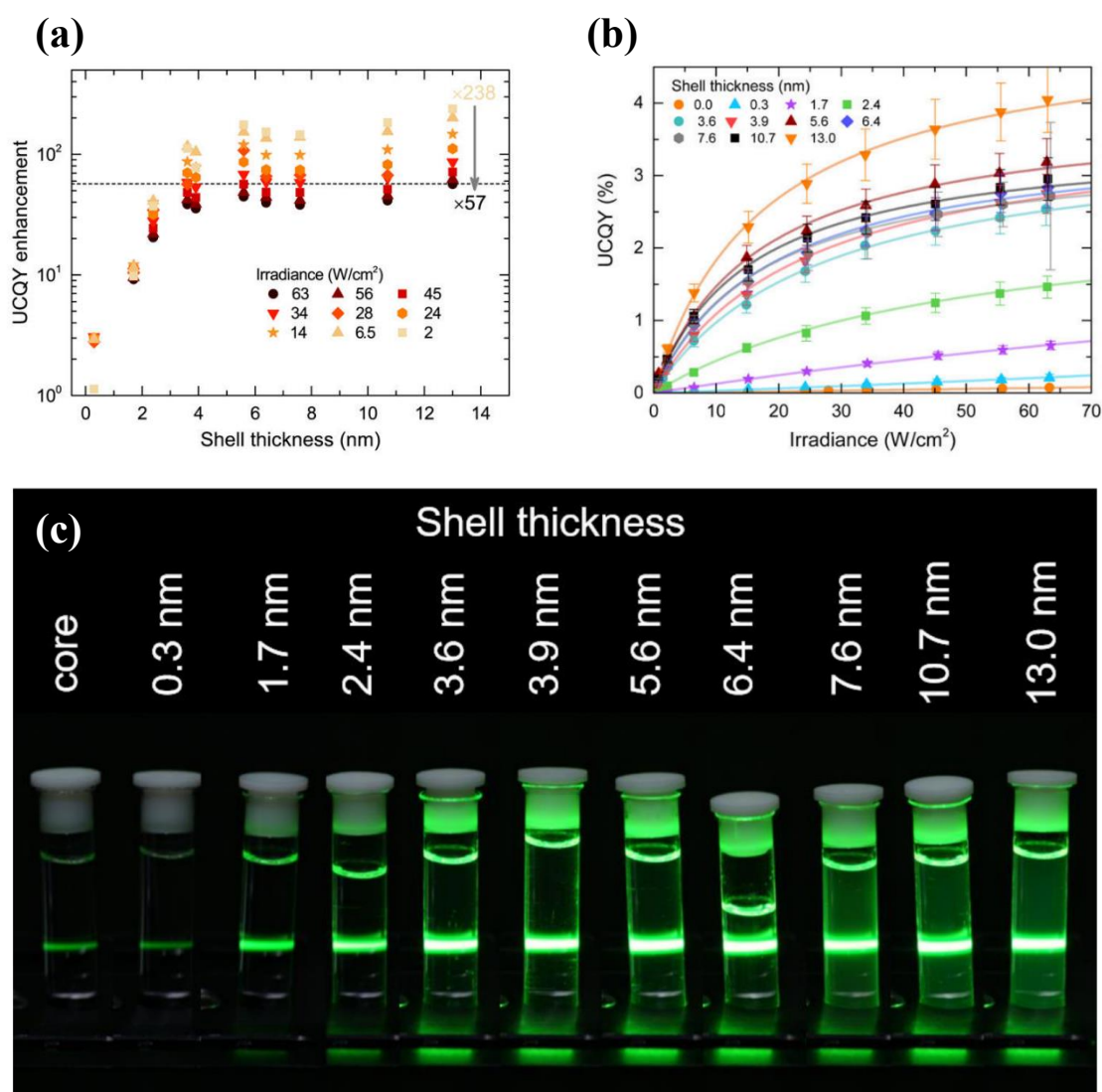


**Figure 2.13** Influence of inert β-NaLuF$_4$ shell thickness on quantum yield enhancement (a), quantum yield (%) (b) and optical intensity under 980 nm laser excitation at 63 W/cm$^2$ (c) for series of NaYF$_4$ UCNPs with increasing shell thickness. Reproduced from [80].

To overcome this bottleneck an active shell can be employed [123]. As demonstrated in Figure 2.14 (a) by only coating the optically active core with an inert shell this shell volume is not involved directly with the upconversion process. However, if the shell coating is replaced by $NaYbF_4$ the volume of the shell can now absorb additional incoming NIR excitation and transfer this to the core for enhanced emission which is demonstrated in Figure 2.14 (b). Additionally, by again coating this ($NaYF_4$: $Yb^{3+}/Tm^{3+}$)/$NaYbF_4$ UCNP with an inert shell of $NaYF_4$ to passivate the inner shell layer even higher emission enhancement is reported in Figure 2.14 (c).

Surface passivation especially for active shell designs where multiple shell layers are required results in relativity large UCNPs greater than 50 nm and thus their practicality is reduced.
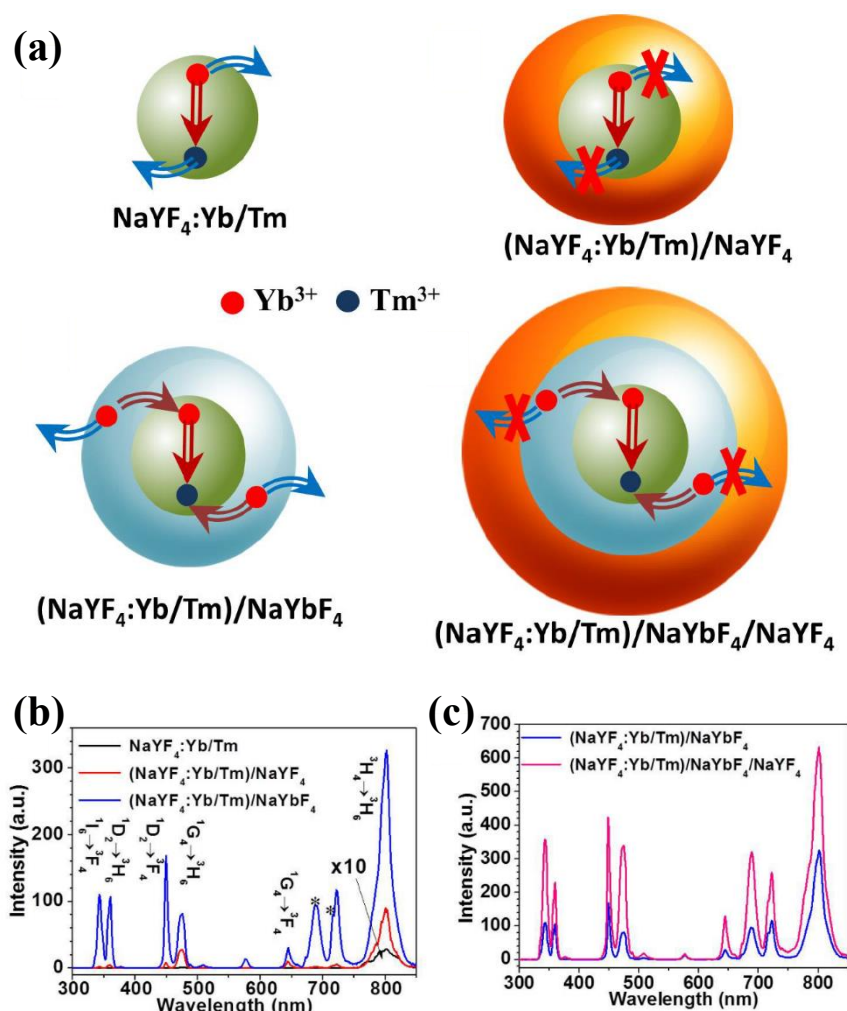


**Figure 2.14** Design logic (a) and relative emission intensity (b) for active shell designed $NaYF_4$: $Yb^{3+}/Tm^{3+}$ UCNPs (c). Reproduced from [123].

## 2.2.4      Broadband Sensitization

The surface of UCNPs can be functionalised with a wide variety of ligands as shown in Figure 2.15 for various biomedical applications including drug delivery and bioassays [124]. This functionalising approach can also be used to increase upconversion efficiency by utilising organic dyes and photosensitisers which act as antennae to absorb energy and funnel incoming light to the UCNP [125].
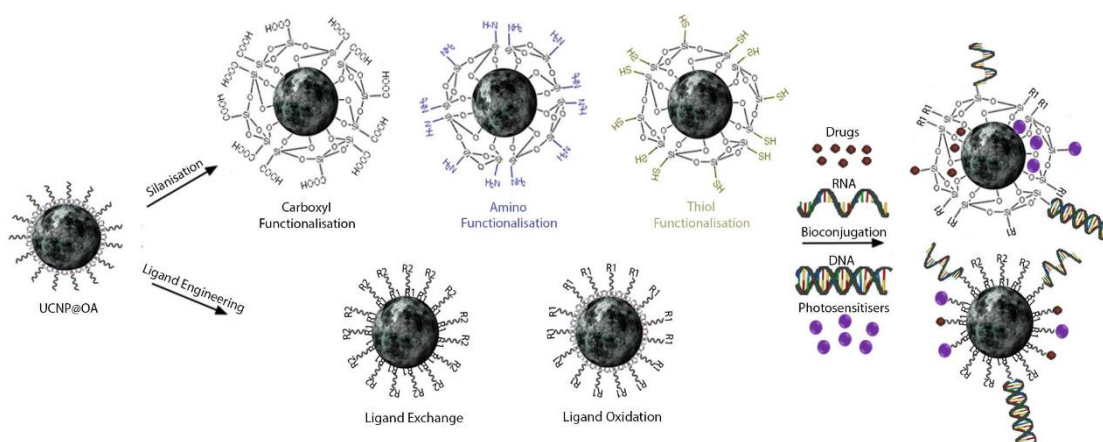


**Figure 2.15** Library of UCNP surface functionalisations. Reproduced from [124].

The most common type of broadband sensitization takes advantage of the up to five orders of magnitude higher extinction coefficient of dyes compared to lanthanides. The first demonstration of this type of broadband sensitization reported the attachment of the organic dye IR-806 to the surface of $NaYF_4$: $Yb^{3+}$, $Er^{3+}$ UCNPs resulting in a massive 3,300 times enhancement [87]. Further development of this concept with designs taking advantage of an active shell that should have allowed more efficient energy transfer to occur from the dye to the inner core only saw a 14 times increase in upconversion emission versus the non-functionalised UCNPs [126]. This difficultly to reach the enhancement achieved initially and the additional obstacles of dye enhancement saturation displayed in Figure 2.16 (a,b) and enhancement stability in air shown in Figure 2.16 (c) are still key challenges for broadband sensitization enhancement [127].
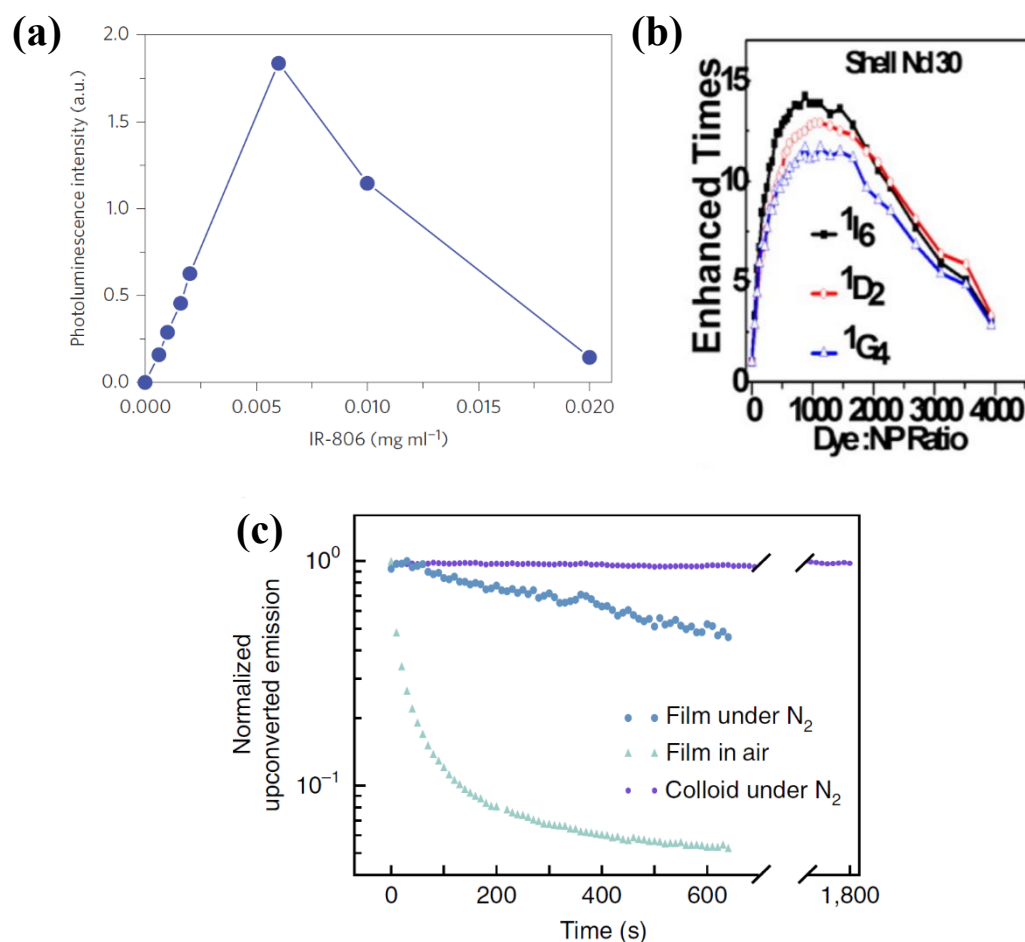
**Figure 2.16** The upconversion dye enhancement saturation (a,b) and dye enhancement stability of upconversion (c). Reproduced from [87, 126, 127].

Apart from dyes it is the OA ligand itself that has the potential for enhancing emission at high temperature. Upconversion efficiency at higher temperatures is usually decreased by thermal quenching caused by the increased activity of phonons that give leverage to competing non-radiative relaxation pathways [128, 129]. It is also commonly understood that quenching occurs from surface ligands [28, 130] including OA ligands [131]. However, taking into account reports of size-temperature dependent enhancement of UCNPs [132] explained by high temperature electron-phonon interactions [133] the established understanding could be contradicted and enhancement at high temperature achieved via the surface OA.

# Chapter 3

# Experimental Methods

In this chapter an overview of the synthesis and characterisation methods used throughout this thesis are presented. Materials in this project were synthesised and thoroughly characterised to determine their morphological, optical and chemical properties.

## 3.1    Synthesis

### 3.1.1    Core UCNP

Typical synthesis methods listed below were used to synthesize all UCNPs [129]. 1 mL of $LnCl_3$ in methanol (1.0 mmol, Ln = $Y^{3+}$, $Yb^{3+}$, $Er^{3+}/Tm^{3+}$) was mixed with OA (6 mL) and ODE (15 mL) in a 100 mL three-neck round bottom flask. The solution was then degassed under 99.999% pure Ar flow during heating to 150 °C followed by a 30 minute isothermal reaction to form a clear solution which was cooled to room temperature. 10 mL of methanol containing $NH_4F$ (4 mmol) and NaOH (2.5 mmol) was then added to the flask and stirred for 60 minutes. The solution was slowly heated to 110 °C and maintained at 110 °C for 30 minutes to completely remove the methanol and any residual water. The reaction solution was then quickly heated to 310 °C and maintained isothermally for 1 hour, before being cooled to room temperature. Ethanol was added to precipitate the formed nanocrystals, which were washed four times with cyclohexane, ethanol and methanol. The obtained pure $NaYF_4$: $Yb^{3+}$, $Er^{3+}/Tm^{3+}$ nanocrystals were finally redispersed in 10 mL of cyclohexane. All UCNPs were stored in -4 °C freezers.

## 3.1.2 Core Shell UCNP

First α-NaYF$_4$ seeds were obtained using all the preparation and pretreatment steps required for the NaYF$_4$ core synthesis method. The only two differences were that the lanthanide precursor was changed to 1 mmol of YCl$_3$ and the reaction temperature became 290 °C (instead of 310 °C). After the reaction, the nanoparticles were washed and redispersed in cyclohexane. The obtained pure α-NaYF$_4$ seeds in cyclohexane solution were mixed with 10 mL of ODE in one 100 mL three-neck flask. The mixture was then maintained at 110 °C for 30 minutes under 99.999% pure Ar flow. After the mixture was cooled to room temperature the α-NaYF$_4$ ODE solution as the precursor for the inert shell was obtained.

A hot-injection method was used for growing an undoped shell onto the core nanocrystals. 1 mL (0.2 mmol Ln$^{3+}$) of the obtained NaYF$_4$ core cyclohexane stock solution was mixed with OA (5 mL), OM (1 mL) and ODE (8 mL) in a 100 mL three-neck flask. The mixture was then degassed under 99.999% pure Ar flow and maintained at 110 °C for 30 minutes to completely remove cyclohexane as well as any residual water. After degassing, the solution was quickly heated to 305 °C and the pure α-NaYF$_4$ seeds in ODE solution were injected using a syringe (injection rate: 0.05 mmol α-NaYF$_4$ seed solution every 10 minutes); with the total amount injected producing different shell thicknesses as required. After the reaction, the precipitate was washed and stored in cyclohexane.

## 3.1.3 Noble Metal Dewetting

A Leica EM ACE600 sputtering and carbon thread coater as shown in Figure 3.1 (a) or Edwards E306 deposition system was used to sputter coat a 1 nm thick Au film or Ag film respectively onto glass coverslips. Annealing of the glass coverslip was then performed in a Lindberg Blue Mini-mite tube furnace as shown in Figure 3.1 (b). The tube was under vacuum with one end connected to a rotary pump and the other connected to a multi gas inlet. The coated glass coverslips were placed in a ceramic furnace boat at the centre of the tube. Annealing was performed with a N$_2$ gas flow rate of 100 SCCM for 1 hour at 400 °C to dewet the Au film into discrete Au nanoparticles as illustrated in Figure 3.1 (c).
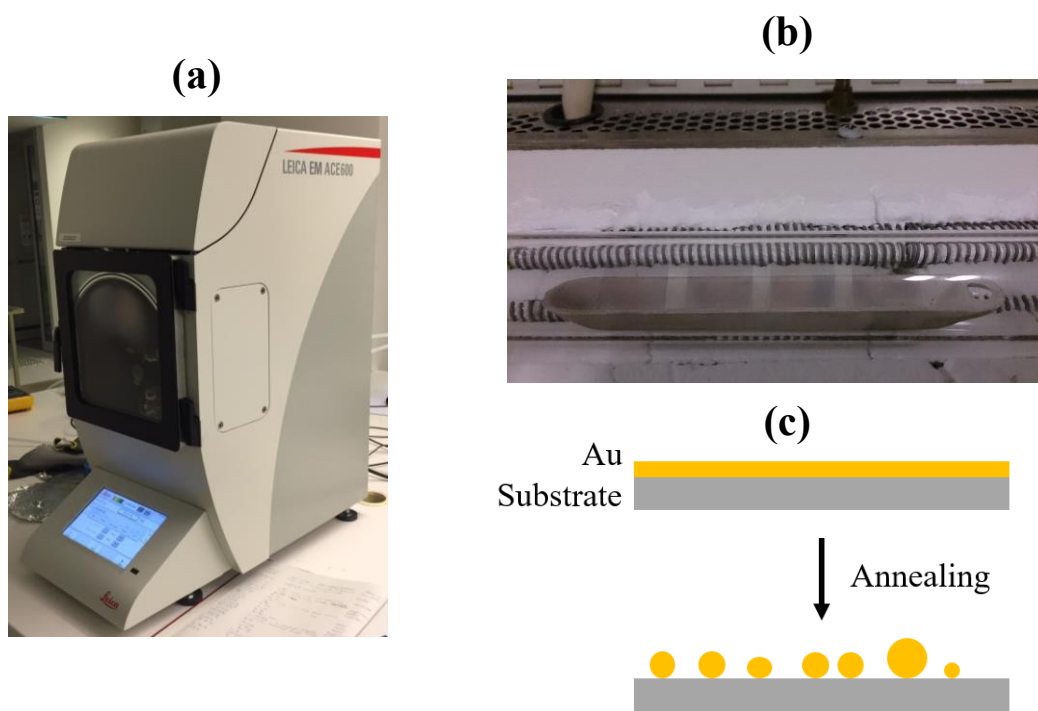
**Figure 3.1** Leica EM ACE600 sputtering and carbon thread coater (a). Reproduced from [134]. Image of coated glass slides on ceramic annealing boat inside tube of Lindberg Blue Mini-mite tube furnace (b) and illustration of dewetting process (c).

### 3.1.4 Soft Liquid Phase Exfoliation

0.1 g of bulk 1 μm - 5 μm sized $NaYF_4$ ($NaY_{0.77}Yb_{0.20}Er_{0.03}F_4$) powder material purchased from Sigma Aldrich was dissolved in a 1% (v/v) ethanolic solution of triethylamine (TEA). The solution was then sonicated in an ultrasonic bath (Unisonics FXP4M operated at 40 W) for 30 minutes and finally centrifuged at 6,000 g for 15 minutes to separate the exfoliated nanosheets. The exfoliated material was harvested from the resulting supernatant for subsequent experiments.

## 3.2 Characterisation

### 3.2.1 Morphology

The size and morphology of the synthesised materials were characterised using a FEI Tecnai T20 Transmission Electron Microscope (TEM) shown in Figure 3.2 (a) or a Philips CM10 TEM with Olympus SIS Megaview G2 Digital Camera at an operating

voltage of 100 kV. Samples were prepared for TEM by placing a 10 µL drop of dilute solution onto formvar coated copper grids (300 mesh) and letting it dry in air. TEM images are created from the collection of transmitted electrons through a sample producing a high resolution 2D image of the sample. Additional scanning electron microscope (SEM) imaging was performed on a Zeiss Supra 55VP SEM shown in Figure 3.2 (b) at 10 kV for samples prepared on both silicon wafer and glass coverslips. SEM images are created from the scattered electrons out of a sample producing a 3D image of the sample but at a lower resolution than TEM. Atomic force microscopy (AFM) measurements were performed on a Digital Instruments Dimension 3100 AFM shown in Figure 3.2 (c). AFM was used to investigate surface morphology, height and mean surface roughness of samples. Samples were prepared by dropcasting onto atomically smooth mica substrates immediately after exfoliation by adhesive tape.

**(a)**                                           **(b)**

**(c)**
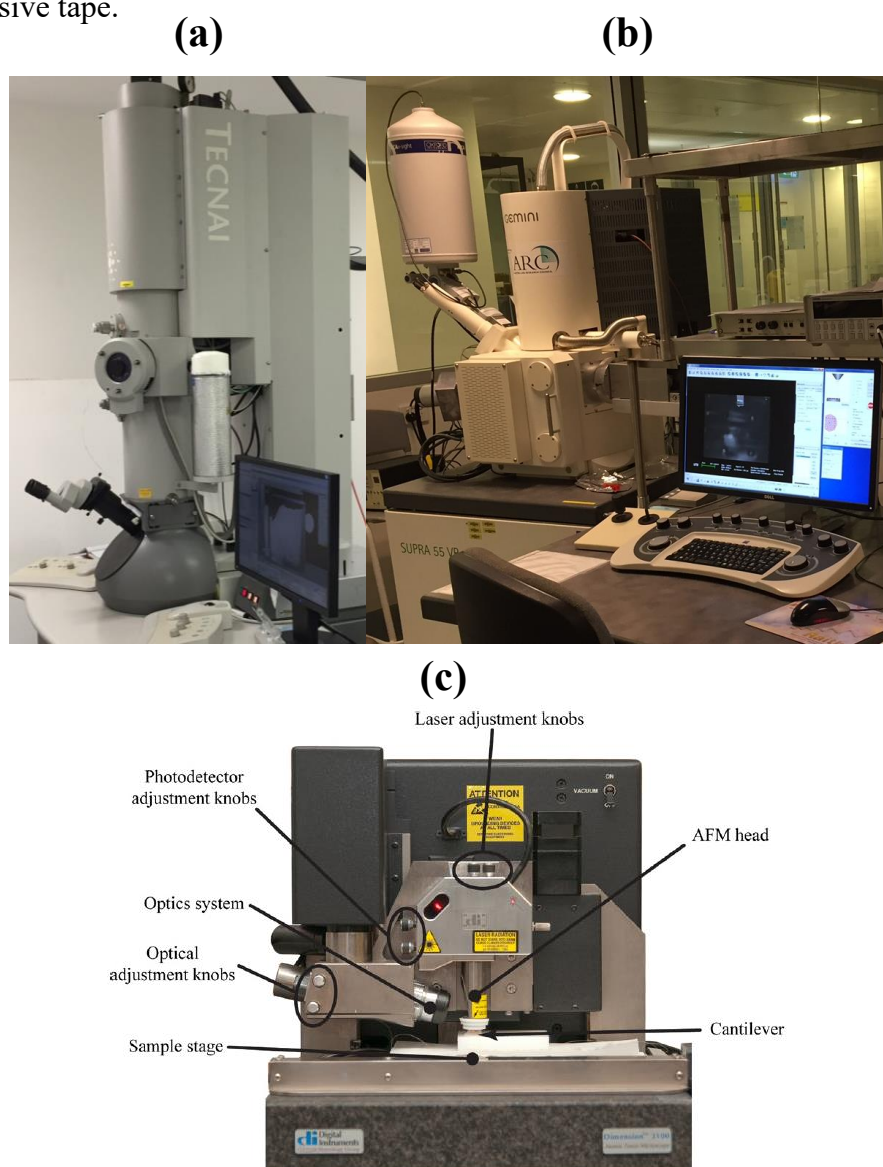
**Figure 3.2** FEI Tecnai T20 Transmission Electron Microscope (a) and Zeiss Supra 55VP SEM (b). Reproduced from [134]. Digital Instruments Dimension 3100 AFM (c). Reproduced from [135].

## 3.2.2    Structural

Element mapping images were collected with an aberration-corrected analytical transmission electron microscope (TEM, JEOL ARM-200F) equipped with a Centurio SSD energy-dispersive X-ray spectroscopy (EDS) detector set at 77 K. The TEM was operated at 80 kV. The line profiles were processed with the LOWESS smoothing algorithm as implemented in OriginPro. Crystallographic information of samples was recorded via X-ray diffraction (XRD) defined by Braggs Law as shown in Figure 3.3 (a) on a Bruker D8 Discover diffractometer pictured in Figure 3.3 (b) with a slit of 0.02° at a scanning speed of 2° min$^{-1}$ using Cu Kα radiation ($\lambda = 1.5406$ Å). The UCNP doping concentrations were determined by inductively coupled plasma mass spectrometry (ICP-MS) using an Agilent 7500cx ICP Quadrupole mass spectrometer.
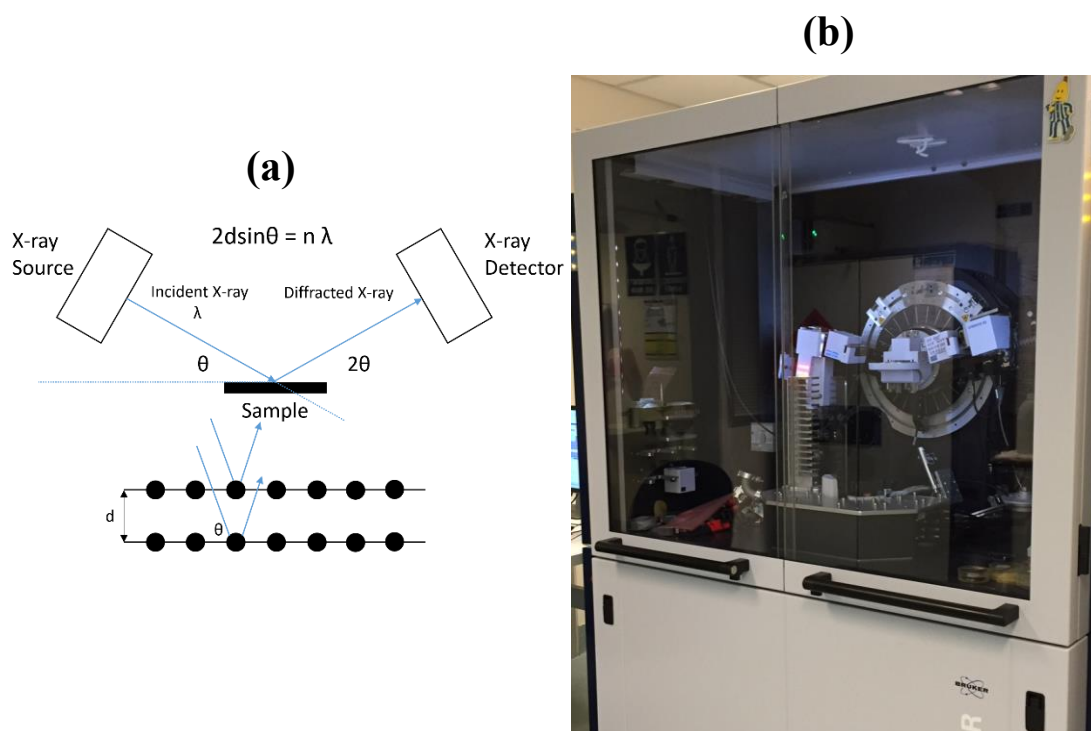


**Figure 3.3** Illustration of X-ray diffraction (a) and Bruker D8 Discover diffractometer (b). Reproduced from [134]

## 3.2.3     Synchrotron Soft X-ray

Information on the chemical structure, bonding environment, band structure and elemental valence in samples were determined by X-ray photoelectron spectroscopy (XPS) and near edge X-ray absorption fine structure (NEXAFS) in three modes of total electron yield (TEY), partial electron yield (PEY) and total fluorescent yield (TFY) [136]. XPS measures the atomic binding energy of a sample at a fixed X-ray photon energy whereas NEXAFS measures the X-ray absorption intensity as a function of X-ray photon energy. The basic operating fundamentals of XPS are shown in Figure 3.4 (a). X-ray photons of energy hv above the work function of the sample irradiate it causing photoelectrons to be emitted which are measured by a detector giving the binding energy of the sample's electrons via the characteristic XPS equation. A typical XPS spectrum is a plot of the number of electrons detected versus the binding energy of the electrons detected. Each element produces a characteristic set of XPS peaks at characteristic binding energy values that directly identifies each element that exists in or on the surface of the sample being analysed. These characteristic spectral peaks correspond to the electron configuration of the atoms present in the sample.

As Figure 3.4 (b) illustrates for NEXAFS the energy of the X-rays is tuned to excite specific core electron orbitals which are commonly referred to as the K, L and M edges. NEXAFS in TEY mode monitors the neutralization current of the grounded sample while TFY mode measures photons that are emitted after electrons of lower binding energy fill created core holes. TFY mode gives information about the bulk sample (~1 μm) due to the long mean free path of the photons while TEY mode probes the surface of a material (~5 nm) due to the short mean free path of the electrons and is sensitive to sample charging. In PEY mode a retarding bias voltage which is applied to the detector set as the starting scan photon energy multiplied by a bias voltage factor (0.5-1), for which the default value is 0.75. This bias prevents low kinetic energy electrons reaching the detector but allows Auger electrons associated with the probed electronic transition to pass through. The retarding voltage blocks secondary electrons which have relatively long inelastic mean free paths. As a result, the surface sensitivity of the PEY mode is higher than the TEY mode, with a sampling depth of only the first few nanometres.
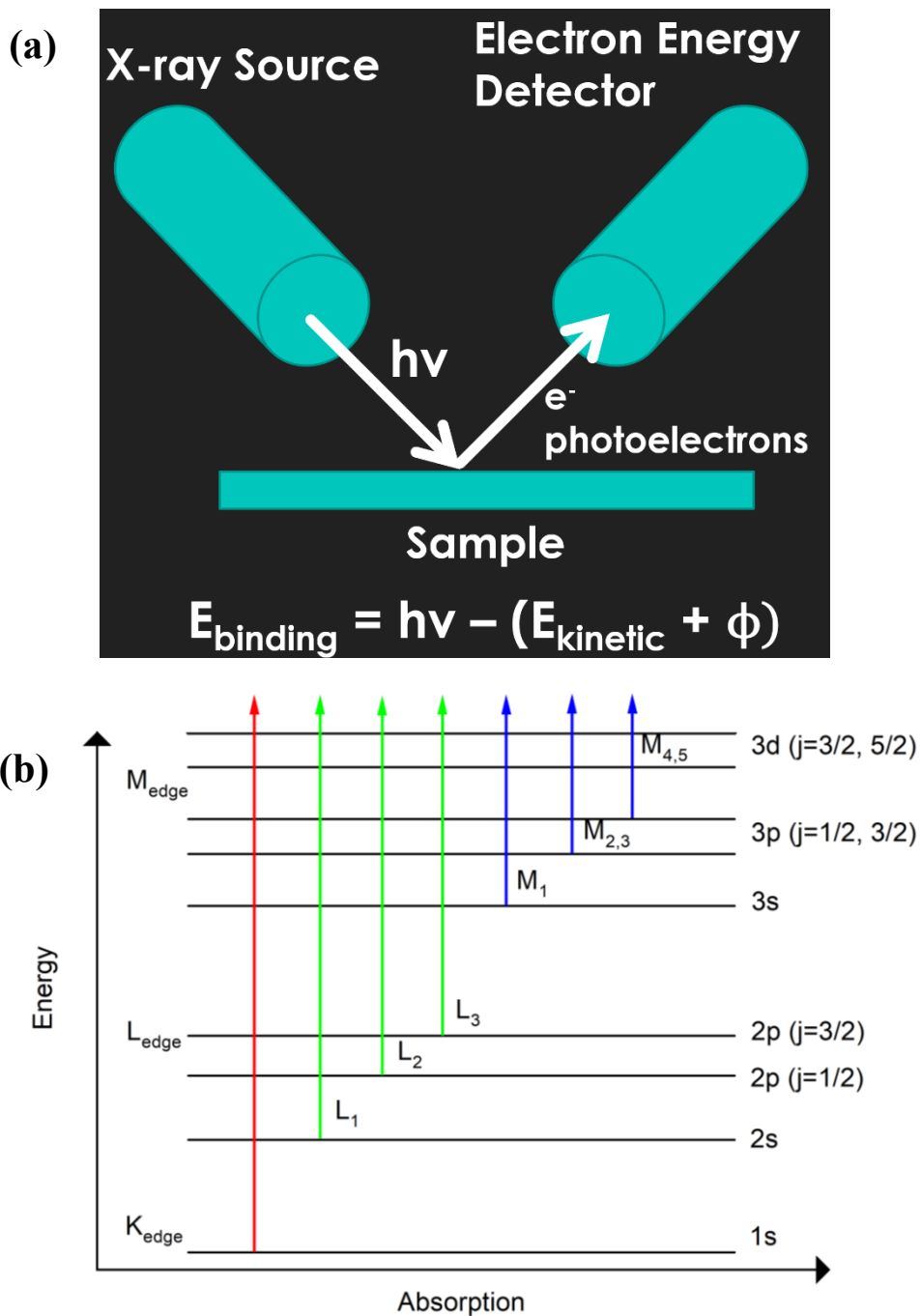
**Figure 3.4** Illustration of XPS process where $E_{binding}$ is the binding energy of the electron, hv is the energy of the X-ray photons being used, $E_{kinetic}$ is the kinetic energy of the electron as measured by the electron energy detector and $\varphi$ is the work function dependent on the kinetic energy given up by the photoelectron to become absorbed by the electron energy detector (a). Illustration of NEXAFS absorption edges from excitation of corresponding core electrons (b).

XPS and NEXAFS were performed on the soft X-ray spectroscopy beamline at the Australian Synchrotron as shown in Figure 3.5 (a,b). Samples were dropcast on clean test grade silicon wafer (0.010 - 0.018 ohm/cm) and loaded into the analysis chamber at ultrahigh vacuum ($\sim 10^{-10}$ mbar) for data acquisition.

XPS spectra collected on the soft X-ray beamline were calibrated to a polycrystalline Au reference. Survey scans were performed using an X-ray photon energy of 1486 eV, which is equal to the Al K$\alpha$ energy. XPS narrow scans were performed using X-ray photon energies in the regions of interest such as the Y 3d core level and the Yb 4d core level (200 - 140 eV) with an energy step size of 0.1 eV. Valence band XPS scans were performed at 150 eV to probe the valence band edge. Narrow scan photoelectron data was collected in the same photoelectron energy window under identical acquisition conditions with each spectrum having a fitted Shirley background removed and the peak intensities extracted by Gaussian peak fitting. The integrated area ratio was plotted against photoelectron kinetic energy. The inelastic electron mean free path of the photoelectrons was calculated using the QUASES-IMFP-TPP2M Ver.3.0 software [137, 138].

For determining dopant distribution via NEXAFS spectra inspection of the energy position of gold related photoelectron lines within the scanning window with respect to the retarding potential of the PEY detector was performed. For the retarding potential used all the Au photoelectron lines are outside the scanning window of interest for Yb and Er (1400 - 1530 eV) [139]. The closest Au line is the 4s line at 763 eV. Additionally, the peak intensities of the Er and Yb absorption peaks were used without any contribution from the spectral background.
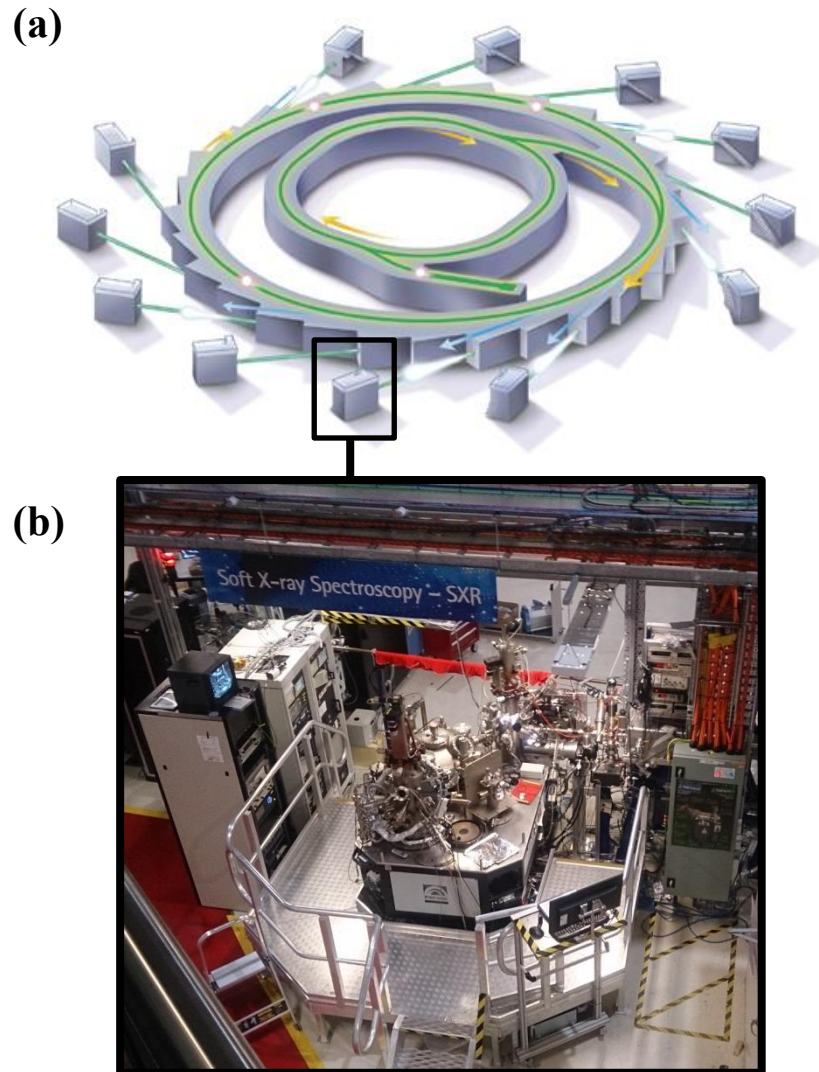
**Figure 3.5** A typical synchrotron set-up is displayed a number of experimental stations are attached to the main beamline (a). Reproduced from [140]. X-ray radiation is produced from electrons being accelerated to almost the speed of light which are deflected through magnetic fields. The resulting radiation is channelled off to beamlines for various characterisation techniques. This how the Australian Synchrotron in Clayton, Victoria is set-up and pictured is the Soft X-ray Spectroscopy station where measurements were performed (b).

## 3.2.4　　Optical

UV-Vis measurements were performed on a Cary 7000 universal measurement spectrophotometer calibrated to a single baseline to determine optical reflection and transmission of samples. Raman and photoluminescence spectra were acquired from samples on $Si/SiO_2$ substrates using a Horiba LabRAM HR Evolution Raman spectrometer with 532 nm and 785 nm laser lines at 0.5 mW laser power. Upconversion emission spectra in the range of 200 nm - 1000 nm from samples in solution was measured using an optical system (optical path shown in Figure 3.6) with a 5 W Leo Optics 976 nm laser and OceanOptics QE65000 spectrometer attached. Samples were measured in UV quartz cuvettes.
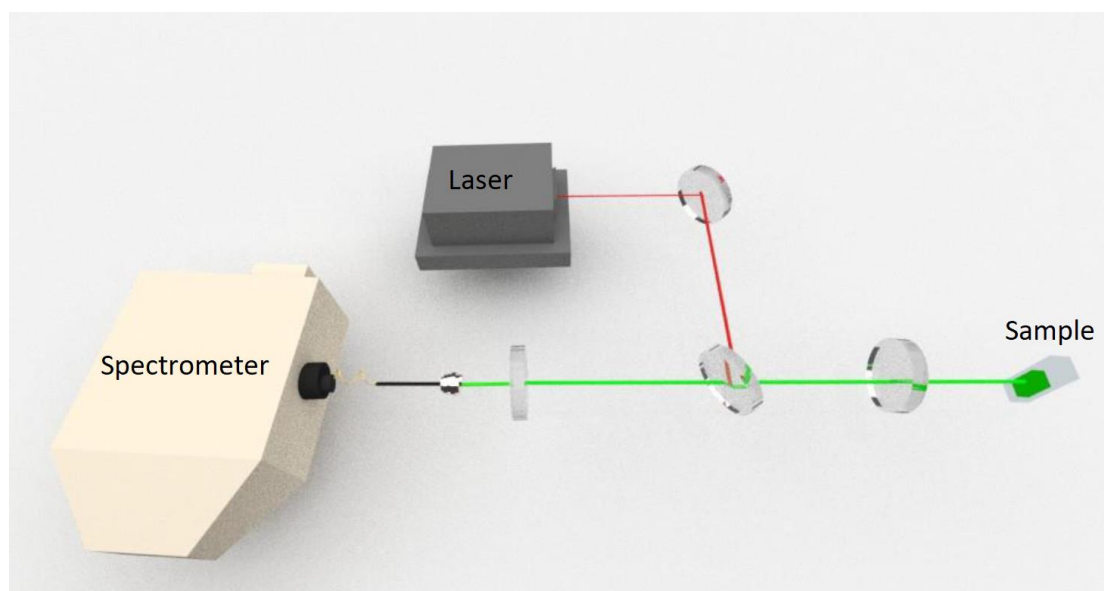


**Figure 3.6** Schematic set-up of the custom system for measuring upconversion emission spectra from samples in solution. Reproduced from [35].

A scanning confocal microscope system (optical path and image of set-up shown in Figure 3.7) equipped with a fiber-coupled 976 nm single mode polarized diode laser focused through a 100x objective lens (NA 1.4) was used to measure the upconversion emission and lifetime of single UCNPs at low power (20 mW which was measured at the objective back aperture). The emitted light from a sample was collected by the same objective lens, which was refocused into an optical fiber having a core size of 50 μm matching the first Airy disk of the system. A single photon counting avalanche diode (SPAD) detector was connected to the collection optical

fiber to detect the emission intensity. The scanning was achieved by the moving of a 3D piezo stage and lifetime was fitted to a double decay exponential function. For each sample values were averaged to give mean intensity and lifetime.
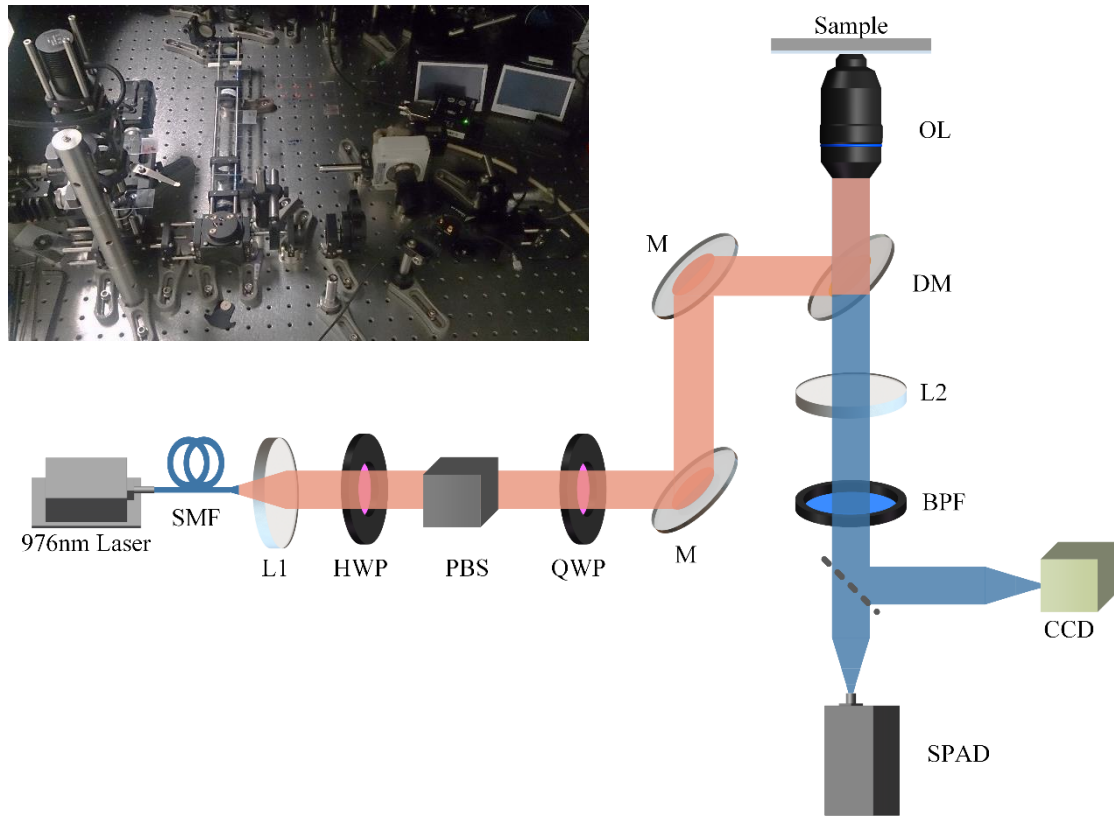


**Figure 3.7** Schematic set-up of the custom confocal scanning microscope with inset of experimental system. SMF, single-mode fiber; L1, collimation lens; HWP, half-wave plate; PBS, polarized beam splitter; QWP, quarter-wave plate; M, mirror; DM, dichroic mirror; OL, objective lens; L2, collection lens; BPF, band pass filter; SPAD, single-photon avalanche diode; CCD, charge coupled device.

# 3.3    Simulation

## 3.3.1    Rate Equation

Applied from previous work [44] to investigate quantum efficiency enhancement due to internal defect reduction in NaYF$_4$: Yb$^{3+}$, Er$^{3+}$ upconversion nanocrystals a simplified energy level diagram as shown in Figure 3.8 was considered that involves

two energy levels associated with the sensitizer $Yb^{3+}$ ions ($^2F_{7/2}$ and $^2F_{5/2}$, represented as S1 and S2, respectively). Assuming: (a) the excitation photons are absorbed by $Yb^{3+}$ only and (b) energy transfer happens between $Yb^{3+}$ on the excited level and $Er^{3+}$ on both the ground and the intermediate levels, the following independent rate equations can be obtained.

$$\frac{dn_1}{dt} = -c_1 n_1 n_{S2} + (A_2 + W_2)n_2 + (1-b)A_3 n_3$$

$$\frac{dn_2}{dt} = c_1 n_1 n_{S2} - c_2 n_2 n_{S2} - (A_2 + W_2)n_2 + (bA_3 + W_3)n_3$$

$$\frac{dn_3}{dt} = c_2 n_2 n_{S2} - (bA_3 + W_3)n_3$$

$$\frac{dn_{S2}}{dt} = P_{980} n_{S1} - A_S n_{S2} - (c_1 n_1 + c_2 n_2)n_{S2}$$

where $P_{980}$ is the absorption rate of $Yb^{3+}$, $A_S$ is the intrinsic decay rate of excited $Yb^{3+}$ ions, $c_i$ is the upconversion coefficient between excited $Yb^{3+}$ ions and $Er^{3+}$ ions on level i, $A_i$ is the radiative decay rate of $Er^{3+}$ ions on level i, $W_i$ is the non-radiative decay rate of $Er^{3+}$ ions on level i (this parameter will be affected by the internal defect density), b is the branching ratio for $Er^{3+}$ ions decaying from level 3 to level 2 and n is the population of ions on an energy level satisfying

$$n_1 + n_2 + n_3 = 1$$

$$n_{s1} + n_{s2} = 1$$

The system of equations is solved from $t = 0$ to $t = t_f$, where $t_f$ depends on the longest lifetime in the system. The numerical solution of the total system of equations is the population of each energy level as a function of time. The quantum efficiency can then be achieved from the emission ratio and absorption ratio.
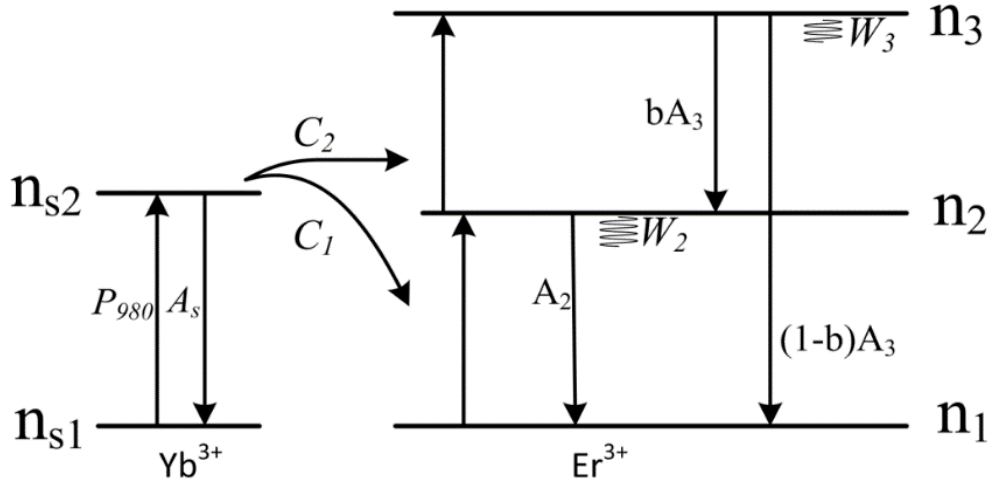
**Figure 3.8** Simplified energy level diagram used for rate equation simulation.

## 3.3.2    Density Functional Theory

Calculations were performed using density functional theory (DFT) as implemented in the Vienna Ab initio Simulation Package (VASP) using the Hubbard interaction term (DFT+U) [141]. A plane-wave pseudopotential approach was used with the energy cut-off set to 400 eV - 700 eV. A generalised gradient approximation (GGA) in the Perdew-Burke-Ernzerhof (PBE) form was used [142], with the ion-electron interaction defined using the projector augmented wave (PAW) method [143]. A k-point mesh of $10 \times 10 \times 1$ and $1 \times 8 \times 8$ was used for geometry optimisations and density of states. For the calculation of the cleavage energy, the effect of the van der Waals (vdW) interaction was accounted for in the calculation by including Grimme's D3 vdW correction [144]. The electronic self-consistent calculation was performed with an energy tolerance of $10^{-7}$ eV - $10^{-6}$ eV and the atomic relaxation was performed with a force tolerance of $10^{-2}$ eV/ Å - 0.03 eV/ Å. The Bader partial charges were calculated according to the procedure outlined by Henkelman et al. [145] and implemented in VASP. In order to reproduce the experimental band gap of bulk $\beta$-NaYF$_4$, the procedure outlined in [51], in which the empirical Hubbard U term was added to the total Kohn-Sham energy was adopted. A value of U of 5.0 eV for the 4f orbital of Y and a value of 4.2 eV for the 2p orbital of F was used.

# Chapter 4

# Depth Profiling of NaYF$_4$ UCNPs by Synchrotron Techniques

## 4.1      Introduction

Understanding of how lanthanide dopants distribute within UCNPs is crucial for effectively applying enhancement methods to increase their efficiency. Unfortunately, it is commonly assumed that sensitizer and activator lanthanide ions are uniformly distributed within the NaYF$_4$ crystal.

It is known that surface dopant ions show weaker luminescence emission intensities compared to interior dopant ions due to quenching from surface defects, impurities, ligands and solvents [146-148]. The heterogeneous distribution of Yb$^{3+}$ within UCNPs is also known to deteriorate emission brightness and decay lifetime while the decreased distance between activators in UCNPs with high doping concentrations can also lead to induced self-quenching from cross-relaxation mechanisms [149-151] and amplified stimulated emissions [44]. These reports announce that systematic characterisation of the dopant distribution in host NaYF$_4$ UCNPs will lead to a better understanding of upconversion luminescence mechanisms and methods for enhancement.

In this chapter the distribution of lanthanide ions within the NaYF$_4$ nanocrystal is quantitatively determined. The hypothesised Yb$^{3+}$ distribution within UCNPs of different sizes and concentrations is characterised by the ratio of Yb$^{3+}$/Y$^{3+}$ at different depths from the surface to the centre of the UCNPs by measuring Yb and Y photoemissions over a range of X-ray photon energies via specially tailored

synchrotron XPS [68, 152], EDS [66], NEXAFS and ICP-MS techniques. Clarke as second author was the primary investigator for designing the optical and chemical analysis experiments as well as collecting, analysing and interpreting results from these experiments

# 4.2 Lanthanide Distribution

## 4.2.1 Hypothesis

It has been reported that by controlling the heating rate and conditions during the synthesis of $NaYF_4$: 20% $Yb^{3+}$, 4% $Tm^{3+}$ UCNPs that the range in size can vary from 13.0 nm - 43.0 nm. Surprisingly the smaller UCNPs were found to have a higher emission efficiency than the larger UCNPs [59]. In a parallel investigation, UCNPs with higher concentrations of $Yb^{3+}$, coated with an $NaYF_4$ inert shell, displayed enhanced upconversion luminescence [23].

To explain these phenomena apart from the high internal crystal quality obtained from well-controlled synthesis conditions, these findings led to the hypothesis that the sensitizer ions' distribution across the host UCNPs may also be non-uniform. This hypothesis is illustrated in Figure 4.1, when the UCNPs are doped with a fixed concentration of 20% $Yb^{3+}$ ions, as $Yb^{3+}$ has a relatively higher nucleation energy compared with the host $Y^{3+}$ ions, the $Yb^{3+}$ ions are expected to concentrate in the centre of the UCNPs and radically decrease in concentration towards the surface in ratio to the host $Y^{3+}$ ions. This distribution regardless of the size would explain why the smaller UCNPs have a higher upconversion emission efficiency than the larger ones as they have a greater portion of their $Yb^{3+}$ ions in the centre avoiding surface quenching effects. Accordingly, when the doping concentration of the $Yb^{3+}$ ions increases in each UCNP, it is expected that the $Yb^{3+}$ ions would distribute in a similar manner, albeit with a steeper gradient for successively higher doping concentrations.
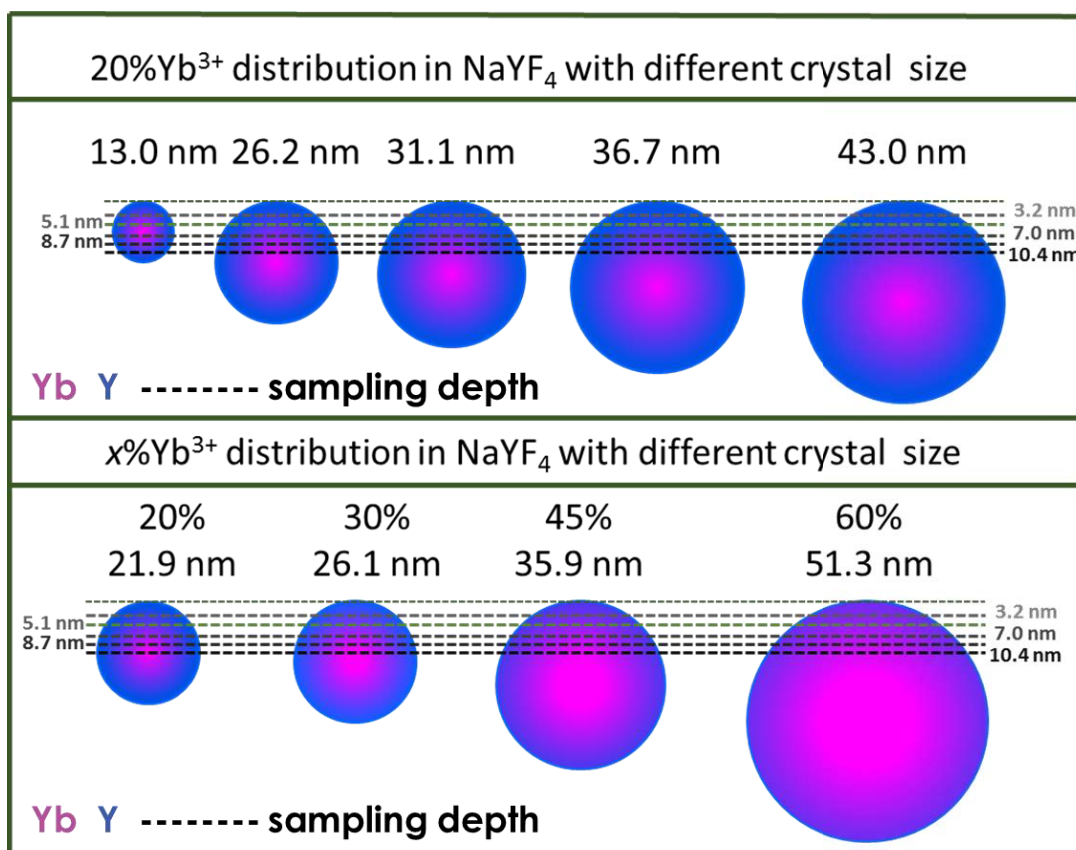
**Figure 4.1** Diagram of the hypothesised $Yb^{3+}$ distribution within $NaYF_4$ UCNPs as a function of XPS sampling depth. The $Yb^{3+}$ distribution within the $NaYF_4$ UCNPs of varying size and $Yb^{3+}$ concentration can be measured by the XPS ratio of $Yb^{3+}/Y^{3+}$ photoemissions as a function of depth using tuneable energy synchrotron XPS. The dashed lines indicate the available range of XPS sampling depths relative to the UCNP sizes.

## 4.2.2 Morphology

UCNPs for this investigation were synthesised using the one pot solvothermal method [23, 59]. Figure 4.2 shows the TEM images of the as synthesised UCNPs the result of controlled heating rate (a-e) and varied $Yb^{3+}$ doping concentration (f-i). As shown in the images the synthesis procedure produces highly uniform UCNPs that were measured as being pure hexagonal phase via XRD [59]. The doping concentration of $Tm^{3+}$ was fixed at 4% for all UCNPs. Figure 4.2 (a-e) shows the fixed 20% $Yb^{3+}$ doped UCNPs with varying sizes of 13.0 nm, 26.2 nm, 31.1 nm, 36.6 nm and 43.0 nm. Figure 4.2 (f-i) shows the $x$%$Yb^{3+}$ UCNPs of sizes: 21.9 nm, 26.1 nm, 35.9 nm, 51.3 nm; with x = 20%, 30%, 45% and 60% $Yb^{3+}$, respectively.
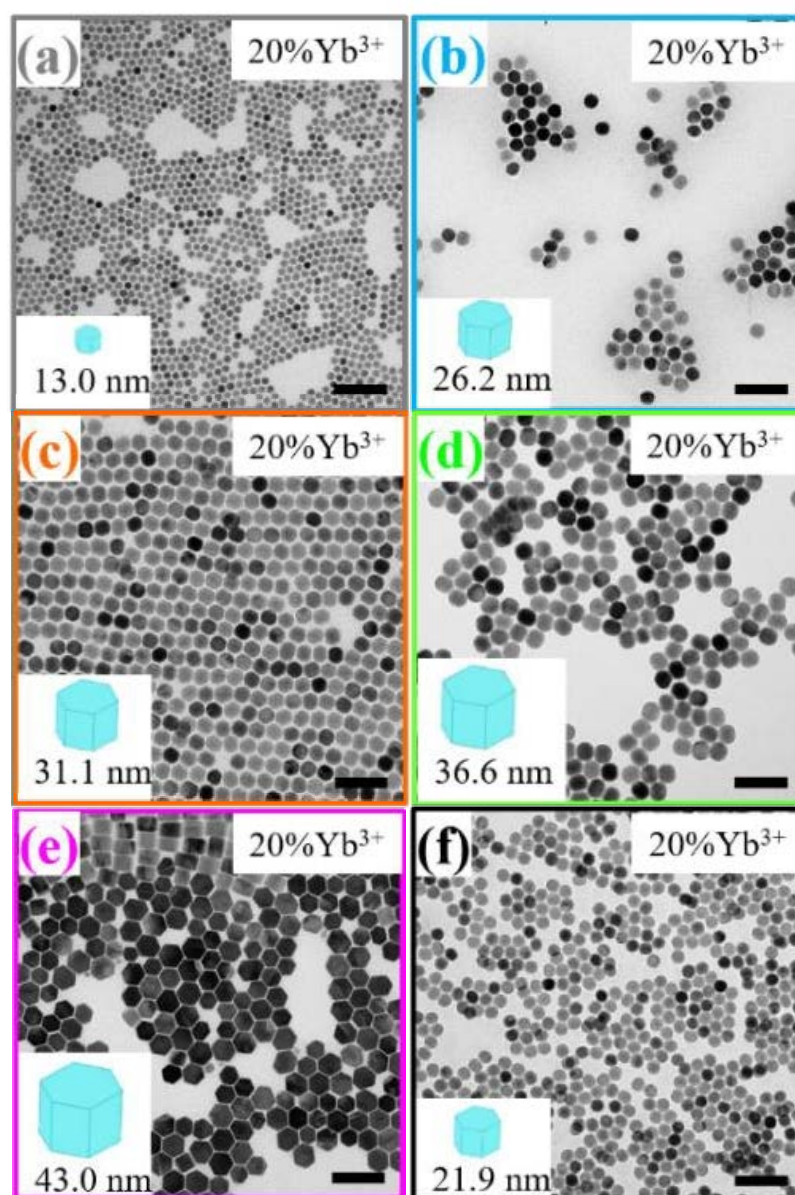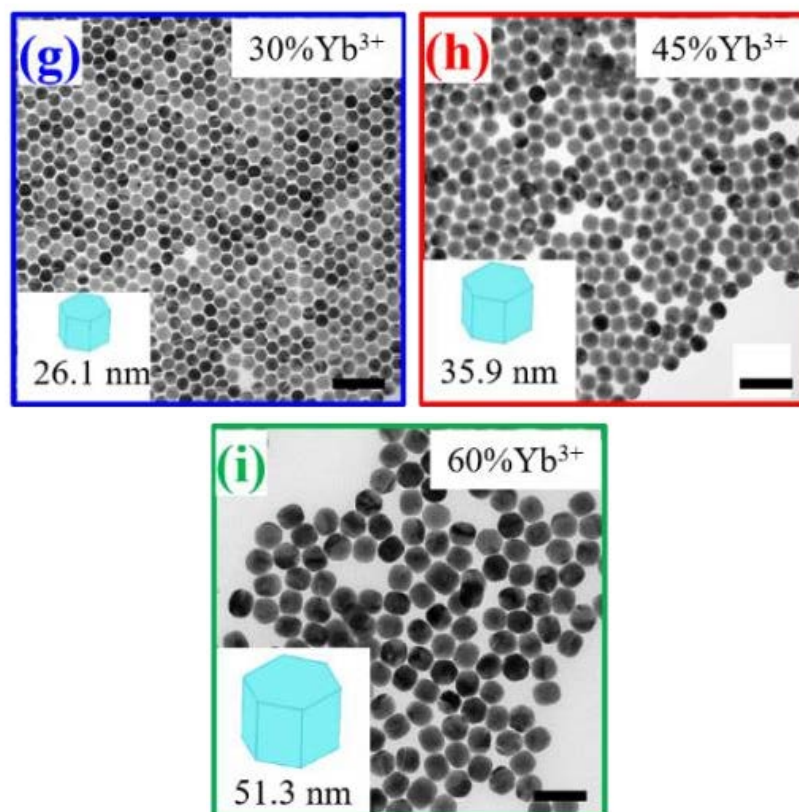
**Figure 4.2** TEM images of NaYF$_4$:x%Yb$^{3+}$,4%Tm$^{3+}$ upconversion nanoparticles used for the lanthanide distribution investigation with different sizes of 13.0 nm, 26.2 nm, 31.1 nm, 36.6 nm and 43.0 nm respectively (a–e) and Yb$^{3+}$ doping concentrations: 20%, 30%, 45% and 60% of size: 21.9 nm, 26.1 nm, 35.9 nm and 51.3 nm respectively (e–i). The black scale bar in each image is 100 nm.

## 4.2.3    Synchrotron Analysis

### 4.2.3.1    Survey Spectra

XPS survey scans were performed on the UCNPs to identify all characteristic elements. Figure 4.3 is the XPS survey spectra for three of the UCNP samples. In each survey all elements of the UCNPs except for Tm are present with Na, Y, Yb and F able to be identified from their distinct photoelectron emissions at the X-ray photon

energy excitation (hν) of 1486 eV. The absence of Tm within the spectra is due to the low concentration in the UCNP samples and overlapping photoelectron emissions.
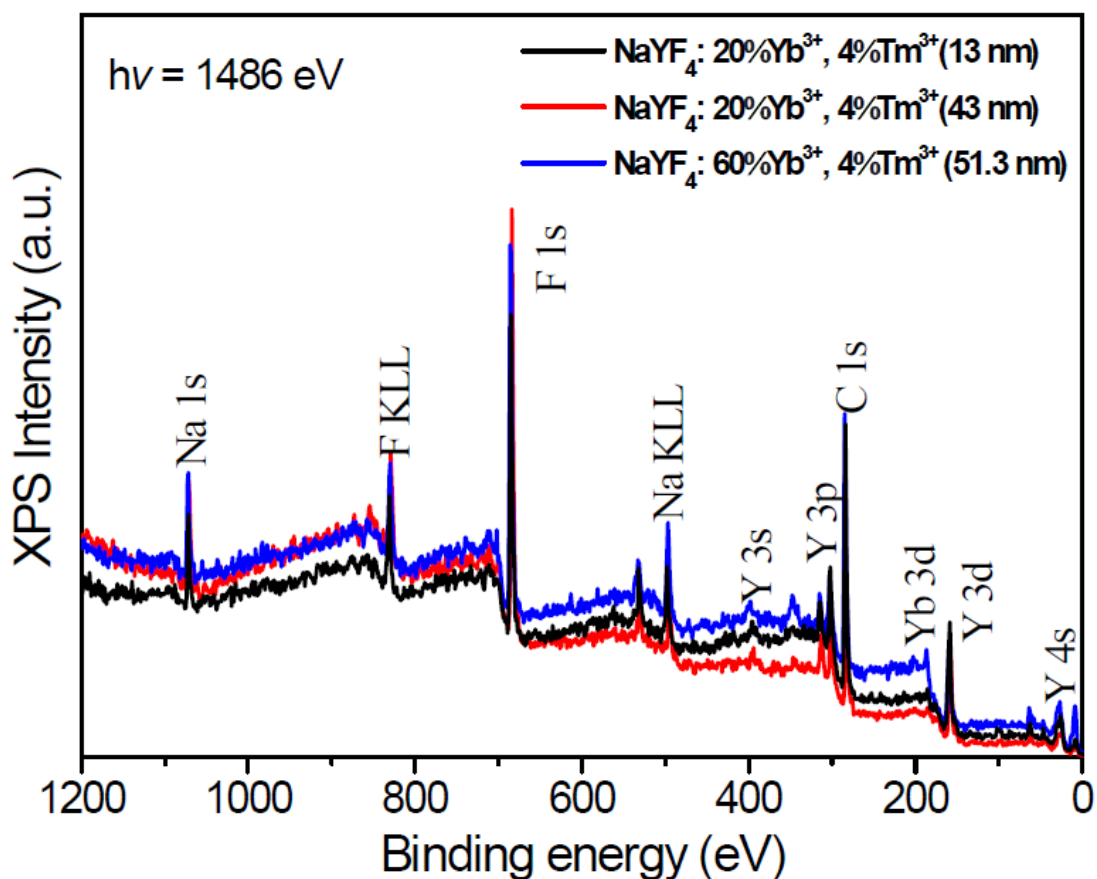


**Figure 4.3** XPS survey spectra for the $NaYF_4$ UCNPs acquired at a photon energy of 1486 eV.

## 4.2.3.2     Depth Profiling Spectra

XPS depth profiling is tuning of the inelastic mean free path dependent sampling depth of the XPS measurement by adjusting the X-ray photon energy. By restricting the binding energy range of the scan to a narrow region a higher resolution XPS scan can be obtained of the photoelectron emissions of interest. Figure 4.4 shows the depth resolved XPS spectra of the narrow binding energy region containing the Y 3d, Yb 4d and Si 2s core levels collected from 20% $Yb^{3+}$ (13.0 nm), 20% $Yb^{3+}$ (31.1 nm) and 60% $Yb^{3+}$ (51.3 nm) $NaYF_4$ UCNPs at X-ray photon energies of 590 eV, 990 eV and 1790 eV. The clear variations in the relative intensities of the Yb and Y

photoemissions with increasing sampling depth can be related to an inhomogeneous distribution of these elements within the nanocrystals.

In all the spectra shown in Figure 4.4, the binding energies of the doublet peaks of the Y 3d split spin-orbital core level occurring from the two possible spin states match the reported values of ~159 eV and ~161 eV respectively for the Y $3d_{5/2}$ and Y $3d_{3/2}$ peaks [68, 152]. The binding energy of the Yb 4d core level also matches the reported values of ~185 eV [153]. The Si 2s peak at around ~153 eV results from the silicon wafer used as the substrate for the experiment which is unfortunately overlapping with the Tm peak preventing its measurement.

At an X-ray photon energy of 590 eV and thus the shallowest sampling depth the Yb 4d peak is absent. However, at a photon energy of 990 eV the Yb 4d peak appears. At 1790 eV the relative intensity ratio of the Yb 4d peak to the Y 3d doublet increases further. This X-ray photon energy range from 590 eV - 1790 eV, corresponds to a sampling depth range within the UCNPs from 3.2 nm - 8.7 nm. These results indicate that all the UCNPs have a higher concentration of $Yb^{3+}$ towards the crystal core.
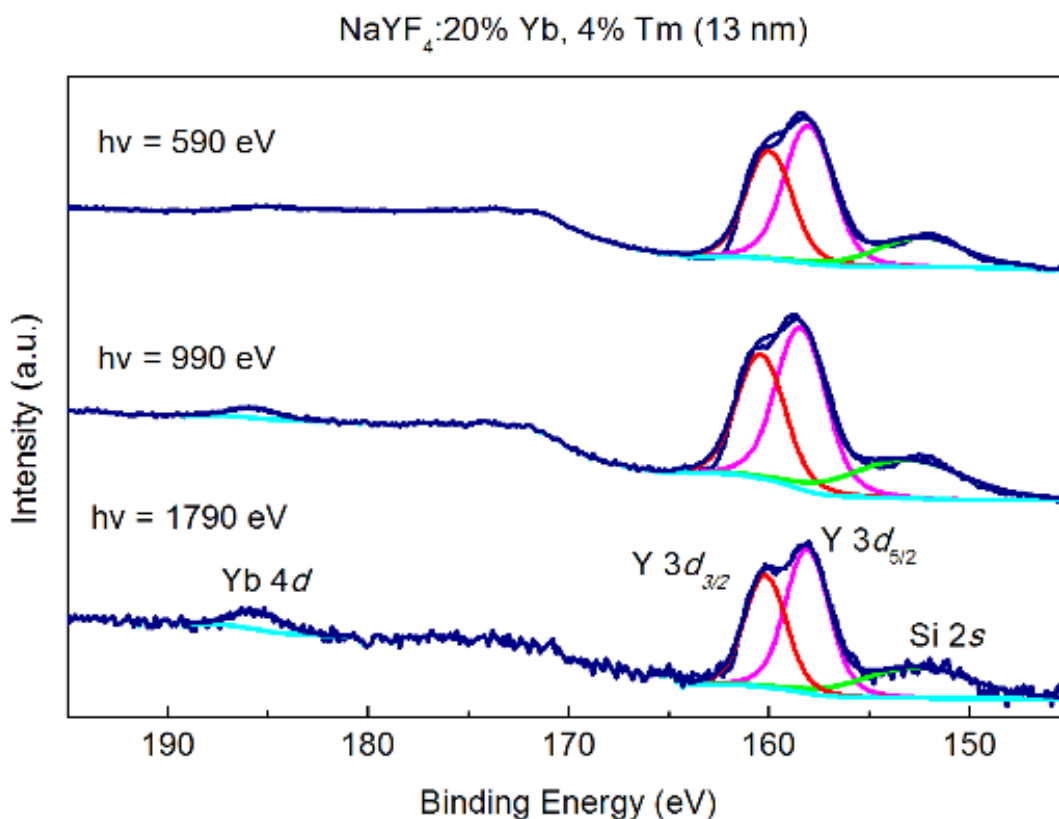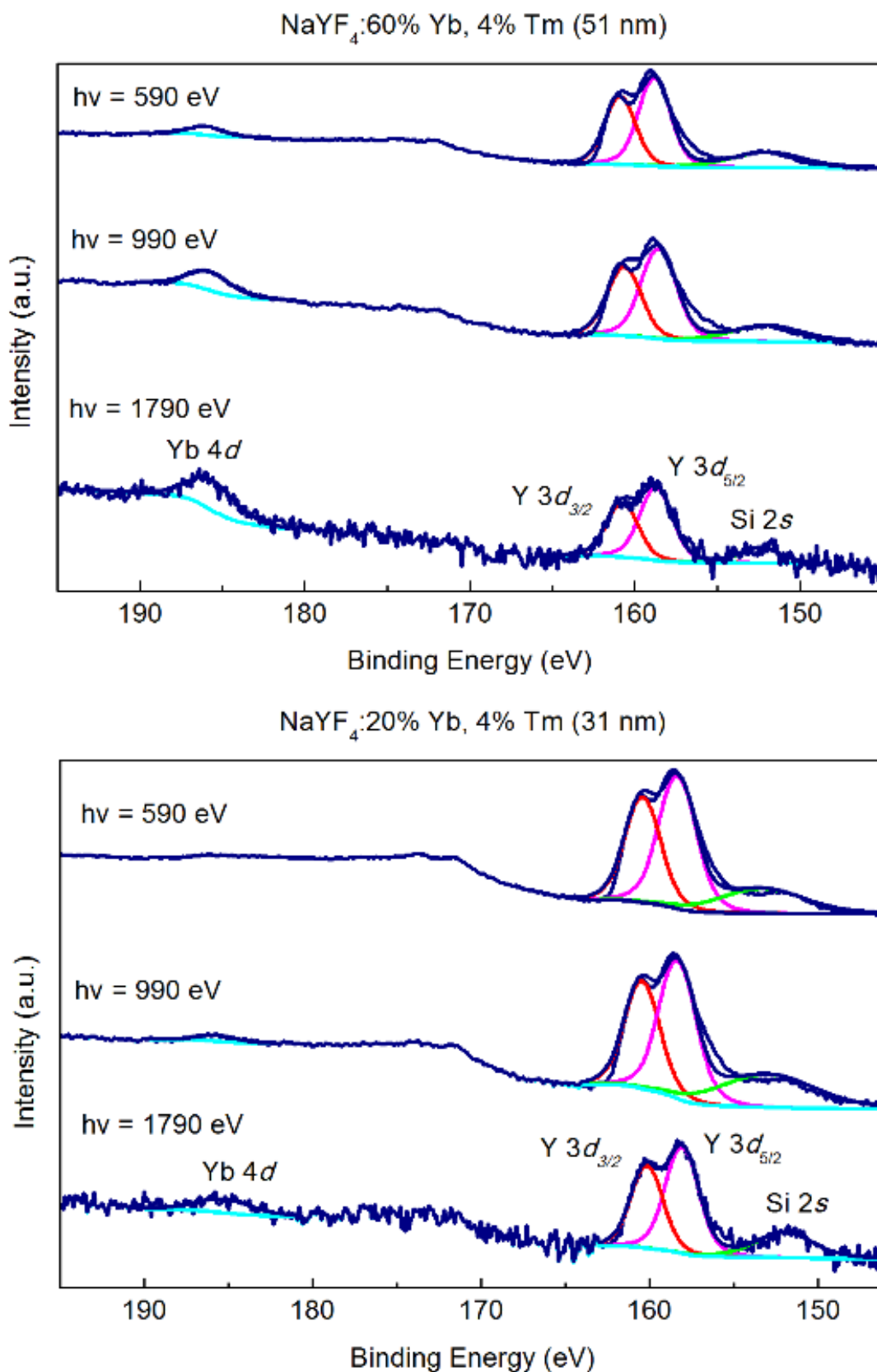
**Figure 4.4** The fitted variable X-ray photon energy XPS spectra of three UCNP samples with different size and Yb$^{3+}$ concentration showing across all samples the consistent increase in ratio of Yb/Y as X-ray photon energy increases.

To quantitatively determine the distribution of the $Yb^{3+}$ dopant ions within the $NaYF_4$ UCNPs, the ratio of the Yb 4d and Y 3d core levels was calculated using the peak area and plotted as a function of the electron kinetic energy and effective sampling depth after correction by the relevant photoionization cross sections [154].

Figure 4.5 (a) shows the intensity ratio of the Yb 4d and Y 3d peaks from $NaYF_4$: 20% $Yb^{3+}$ UCNPs with varying sizes. The increase in the Yb 4d/Y 3d ratio is consistent for all 20% $Yb^{3+}$ doped $NaYF_4$ UCNPs even though their size varies from 13.0 nm - 43.0 nm, indicating that the $Yb^{3+}$ ions concentrate in the crystal interior and gradually decrease from the centre to the surface in ratio to the host $Y^{3+}$ ions. As the gradient trend of the slopes are similar, it can be determined that the distribution from the centre to the surface should be the same. It is notable at the initial sampling depth of 3.2 nm the intensity ratio of Yb 4d to Y 3d for the 13 nm UCNPs is higher than the other sized UCNPs. This is due to this initial sampling depth being closer to the centre of these smallest 13 nm UCNPs where $Yb^{3+}$ ions are more highly concentrated.

Figure 4.5 (b) shows the intensity ratio of Yb 4d/Y 3d in $NaYF_4$ UCNPs with 20%, 30%, 45% and 60% $Yb^{3+}$ respectively. The general increase of the ratio with increasing sampling depth further indicates that $Yb^{3+}$ ions concentrate in the centre of the UCNP and decrease towards the surface. As the concentration of $Yb^{3+}$ increases in the UCNPs, the gradient of the $Yb^{3+}/Y^{3+}$ ratio becomes steeper, indicating comparatively more $Yb^{3+}$ at the same depth.

**(a)**
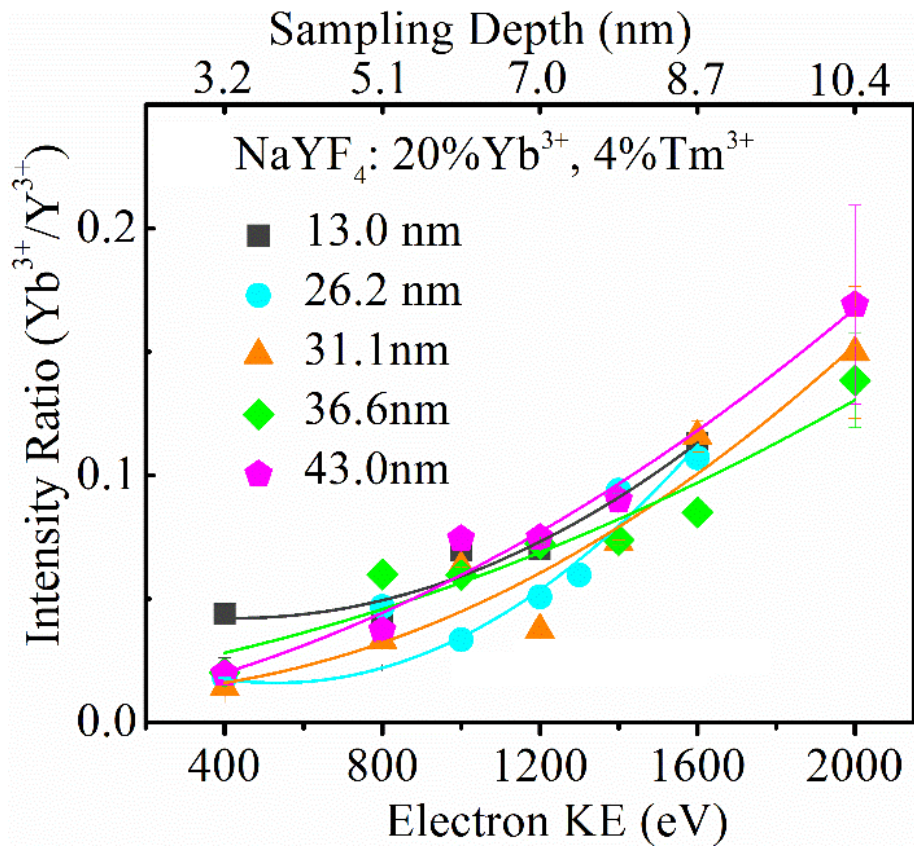
**(b)**
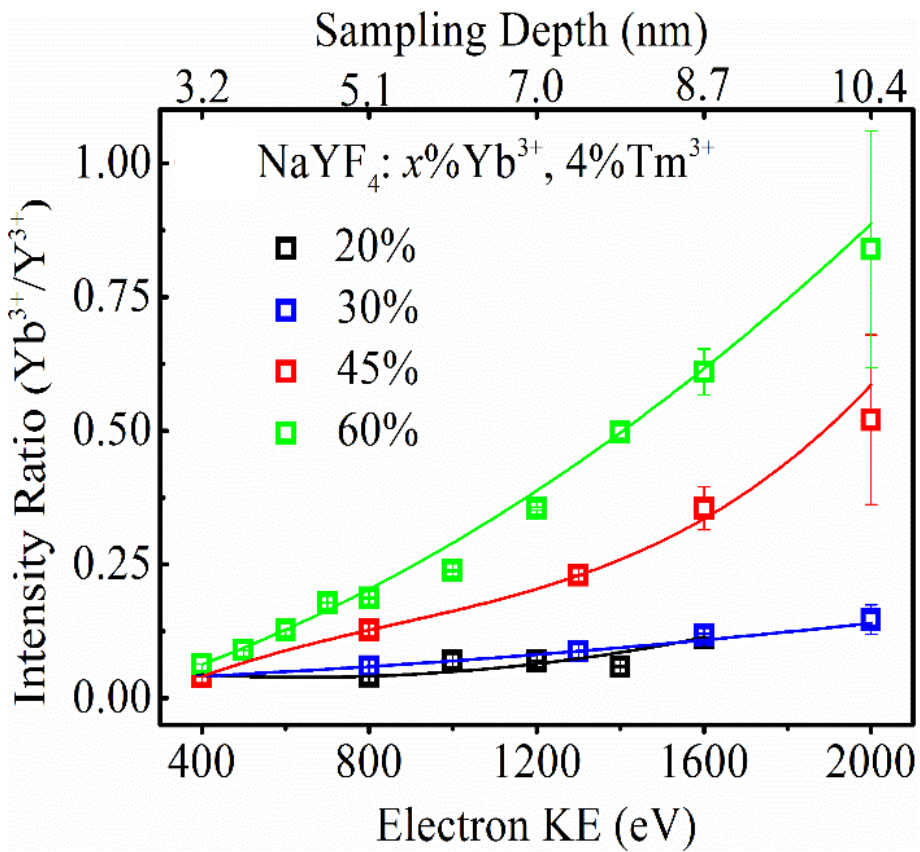
**Figure 4.5** The $Yb^{3+}/Y^{3+}$ ratio within UCNPs as a function of X-ray photon energy/sampling depth is shown for $NaYF_4$: 20% $Yb^{3+}$ UCNPs with sizes of 13.0 nm, 26.2 nm, 31.1 nm, 36.6 nm and 43.0 nm (a) and $NaYF_4$ UCNPs containing 20% $Yb^{3+}$, 30% $Yb^{3+}$, 45% $Yb^{3+}$ and 60% $Yb^{3+}$ with sizes of 21.9 nm, 26.1 nm. 35.9 nm and 51.3 nm, respectively (b).

## 4.2.3.3    Oxidation State

Due to the overlapping photoelectron emissions in the XPS measurements, NEXAFS in TEY mode was performed across the M-edge of both Tm and Yb. NEXAFS spectra of Figure 4.6 and Figure 4.7 overlayed with a calibrated reference foil confirm both the presence of Tm within the UCNPs and that both Yb and Tm are in the 3+ oxidation state, their main oxidation state and the same state as the Y ions in the host $NaYF_4$ UCNP.
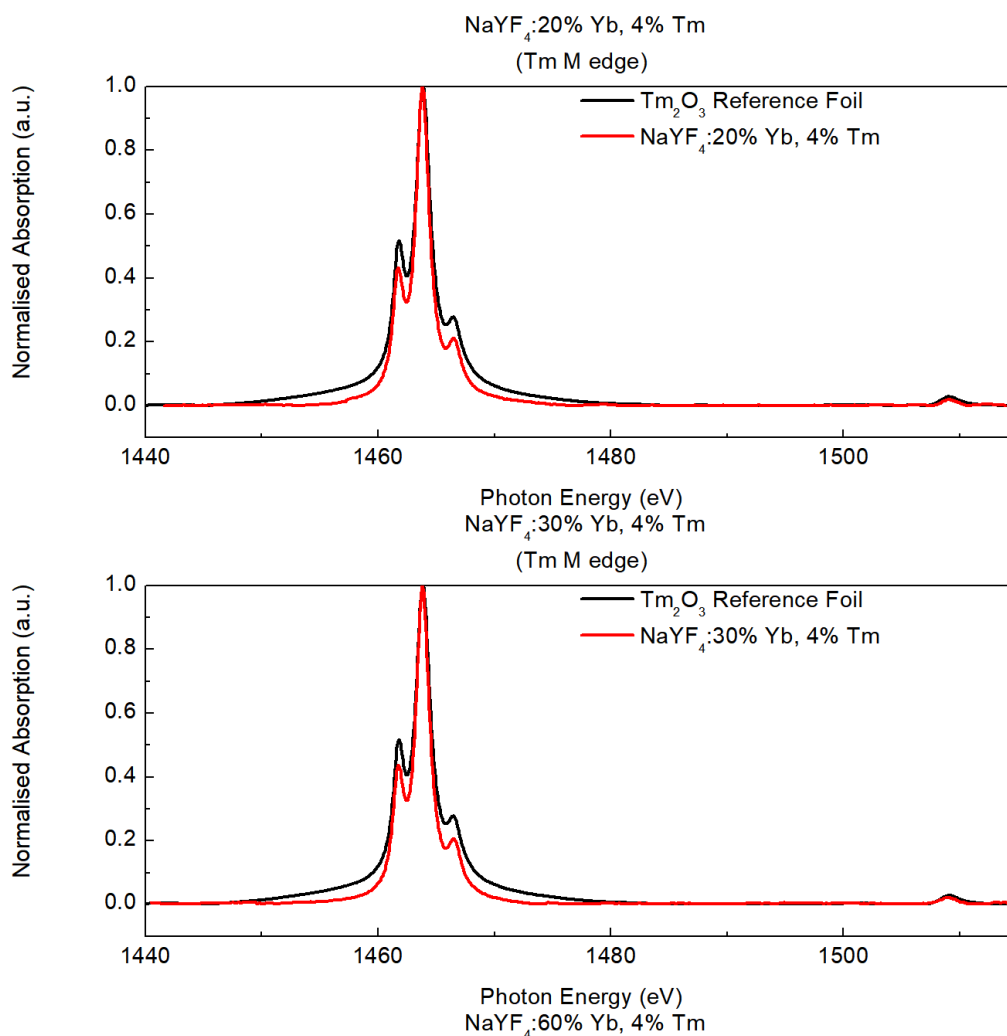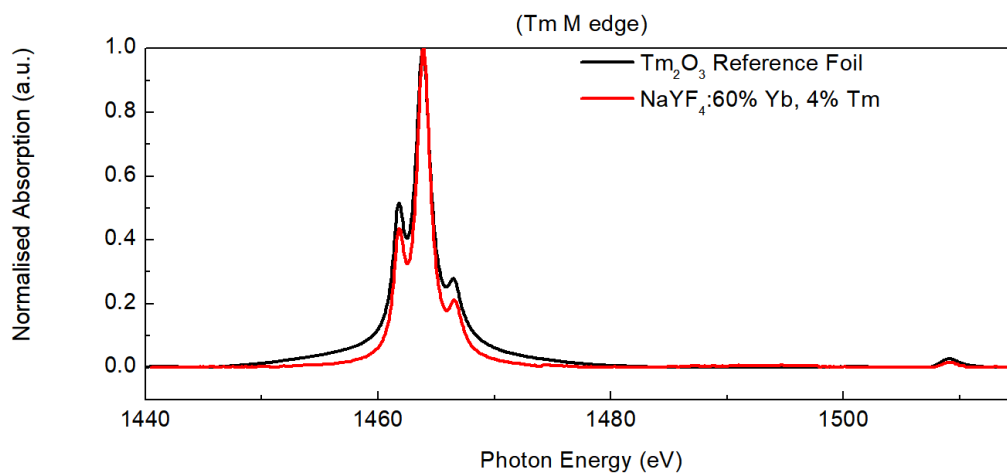
**Figure 4.6** Normalised Tm M-edge TEY NEXAFS spectra of three UCNPs samples superimposed with respective Tm$_2$O$_3$ reference foil.
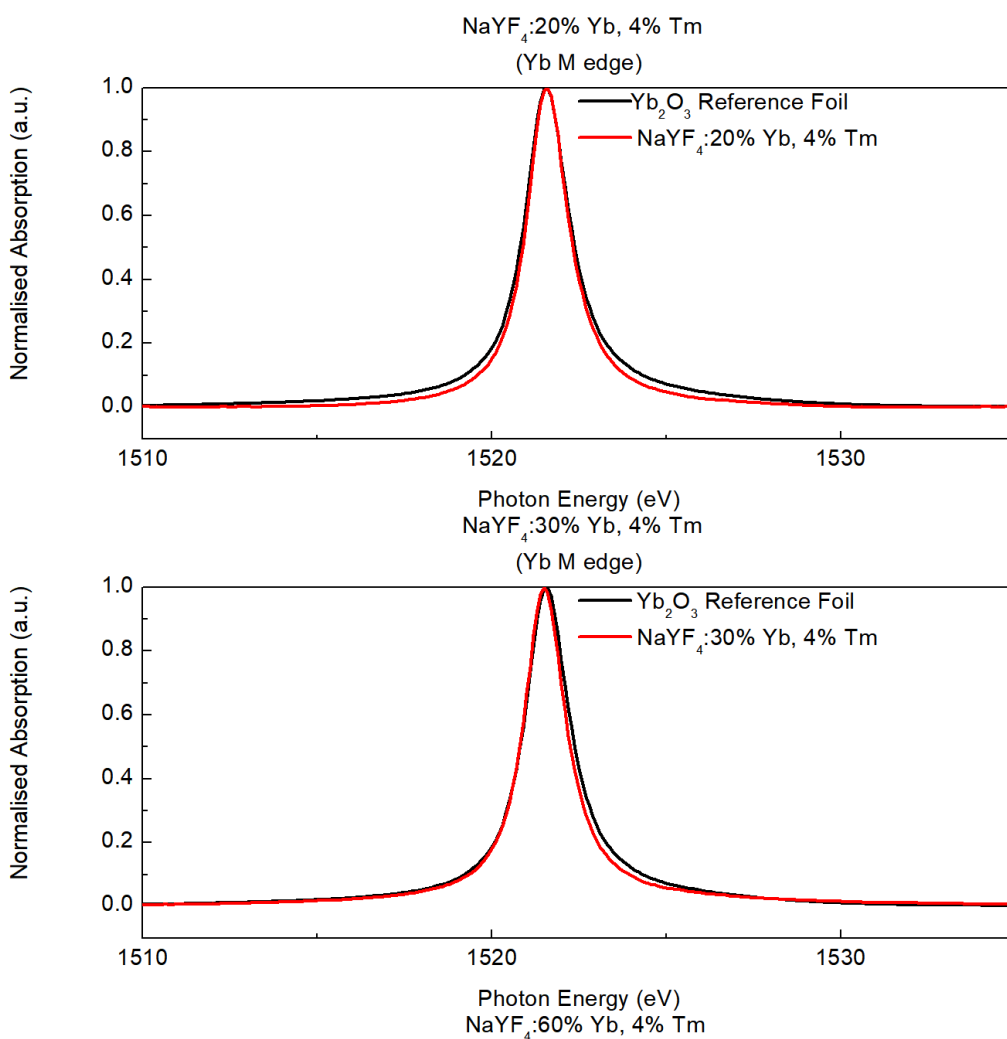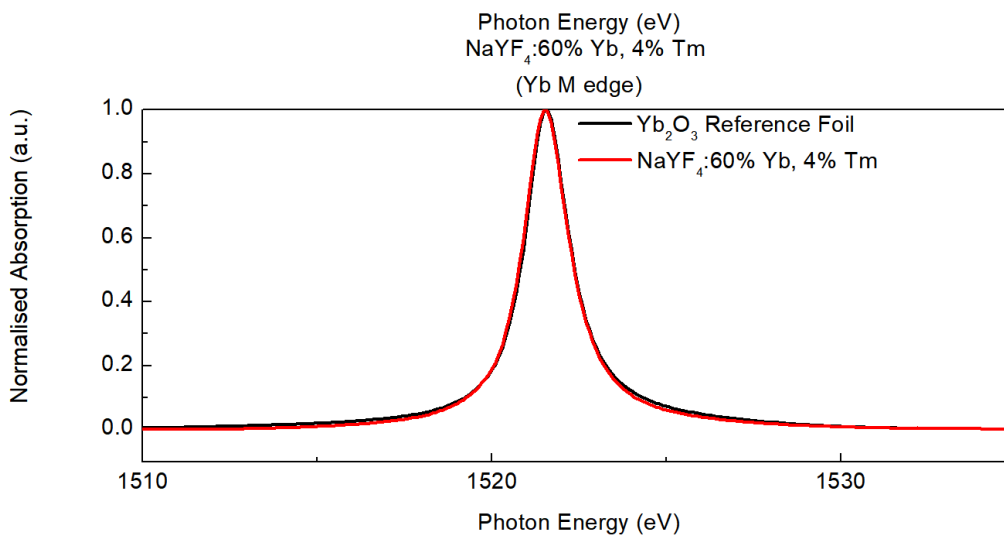
**Figure 4.7** Normalised Yb M-edge TEY NEXAFS spectra of three UCNPs samples superimposed with respective $Yb_2O_3$ reference foil.

## 4.2.4 Lanthanide Distribution

The distribution of $Y^{3+}$ and $Yb^{3+}$ within the UCNPs was next characterised further using EDS mapping. The images in Figure 4.8, show the TEM images, the $Y^{3+}$ (blue) and $Yb^{3+}$ (red) elemental map images and the merged images of the three. Figure 4.8 (a,b) are the elemental maps of 31.1 nm and 43.0 nm $NaYF_4$: 20% $Yb^{3+}$, 4% $Tm^{3+}$ UCNPs. The images of $Y^{3+}$ and $Yb^{3+}$ appear to show uniform distribution, however, when aligned together with the TEM images, the UCNPs in the merged images display a dark purple almost red colour in the centre and light purple even blue at the surface. These merged images suggest that more $Yb^{3+}$ exists in the centre and less towards the surface of the UCNP. The $Y^{3+}$ elemental map of a single $NaYF_4$: 45% $Yb^{3+}$, 4% $Tm^{3+}$ UCNP shown in Figure 4.8 (c) has an absence of blue in the centre while the $Yb^{3+}$ elemental map shows a faint red colour around the surface and the merged image is purple in the centre which fades to blue at the surface. In Figure 4.8 (d), a more intense purple colour, even red colour, is visible in the merged image for these 60% $Yb^{3+}$ doped UCNPs. Unfortunately, smaller UCNPs were unable to be mapped due to damage after long periods of electron beam irradiation exposure.

To quantitatively characterise the dopant distribution via EDS, line scan analysis was performed on the EDS data. Figure 4.9 shows this analysis with the distributions of both $Yb^{3+}$ and $Y^{3+}$ within UCNPs being non-uniform. In both images $Yb^{3+}$ reaches a maximum at the centre of the UCNP and decreases to the surface. This $Yb^{3+}$ distribution tendency within the $NaYF_4$ is the same for all the UCNPs regardless of size or sensitizer concentration. In Figure 4.9 (a), one individual 43.0 nm 20% $Yb^{3+}$ UCNP is line scanned. The $Yb^{3+}$ concentration from the left edge of the UCNP starts at 14.25% and gradually reaches 24.35% at the centre before decreasing back to 15.5% when reaching the right edge of the UCNP. Inversely, the $Y^{3+}$ concentration decreases from the surface to the centre along the UCNP. In Figure 4.9 (b), three aligned 60% $Yb^{3+}$ doped UCNPs were scanned and the periodic concentration variation in $Yb^{3+}$ and $Y^{3+}$ across each individual UCNP is consistent having the same trend of distribution as the 20% $Yb^{3+}$ doped UCNPs. The highest concentration of $Yb^{3+}$ found at the UCNP centre is 56% - 58%.

**(a)**



(a)                                                                                          (b)

**(b)**



(b)
(a)

**(c)**

(b)



(d)
(c)

(d)

56

**(b)**

**(d)**
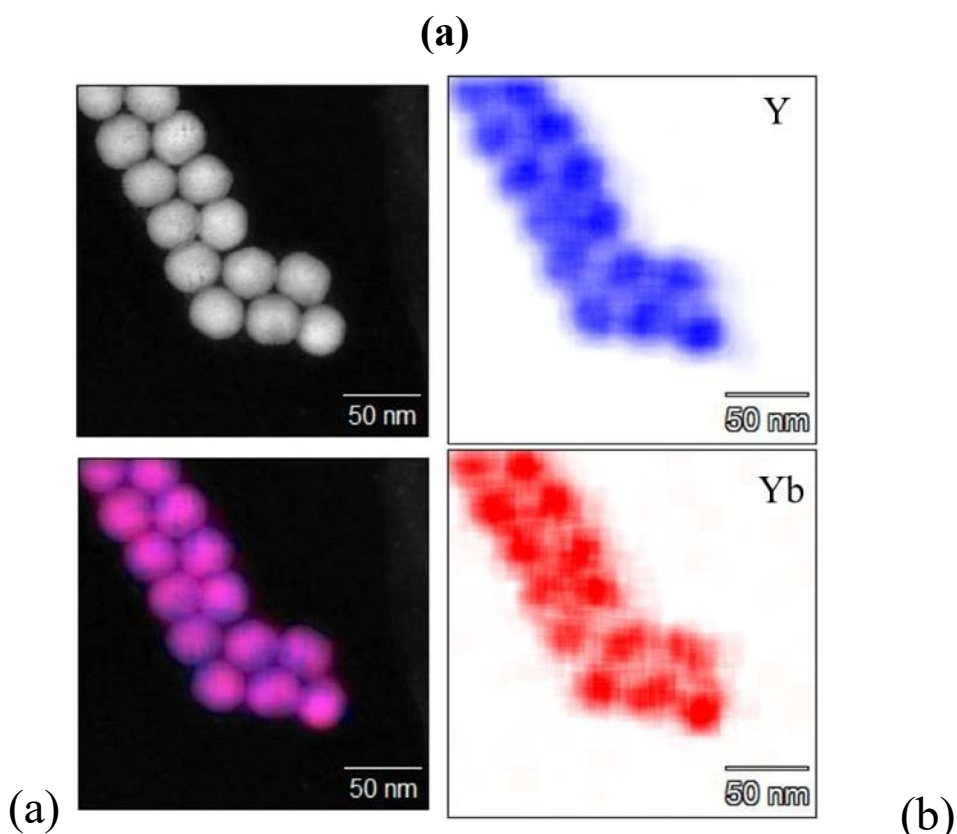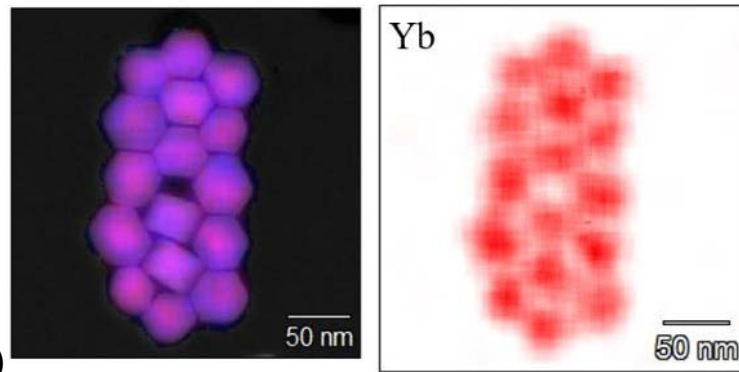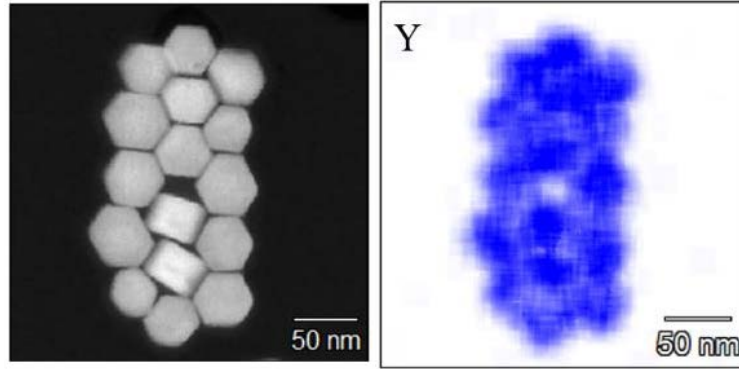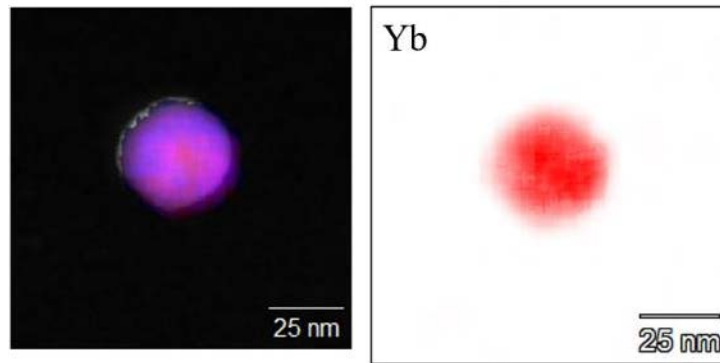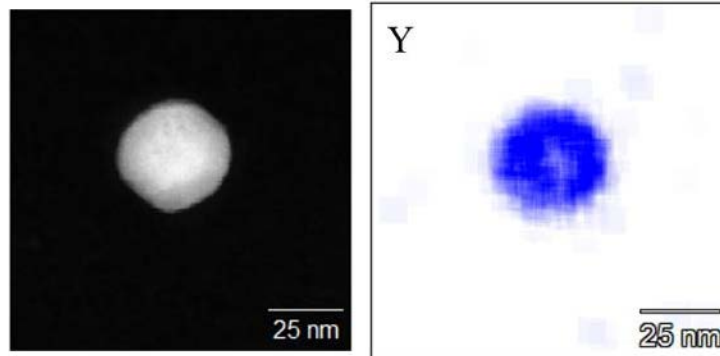
**(d)**
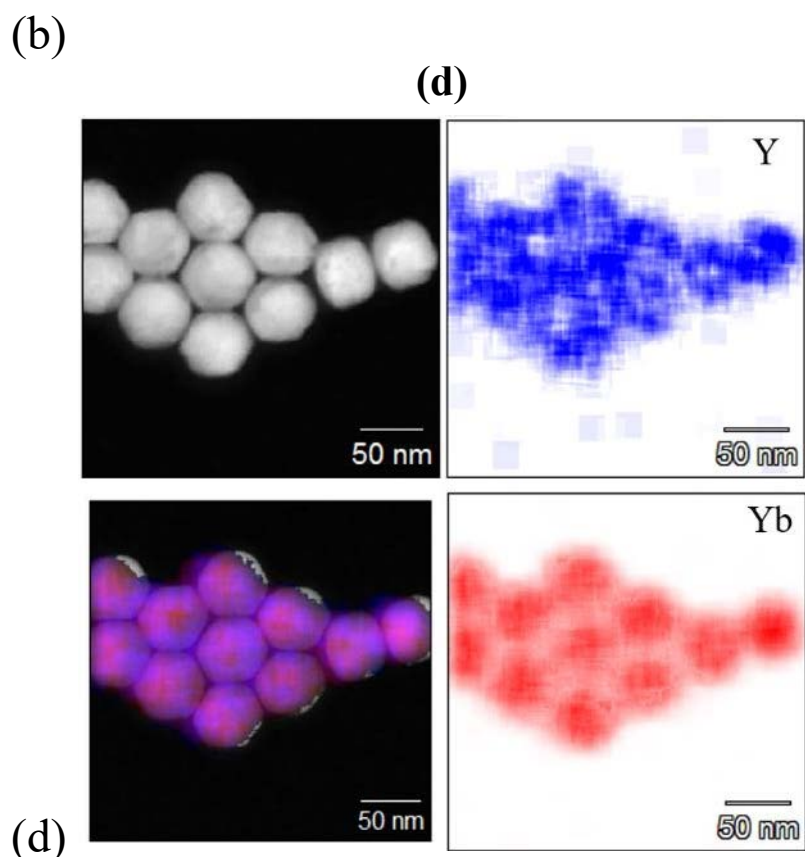
**Figure 4.8** Elemental maps of 31.1 nm NaYF$_4$: 20% Yb$^{3+}$, 4% Tm$^{3+}$ UCNPs (a), 43.0 nm NaYF$_4$: 20% Yb$^{3+}$, 4% Tm$^{3+}$ UCNPs (b), 36.7 nm NaYF$_4$: 45% Yb$^{3+}$, 4% Tm$^{3+}$ UCNPs (c) and 51.3 nm NaYF$_4$: 60% Yb$^{3+}$, 4% Tm$^{3+}$ UCNPs (d).

**(a)**

**(b)**
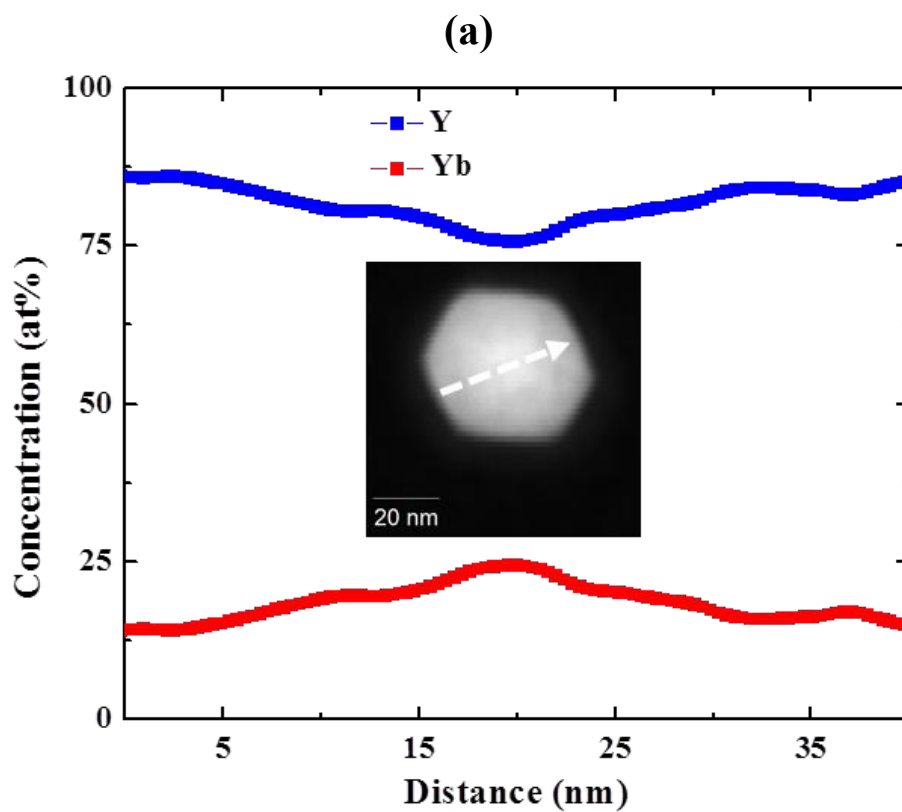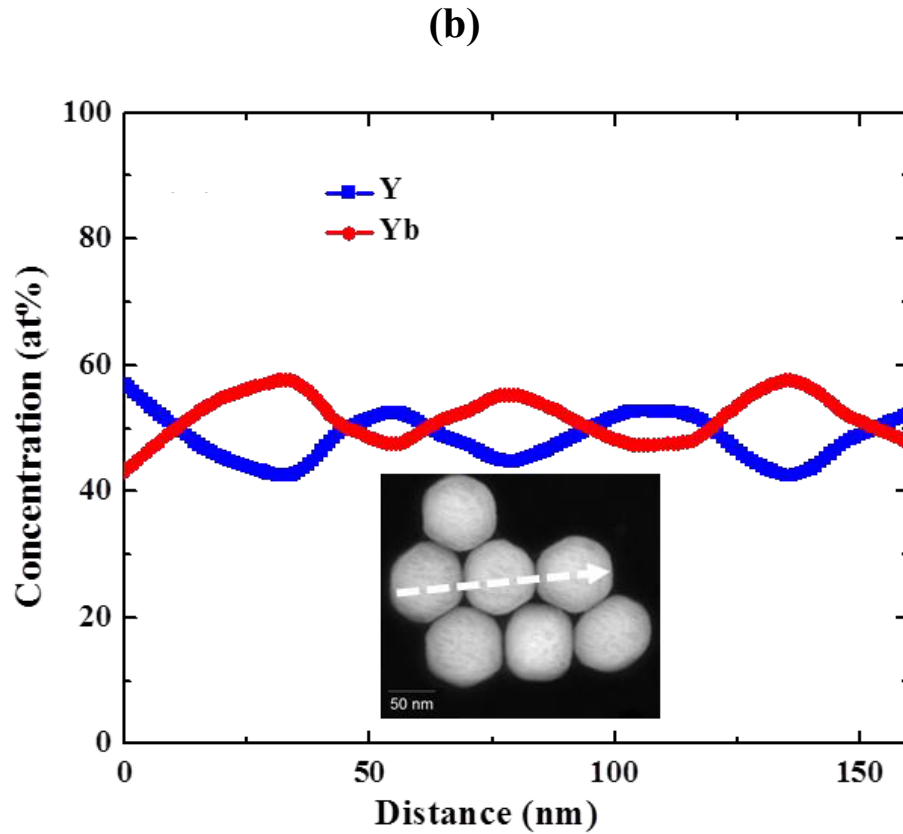


**Figure 4.9** EDS line scans with inset of TEM image of 43.0 nm NaYF$_4$: 20% Yb$^{3+}$, 4% Tm$^{3+}$ UCNPs (a) and 51.3 nm NaYF$_4$: 60% Yb$^{3+}$, 4% Tm$^{3+}$ UCNPs (b).

## 4.2.5 Lanthanide Concentration

The concentration of Yb$^{3+}$, Tm$^{3+}$ and Y$^{3+}$ within the NaYF$_4$ UCNPs was characterised using ICP-MS. ICP-MS allows for an absolute quantitative characterisation of total composition to confirm the UCNPs contained the desired dopant concentrations. Table 4.1 lists the measured compositions of Y$^{3+}$, Yb$^{3+}$ and Tm$^{3+}$ by ICP-MS which are within the designed composition percentage range for all UCNP samples.

**Table 4.1** ICP-MS elemental composition of NaYF$_4$ UCNPs doped with Yb$^{3+}$ and Tm$^{3+}$.

| Size (nm) | Designed Composition | | | Measured Composition | | |
|---|---|---|---|---|---|---|
| | Y$^{3+}$ | Yb$^{3+}$ | Tm$^{3+}$ | Y$^{3+}$ | Yb$^{3+}$ | Tm$^{3+}$ |
| 13.0 | 76% | 20% | 4% | 76.03% | 20.21% | 3.75% |
| 26.2 | | | | 75.52% | 20.94% | 3.30% |
| 31.1 | | | | 77.87% | 18.23% | 3.54% |
| 36.6 | | | | 78.88% | 17.42% | 3.90% |
| 43.0 | | | | 79.62% | 17.05% | 3.70% |
| 27.4 | 66% | 30% | | 68.89% | 27.60% | 3.51% |
| 35.9 | 51% | 45% | | 53.05% | 43.22% | 3.74% |
| 51.3 | 36% | 60% | | 33.48% | 63.24% | 3.28% |

## 4.2.6     Single Particle Upconversion Emission

Single particle optical emission intensities of the UCNP samples were compared and it was determined that the emission intensities of the UCNPs increased with size. However, when normalised to the activator number within each UCNP this trend was inverted as shown in Figure 4.10. Based on the findings of the depth profiling investigation this result can be explained by the lanthanide distribution which produces a Yb$^{3+}$ rich core and Yb$^{3+}$ depleted shell, this structure minimises the surface quenching effects by reducing energy loss from the interactions between sensitizer Yb$^{3+}$ ions and surface defects, impurities, ligands and solvents [146]. In addition to the improved internal crystal quality this distribution especially benefits the smaller UCNPs that have a high surface-area-to-volume ratio explaining why the 13.0 nm UCNPs exhibit a higher upconversion emission efficiency than the larger UCNPs.
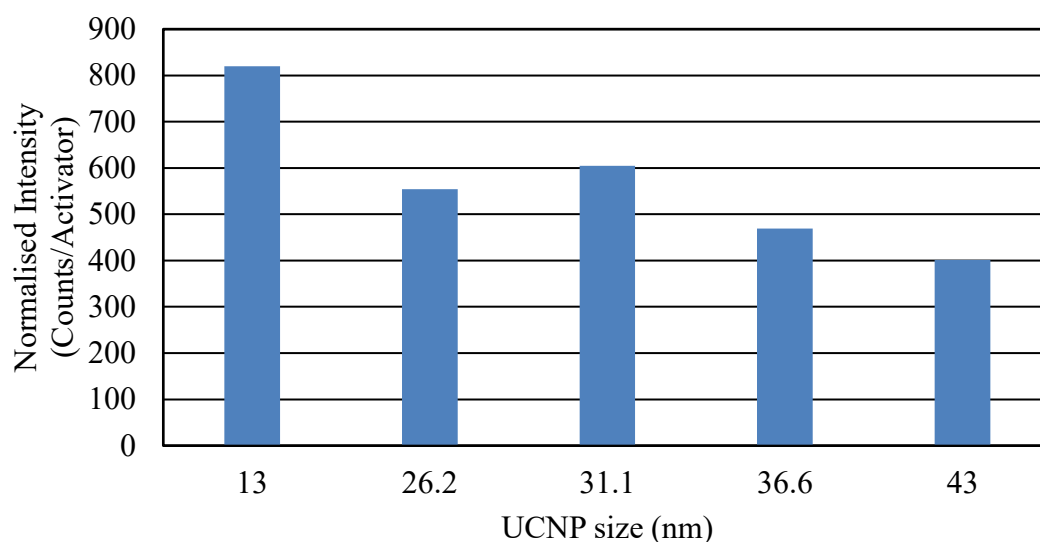
**Figure 4.10** Normalised single particle upconversion intensity to activator number in 20% $Yb^{3+}$ doped UCNPs of sizes 13 nm, 26.2 nm, 31.1 nm, 36.6 nm and 43 nm.

## 4.2.7    Depth Profiling $Tb^{3+}$ in 4% $Tm^{3+}$ $NaYF_4$ UCNPs

An additional batch of three $NaYF_4$ UCNPs doped with 4% $Tm^{3+}$ and 20%, 30% and 45% $Tb^{3+}$ respectively were XPS depth profiled in the same manner to determine if a concentration gradient for $Tb^{3+}$ exists. The three UCNP samples shown in Figure 4.11 (a-c) are uniform with an average size of 8.9 nm, 12.7 nm and 16.4 nm respectively. It was expected again that due to minor differences in ionic size and electronic polarity between the $Tb^{3+}$ and $Y^{3+}$ ions there should be a concentration gradient of $Tb^{3+}$ existing from the surface to core. The summarised result of the depth profiling XPS in Figure 4.11 (d) confirms such a gradient exists in all three UCNP samples. The smaller UCNPs with a higher doping concentration exhibit the steepest $Tb^{3+}/Y^{3+}$ concentration gradient. This result indicates that $Tb^{3+}$ distributes in the same manner as $Yb^{3+}$ with a higher concentration existing at the core of the UCNP that gradually decreases towards the surface. This investigation confirms that depth profiling XPS can be used to characterise the concentration gradient of other lanthanide dopants within UCNPs.
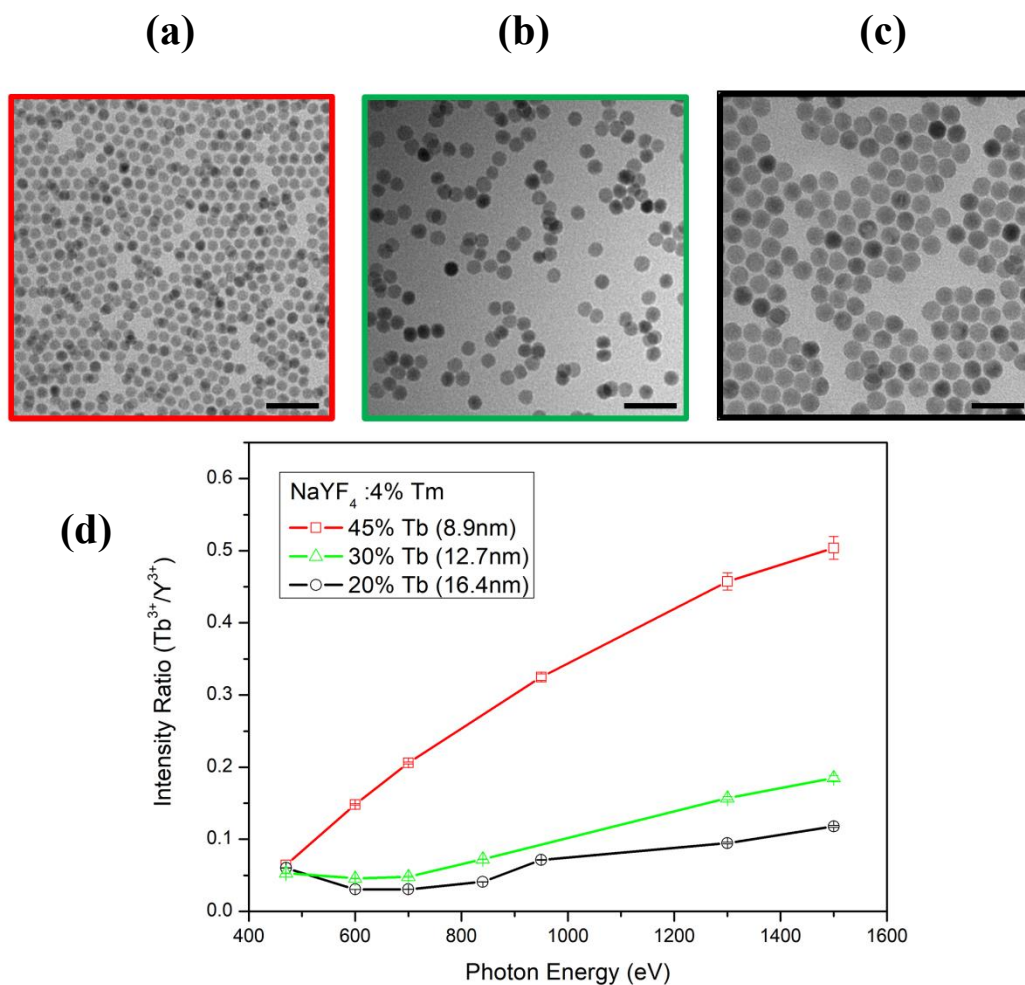
**Figure 4.11** TEM images of the three NaYF$_4$ UCNPs doped with 4% Tm$^{3+}$ and 20% (black), 30% (green) and 45% Tb$^{3+}$ respectively (red) showing uniform size and morphology (black scale bar in each image is 50 nm) (a-c). Increasing Tb$^{3+}$/Y$^{3+}$ atomic ratio within UCNPs with increasing X-ray photon energy (d).

# 4.3      Summary

The $Yb^{3+}/Y^{3+}$ ratio obtained from the lanthanide distribution investigation by XPS supports the hypothesis proposed for UCNPs of different sizes and varied $Yb^{3+}$ doping concentrations. The $Yb^{3+}$ ions distribution within the host UCNP is not uniform and the heterogeneous distribution trend is repeated for all single UCNPs studied regardless of their size or the $Yb^{3+}$ concentration.

The elemental mapping and the line scan EDS analysis are consistent with the depth resolved XPS characterisation. These two methods provide a semiquantitative measurement of the concentration ratio between $Yb^{3+}$ and $Y^{3+}$ which is also reinforced by NEXAFS, ICP-MS and single particle emission analysis. Additional depth profiling of $Tb^{3+}$ doped UCNPs confirms the general ability of the method to determine the concentration gradient of lanthanide dopants within UCNPs.

Compared to the synchrotron-based depth resolved XPS, EDS possesses general accessibility, individual UCNP analysis and short analysis time but is less surface sensitive with samples suffering instability from the intense electron beam. The highly concentrated distribution of sensitizer $Yb^{3+}$ ions within the core of the host $NaYF_4$ UCNPs proven with these characterisation methods is directly related to the upconversion luminescent properties and is advantageous for optical enhancement methods.

# Chapter 5

# Enhanced Emission of Core-Shell NaYF$_4$ UCNPs by Plasmonic Coupling

## 5.1    Introduction

The findings of the lanthanide distribution are taken into account in this chapter towards a method that reliably produces surface plasmon enhanced core-shell (CS) UCNPs. In this method a NaYF$_4$ shell layer with a thickness between 5 nm - 15 nm is grown around the optical active UCNP for use as a tuneable spacer to control the distance between the UCNP and the plasmonic gold (Au) nanoparticles. The Au nanoparticles are formed into uniform spherical nanoparticles atop the CS UCNPs by sputtering and thermal annealing dewetting, the process of a thin film disaggregating into discrete particles via the minimisation of surface energy at high temperature [155]. The shape and size of dewetted Au nanoparticles can be precisely controlled on a large-scale by simply varying the film thickness, annealing temperature and annealing time so that their LSPR can be tuned to match the emission wavelength of Er$^{3+}$ activators in the NaYF$_4$ CS UCNPs [156-158]. The high temperature annealing required for dewetting the Au onto the surface of the CS UCNPs should also promote the diffusion of Ln$^{3+}$ dopants within the UCNP reducing internal defects which can lead to an increased quantum efficiency [82].

The design as shown in Figure 5.1, consisting of an optically active NaYF$_4$: Yb$^{3+}$, Er$^{3+}$ UCNP core, an optically inert shell spacer grown from the same NaYF$_4$ crystal as the core and plasmonic satellite Au nanoparticles decorated on the shell, is achieved via

CS UCNP synthesis and dewetting allowing a large-scale assembly of Au nanoparticles onto singularly dispersed CS UCNPs.

This design overcomes the limitation of previous designs by using an undoped inert NaYF$_4$ shell. The nanometre thickness of this NaYF$_4$ shell is highly controllable by adjusting the concentration and amount of shell precursor added during epitaxial growth [71, 159, 160]. The inert shell of the host NaYF$_4$ crystal is employed here as both a surface passivation layer to reduce surface defects enhancing luminescence [80] and functionality as the spacer in the plasmonic coupling design.
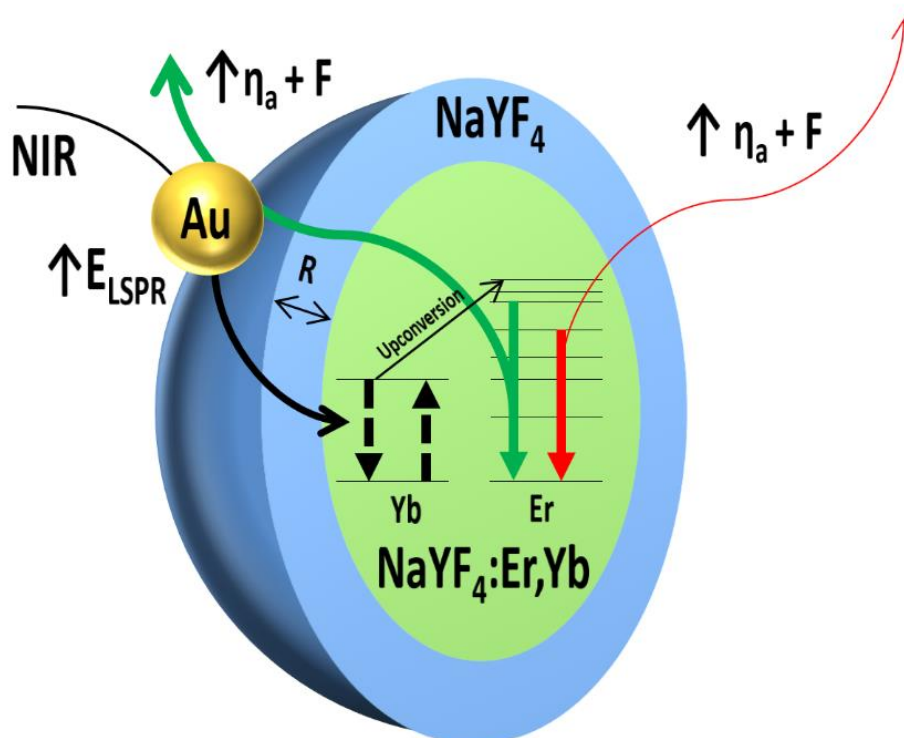


**Figure 5.1** The design for the gold decorated upconversion nanoparticles produced by integrating the methods of core shell UCNP synthesis, thermal annealing and gold dewetting.

# 5.2 Plasmonic Enhancement

## 5.2.1 Morphology

Figure 5.2 (a) shows the TEM image of the well dispersed core UCNPs used for this study that have a highly uniform morphology with an average diameter of 25 nm. Figure 5.2 (b) and Figure 5.3 (a,c) show the core shell (CS) UCNPs which are the core UCNPs after the growth of an inert $NaYF_4$ shell coating of thicknesses between 5 nm, 10 nm and 15 nm respectively. The variation in the 35 nm CS UCNPs resulting in an ellipsoid shape is due to the longitudinal preference of the epitaxial shell growth which is especially pronounced when thin shell coatings are grown. The 35 nm CS UCNPs are within 2 nm of being spherical, less than the incremental 5 nm step in the varied shell thickness and hence should not significantly affect the plasmonic enhancement.

The uniformly separated dewetted Au nanoparticles shown in Figure 5.3 (b) have an average diameter of 15 nm. The Au-CS UCNPs in Figure 5.2 (c) shows the typical morphology of the dewetted Au nanoparticles on the surface of CS UCNPs which also have an average diameter of 15 nm. After dewetting the CS UCNPs appear to have no changes in morphology while the Au nanoparticles have directly dewetted onto the surface of the CS UCNPs producing the desired structure. As Figure 5.3 (d) highlights this method is able produce single well dispersed Au-CS UCNPs. This level of dispersion is suitable to be used directly for single nanoparticle upconversion luminescence measurement to determine the effect the Au nanoparticles have on the emission performance of the CS UCNPs.

XPS survey spectra of the 55 nm CS UCNPs and the 55 nm Au-CS UCNPs after dewetting in Figure 5.2 (d) confirms the composition of the samples. The presence of Na, Y, F and Yb in both spectra can be attributed to the CS UCNPs while the C and O peaks result from attached adventitious carbon from the atmosphere [161]. The presence of the Au peak only in the Au-CS UCNPs spectra confirms the attached nanoparticles are Au. The samples for this XPS measurement were prepared on a Si substrate with a high surface coverage. The absence of the Si peaks in both spectra indicates the X-ray photon energy used had a sampling depth above the silicon

substrate. As a result, it can be concluded that the entire Au peak in the spectrum is resultant from the dewetted Au nanoparticles on the surface of the CS UCNPs rather than Au dewetted on the surface of the substrate.

**(a)**
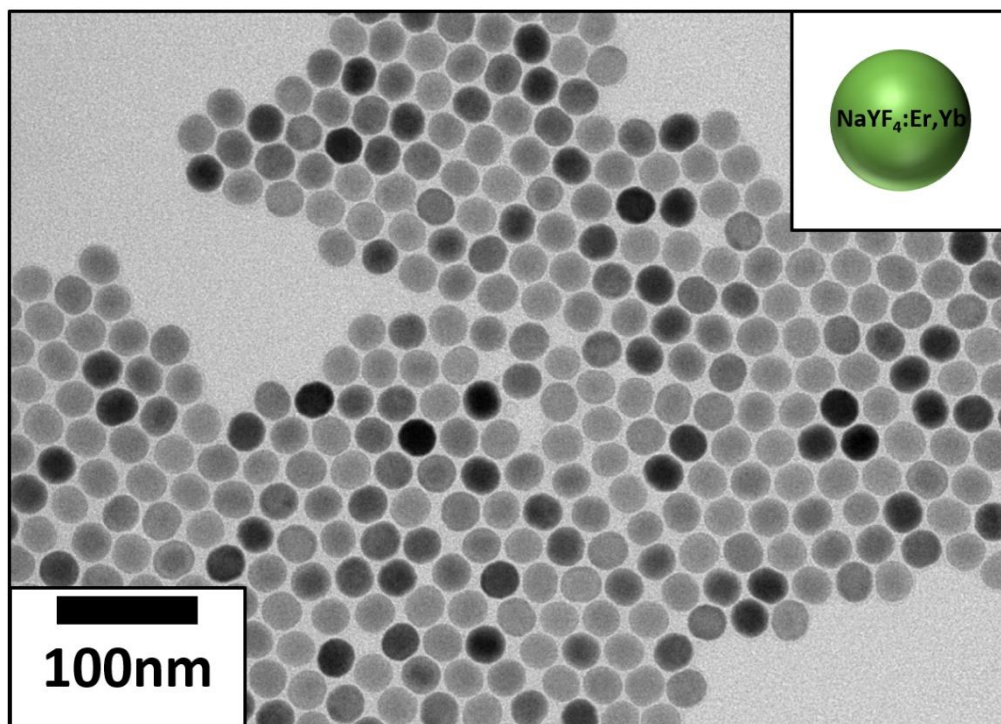


**(b)**
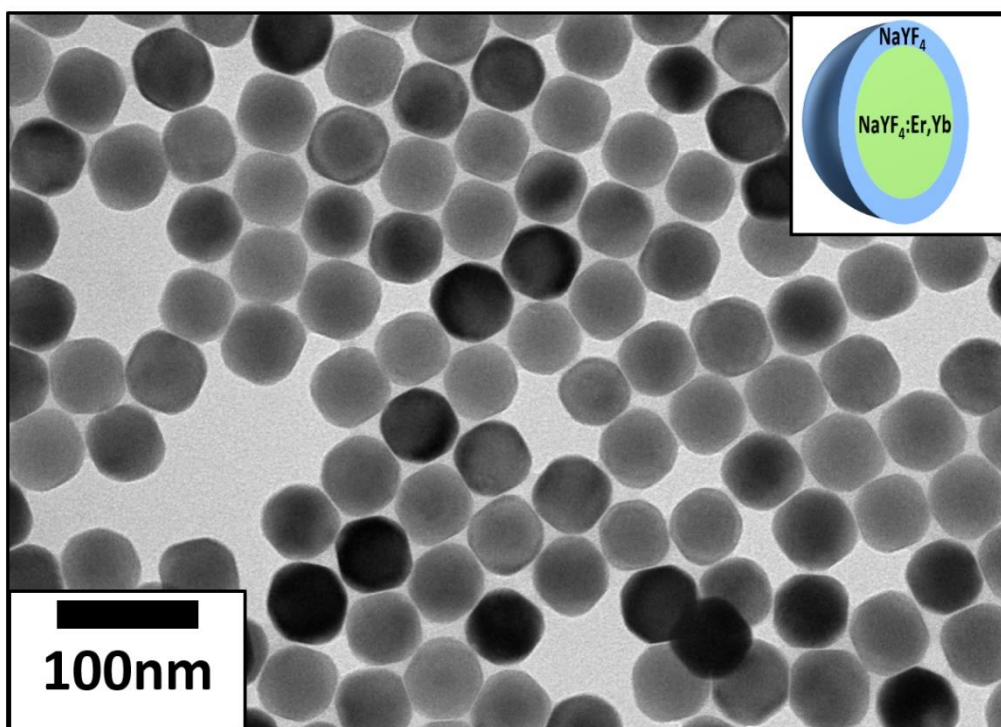
**(c)**
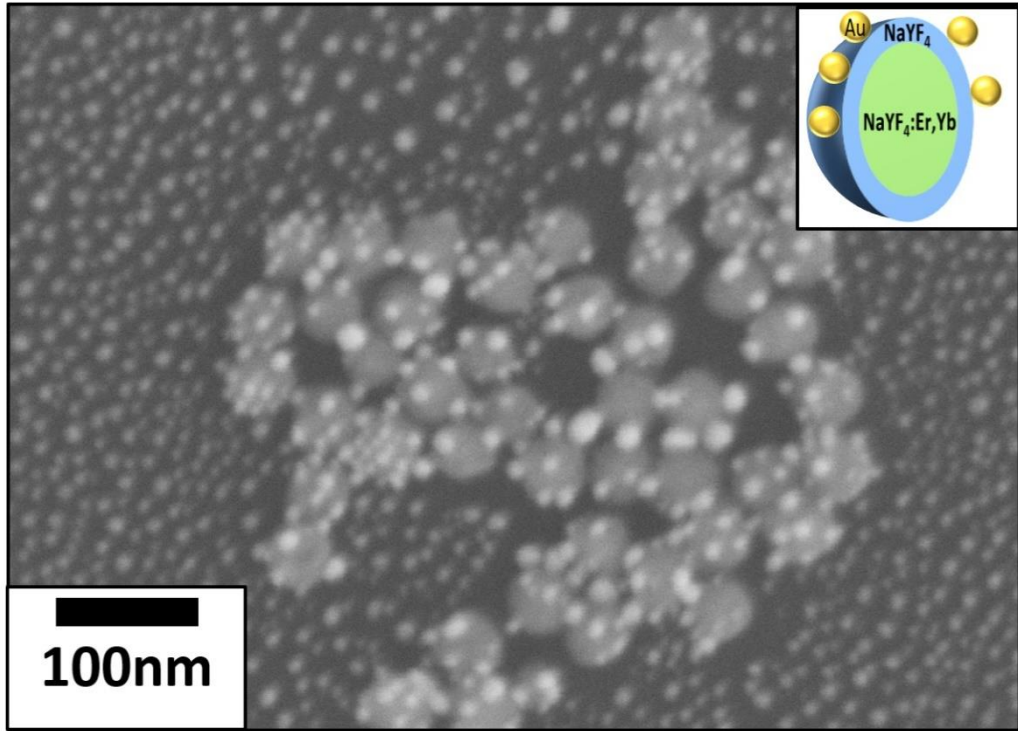


**(d)**
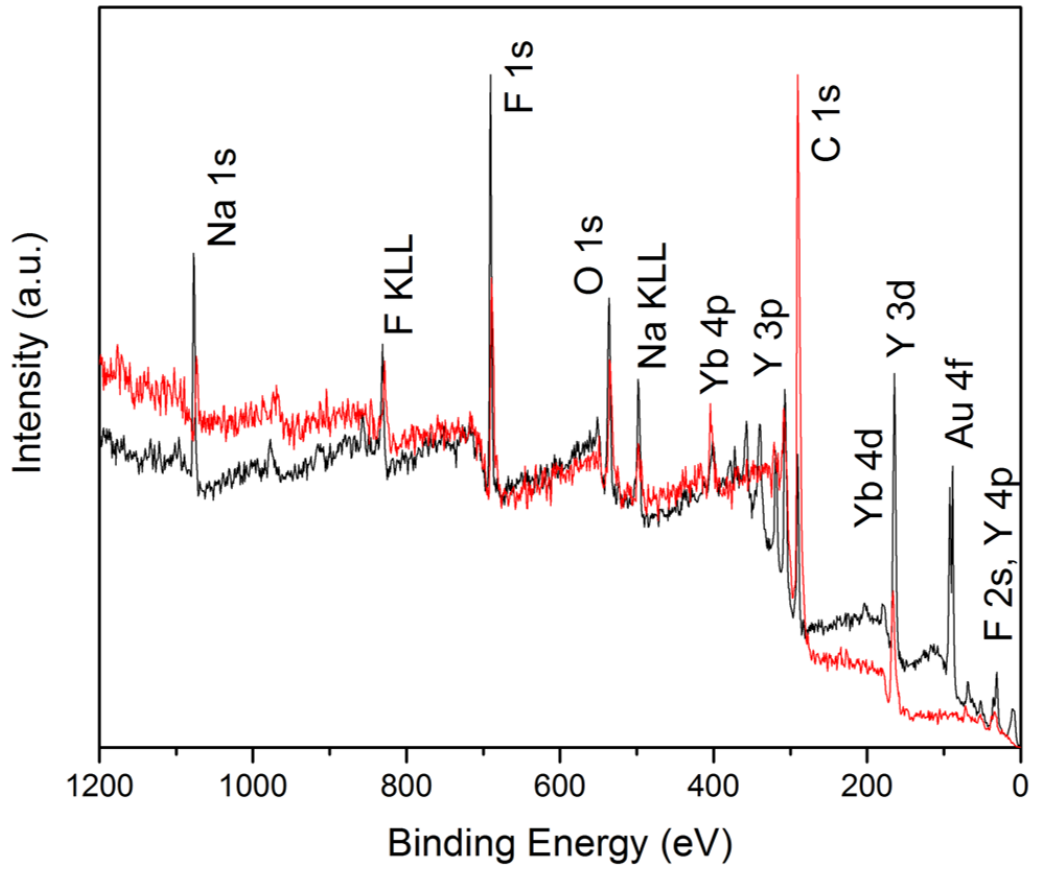
**Figure 5.2** TEM image of 25 nm diameter core β-NaYF$_4$:20%Yb$^{3+}$, 2%Er$^{3+}$ UCNPs (a), TEM image of 55 nm diameter β-NaYF$_4$:20%Yb$^{3+}$, 2%Er$^{3+}$/NaYF$_4$ CS UCNPs (b), SEM image of assembled 55 nm diameter β-NaYF$_4$:20%Yb$^{3+}$, 2%Er$^{3+}$/NaYF$_4$ Au-CS UCNPs after annealing at 400 °C for 1 hour (c) and XPS survey spectra of 55 nm diameter CS UCNPs (red) and the assembled 55 nm diameter Au-CS UCNPs after annealing (black) (d).

**(a)**

**(b)**



100nm

**(c)**



100nm
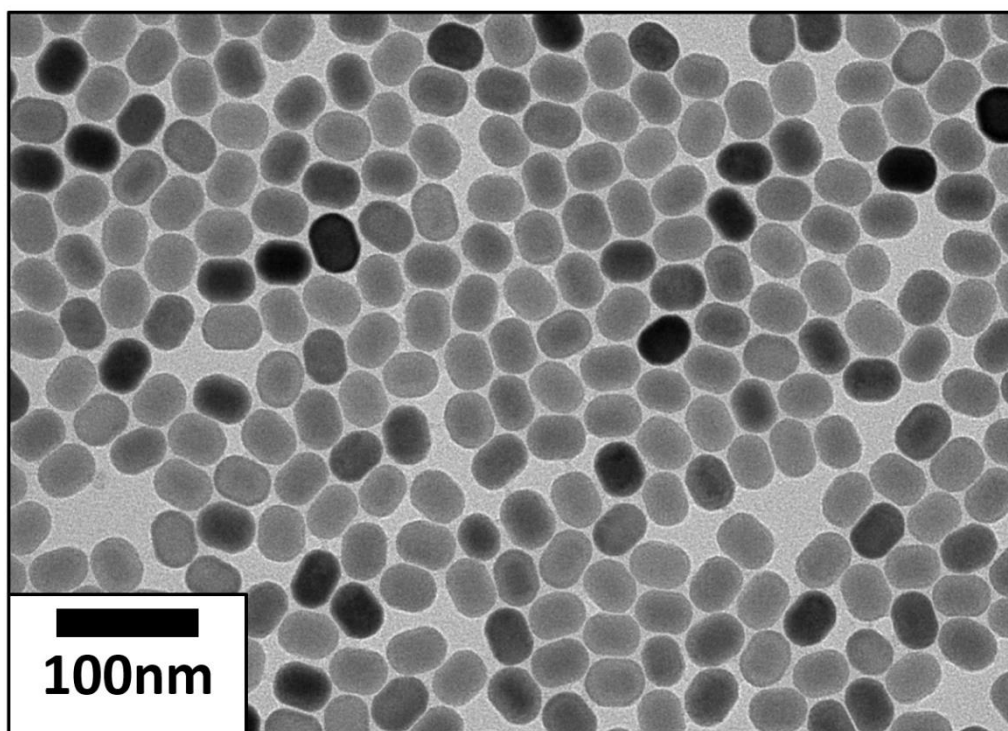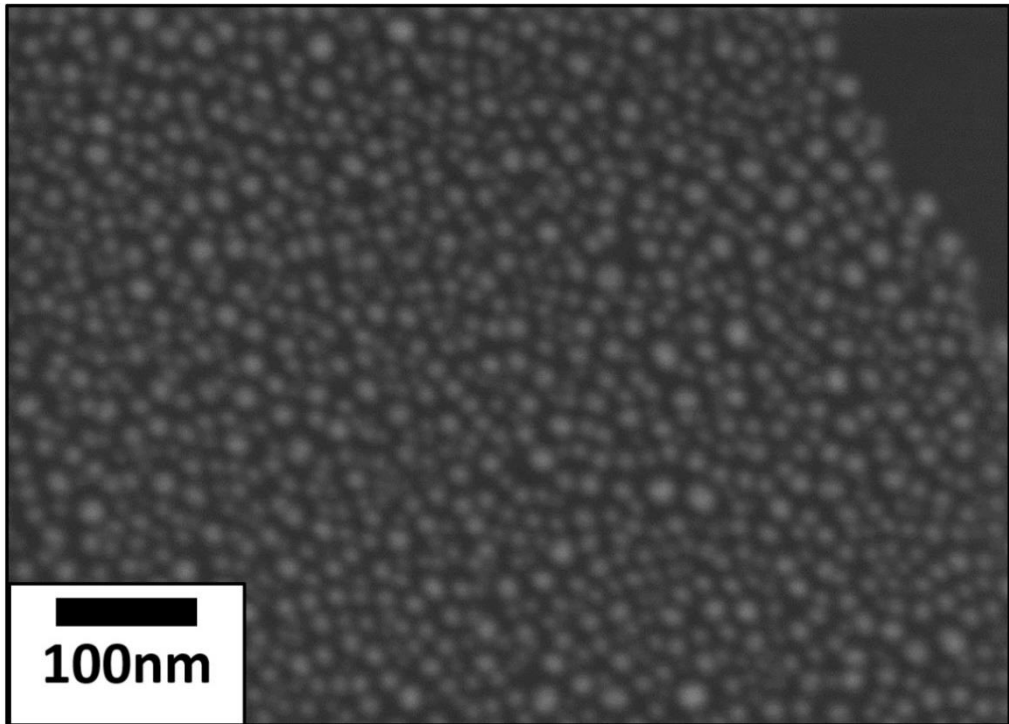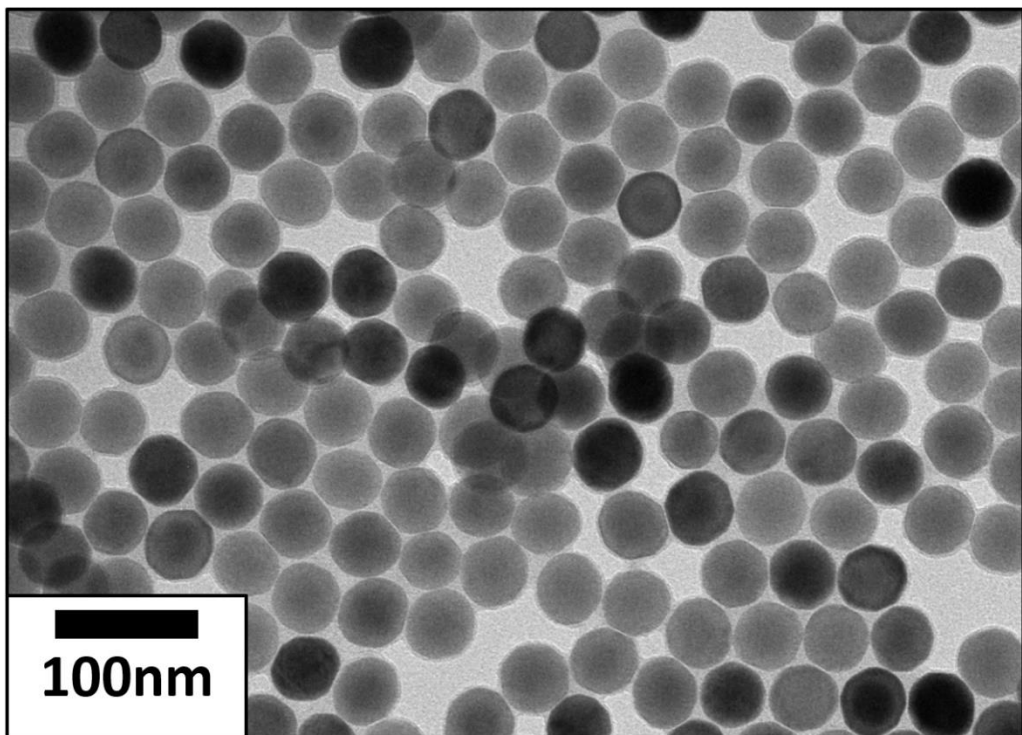
**(d)**
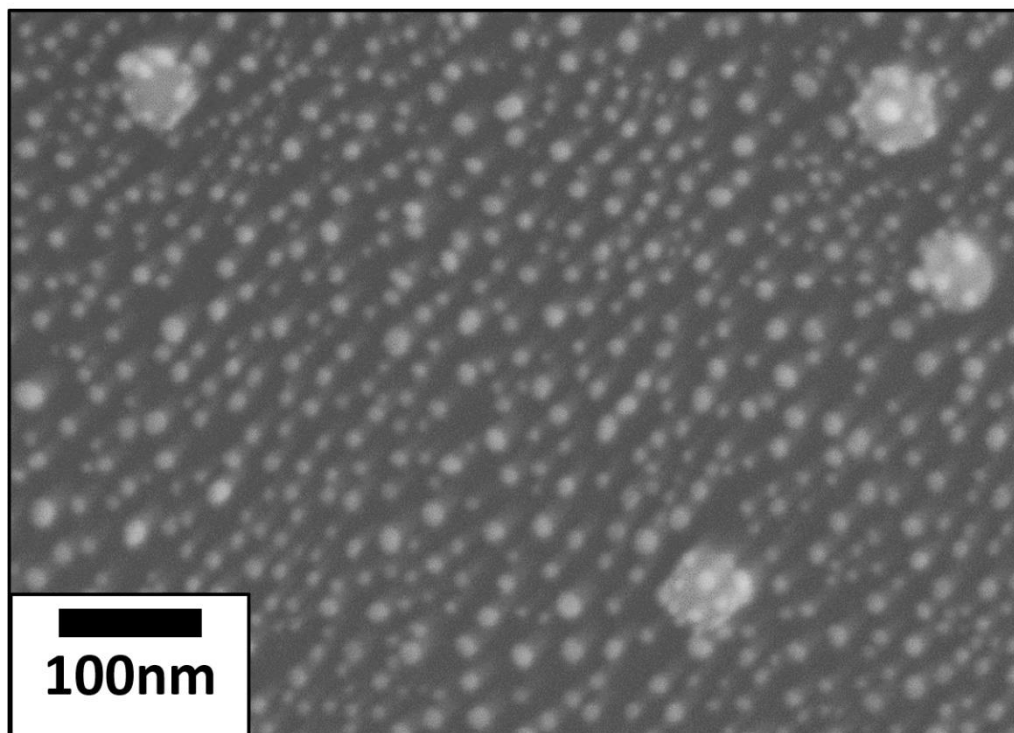


**Figure 5.3** TEM image of 35 nm diameter β-NaYF$_4$:20%Yb$^{3+}$,2%Er$^{3+}$/NaYF$_4$ CS UCNPs (a), SEM image of 15 nm dewetted Au nanoparticles (b), TEM image of 45 nm diameter β-NaYF$_4$:20%Yb$^{3+}$,2%Er$^{3+}$/NaYF$_4$ CS UCNPs (c) and SEM image of 55 nm diameter β-NaYF$_4$:20%Yb$^{3+}$,2%Er$^{3+}$/NaYF$_4$ Au-CS UCNPs (d).

## 5.2.2 Crystal Structure

The dewetting treatment at 400 °C for 1 hour is not only ideal for effectively disaggregating the Au film into discrete nanoparticles of specific size onto the CS UCNP surface but it is also optimum for the CS UCNPs being below the threshold temperature that would result in their aggregation and phase change [81]. XRD characterisation was performed to determine the effect this annealing has on the crystal phase structure of the UCNPs. In Figure 5.4 the CS UCNPs XRD spectra before and after annealing at 400 °C for 1 hour shows that the CS UCNPs retain their β-phase after annealing.
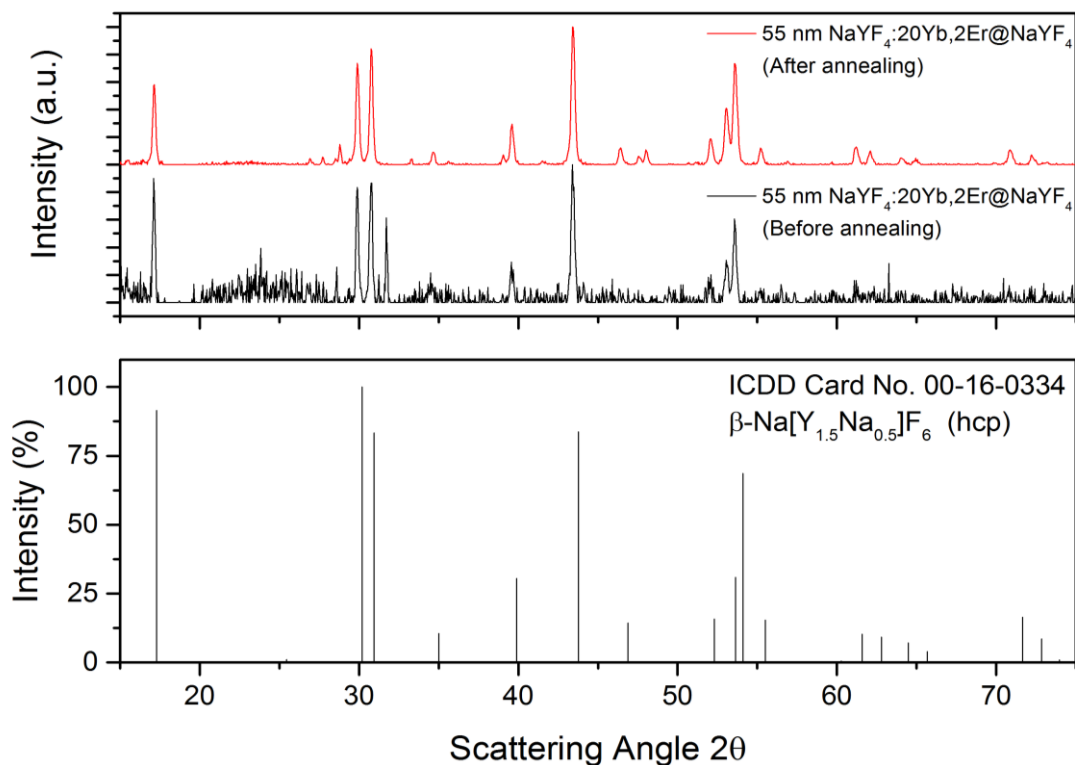
**Figure 5.4** XRD of CS UCNPs with 15 nm shell before and after annealing at 400 °C for 1 hour.

## 5.2.3 Dopant Diffusion

To investigate if the annealing had affected the distribution of the $Er^{3+}$ and $Yb^{3+}$ dopants within the CS UCNPs, near edge X-ray absorption fine structure (NEXAFS) was conducted in partial electron yield (PEY) and total fluorescent yield (TFY).

Figure 5.5 (a,c) are the NEXAFS spectra in TFY mode which probes the entire 5 nm shell CS UCNP volume. The TFY intensity for both $Er^{3+}$ in Figure 5.5 (a) and $Yb^{3+}$ in Figure 5.5 (c) before and after annealing is the same, this indicates that for both samples the surface coverage of UCNPs on the substrate is approximately equal. In PEY mode the sampling depth is only the first few nanometres of the shell volume allowing for any change in the distribution of the dopants to be identified. For both $Er^{3+}$ in Figure 5.5 (b) and $Yb^{3+}$ in Figure 5.5 (d) after annealing there is an increase in the intensity of the PEY spectra. As the TFY spectra determined the surface coverage

was approximately equal the change in intensity of the PEY spectra can be used directly to calculate the relative increase of dopants diffused towards the shell after annealing. This semiquantitative method estimates the increase to be a factor of 3.8 and 4.4 for $Er^{3+}$ and $Yb^{3+}$ respectively. This result indicates that both dopants have diffused further from the core towards the inert shell during the annealing process. The driving force for their diffusion would be the concentration gradient that exists from the core to the inert shell accelerated under the annealing conditions. As expected, the increase in $Yb^{3+}$ is higher than $Er^{3+}$ due to the higher concentration of $Yb^{3+}$ to $Er^{3+}$ (20% to 2%) within the CS UCNP. In Figure 5.6 (a,b) the same technique was applied on 15 nm shell CS UCNPs and 15 nm shell Au-CS UCNPs, revealing a similar relative increase in $Yb^{3+}$ after annealing estimated to be a factor of 1.9.

This diffusion of the lanthanide ions from the core to the inert shell firstly produces a reduced effective distance between the Au nanoparticles on the inert shell and the active core UCNP. Concurrently the enhanced diffusion coefficients of the lanthanide dopants would also facilitate the removal of internal defects increasing the quantum efficiency of the UCNPs as displayed in the simulation of Figure 5.5 (e) [82].

**(a)**
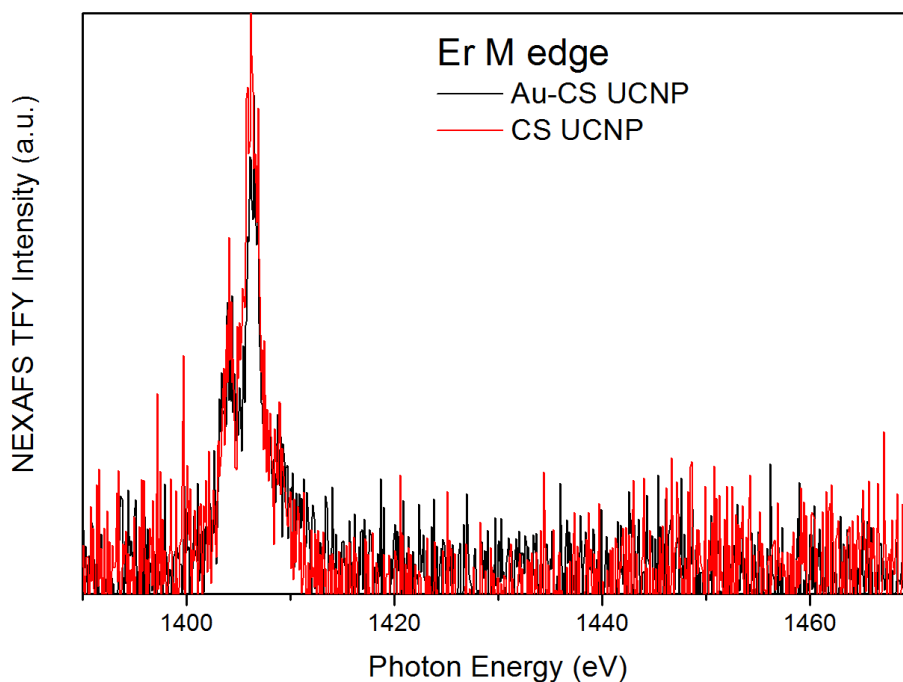
**(b)**
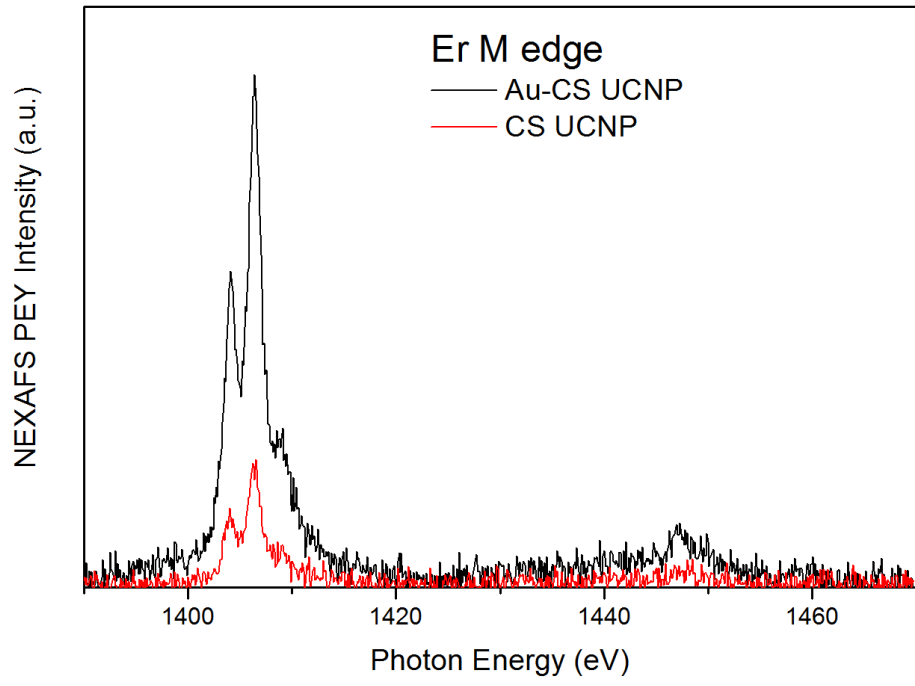


**(c)**
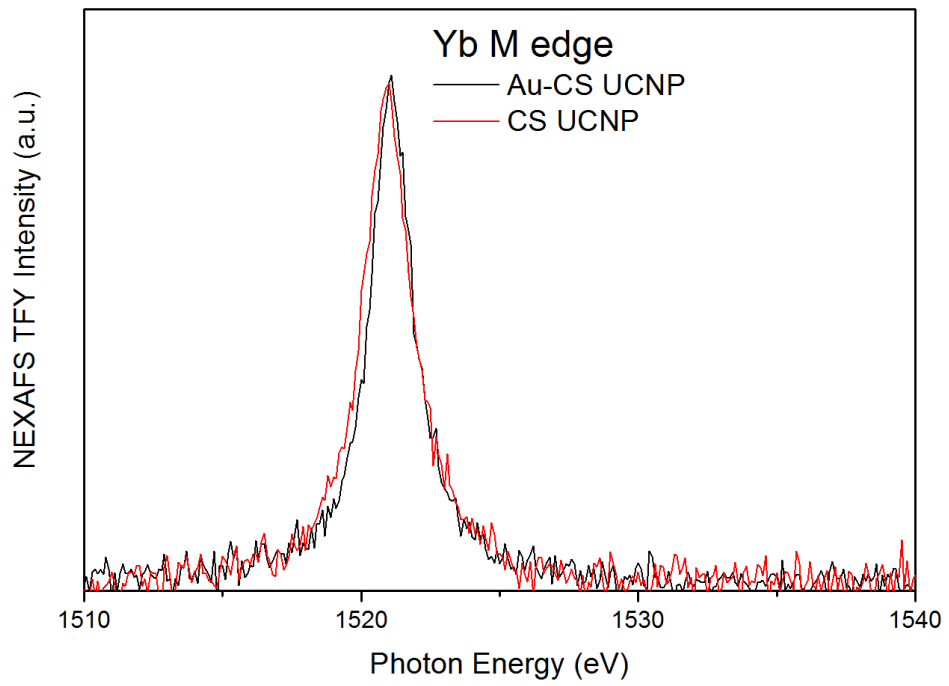
**(d)**
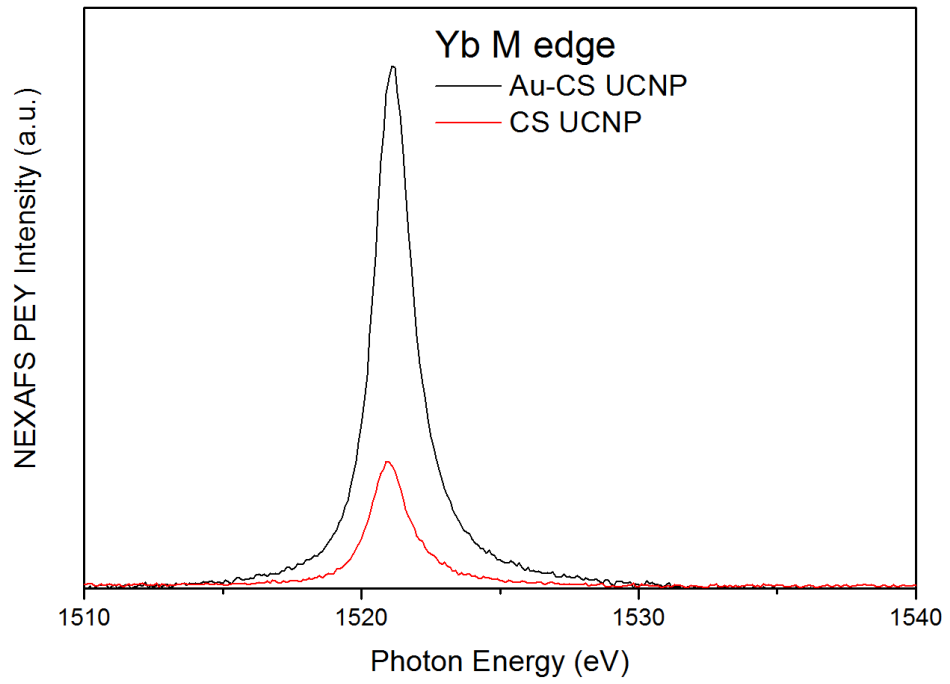


**(e)**
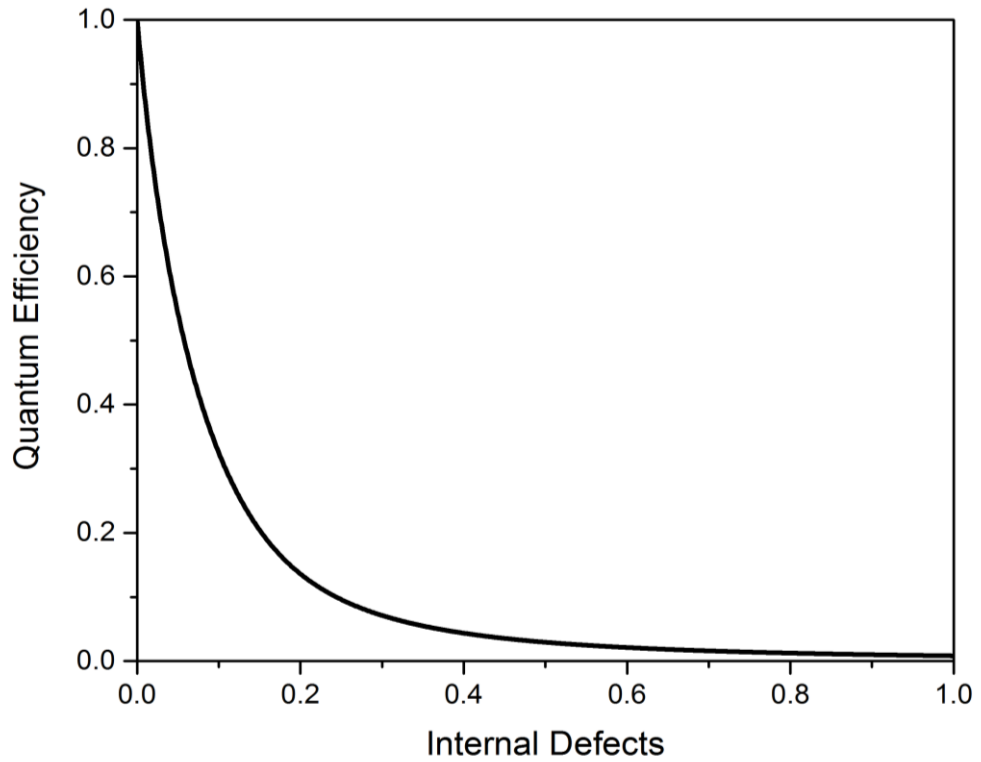


**Figure 5.5** NEXAFS spectra of Er M-edge and Yb M-edge for the CS UCNPs with a 5 nm shell before (CS UCNP) and after annealing with Au (Au-CS UCNP) in TFY

(a,c) and PEY (b,d) modes and the rate equation simulation of quantum efficiency attenuation vs internal defect density (e).
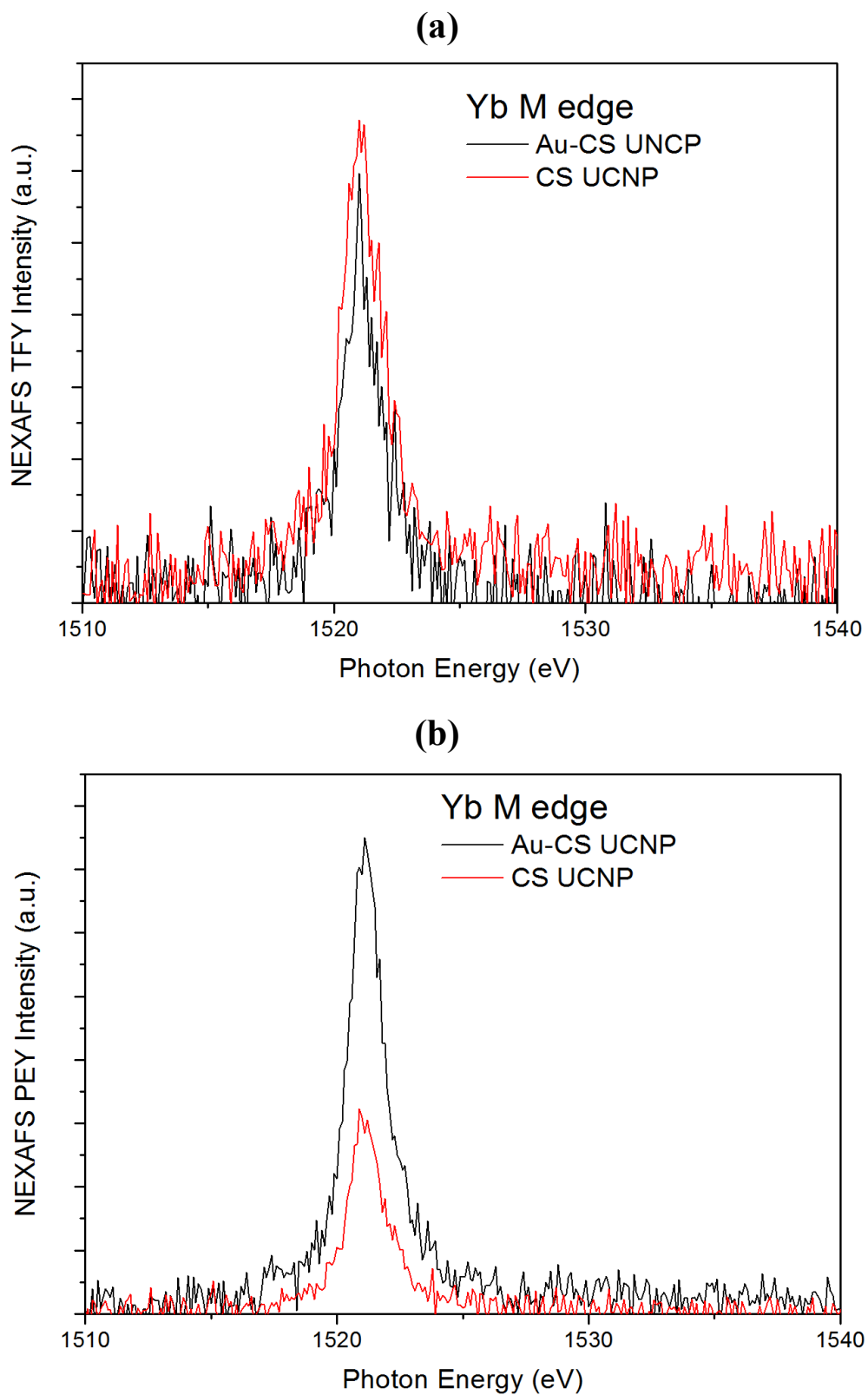


**Figure 5.6** NEXAFS spectra of the Yb M-edge for CS UCNPs with 15 nm shell before (CS-UCNP) and after annealing (Au-CS UCNP) in TFY (a) and PEY (b).

## 5.2.4　Emission Plasmonic Coupling

To study the LSPR of the Au-CS UCNPs, the luminescent upconversion emission profile of the UCNPs and the optical UV-Vis transmission of the dewetted Au nanoparticles were characterised. The overlap between the normalised spectra is shown in Figure 5.7 (a). The 15 nm Au nanoparticles produced from dewetting have their most intense and broad absorption peak centred at 540 nm which identifies their LSPR. The sharp luminescent emission of the UCNPs under 980 nm laser excitation has green emissions at 525 nm and 540 nm and red emissions at 650 nm and 660 nm. The LSPR of the Au nanoparticles overlaps precisely with the green emissions from the $Er^{3+}$ ions radiative transitions of $(^2H_{11/2}, {}^4S_{3/2}) \rightarrow {}^4I_{15/2}$ as shown in Figure 5.7 (b) indicating emission plasmonic coupling enhancement is possible from the Au-CS UCNPs.

**(a)**
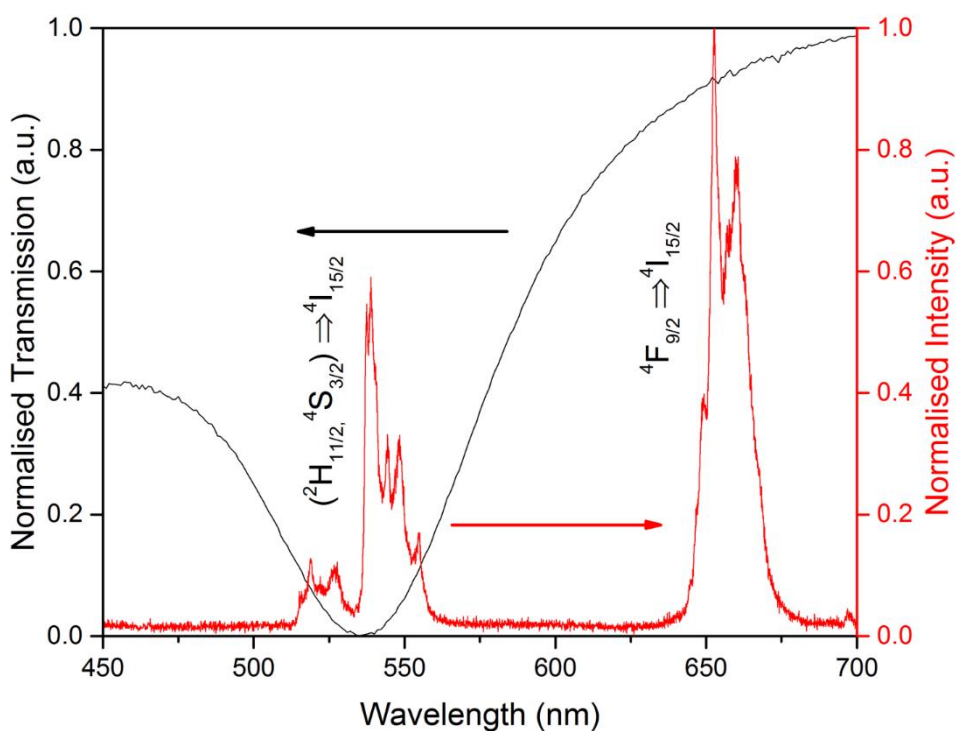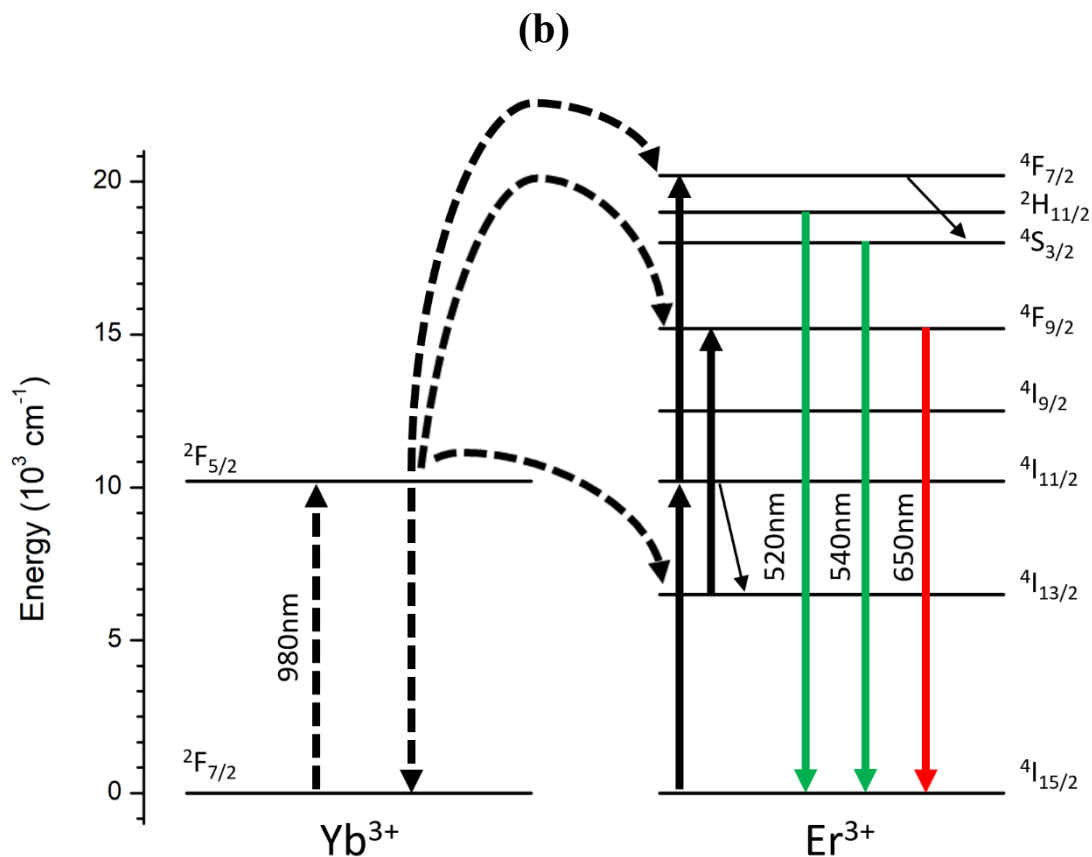
**Figure 5.7** Photoluminescence upconversion spectrum of β-NaYF$_4$:20%Yb,2%Er UCNPs (red) overlaid with UV-Vis transmission of the dewetted Au nanoparticles (black) (a) and the energy level diagram of a Yb$^{3+}$-Er$^{3+}$ upconversion system showing the excitation and the green and red emissions with their respective wavelengths (b). The surface plasmon resonance (~540 nm) of the dewetted Au nanoparticles matches the ($^2$H$_{11/2}$,$^4$S$_{3/2}$) → $^4$I$_{15/2}$ emission of Er$^{3+}$.

## 5.2.5    Single Particle Upconversion Emission

To determine the relationship between shell thickness and luminescent performance of the Au-CS UCNPs, the emission intensity of CS UCNPs, annealed CS UCNPs and Au-CS UCNPs were recorded using a purpose built single nanoparticle scanning confocal microscopy system [23, 59]. The scanned images shown in Figure 5.9 are the upconversion emission points of single core UCNPs (a), CS UCNPs with a 5 nm, 10 nm and 15 nm inert shell respectively (b-d), core Au-UCNPs (e) and Au-CS UCNPs

with a 5 nm, 10 nm and 15 nm inert shell respectively (f-h). Figure 5.8 additionally shows the scanned images of the core UCNPs (a) and CS UCNPs with a 5 nm, 10 nm and 15 nm inert shell respectively (b-d) after annealing under identical conditions but without a Au film. Single UCNPs can be reliably identified using this method due to their small standard derivation in emission intensity. The summary of these emission intensity measurements in Figure 5.9 (i) highlights as reported previously that the emission enhancement of the CS UCNPs saturates at a shell thickness of 5 nm [80], while the luminescent intensity of the annealed CS UCNPs without Au display an insignificant variation to the CS UCNPs as shell thickness is increased. This result suggests that any luminescent enhancement resulting from the improved crystal quality obtained via the reduction of internal defects during the diffusion of dopants as demonstrated by the NEXAFS and simulation results in Figure 5.5 have been effectively cancelled out by the increase in distance between the dopant $Yb^{3+}$ and $Er^{3+}$ ions. This increase in distance between the dopant ions would reduce the probability of energy transfer between $Yb^{3+}$-$Yb^{3+}$ and $Yb^{3+}$-$Er^{3+}$ reducing upconversion emission.

For the luminescent intensity of the Au-CS UCNPs, a clear enhancement dependent on shell thickness is demonstrated. A maximum enhancement factor of 5.5 for total emission is achieved by the 10 nm shell Au-CS UCNPs. This maximum enhancement factor at a spacer separation of 10 nm outperforms similar previously designed structures as listed in Table 5.1 and is consistent with the simulation results in Liu & Lei's work which estimated the optimum separation to be approximately 10 nm [113]. In this work surface plasmon coupling enhancement is applied cooperatively to surface passivated CS UCNPs. This justifies the modest total surface plasmon coupling enhancement factor of 5.5 to be a value approaching the highest feasible factor achievable for the already surface passivated enhanced CS UCNPs.
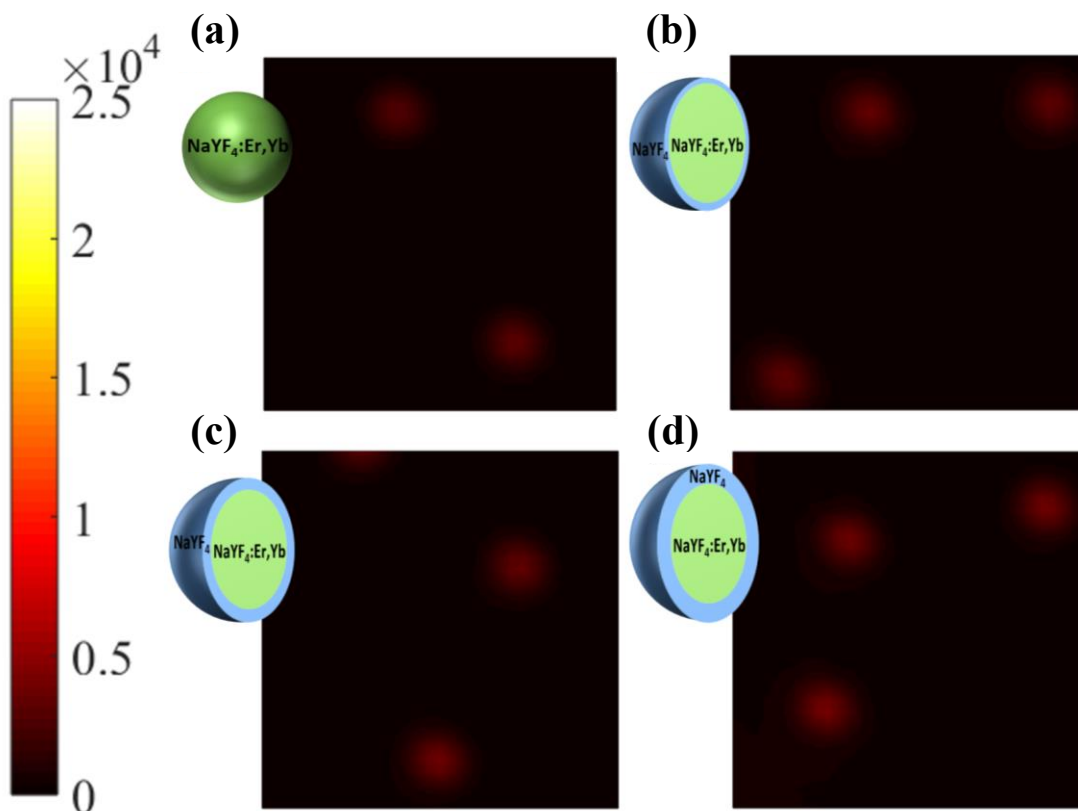
**Figure 5.8** The emission scanning confocal images of the core UCNPs (a) and CS UCNPs with a 5 nm, 10 nm and 15 nm inert shell respectively (b-d) after annealing at 400 °C for 1 hour with no Au. Each scanned image is 3 μm × 3 μm and the colour bar indicates the emission intensity range of the single UCNPs.

**(i)**
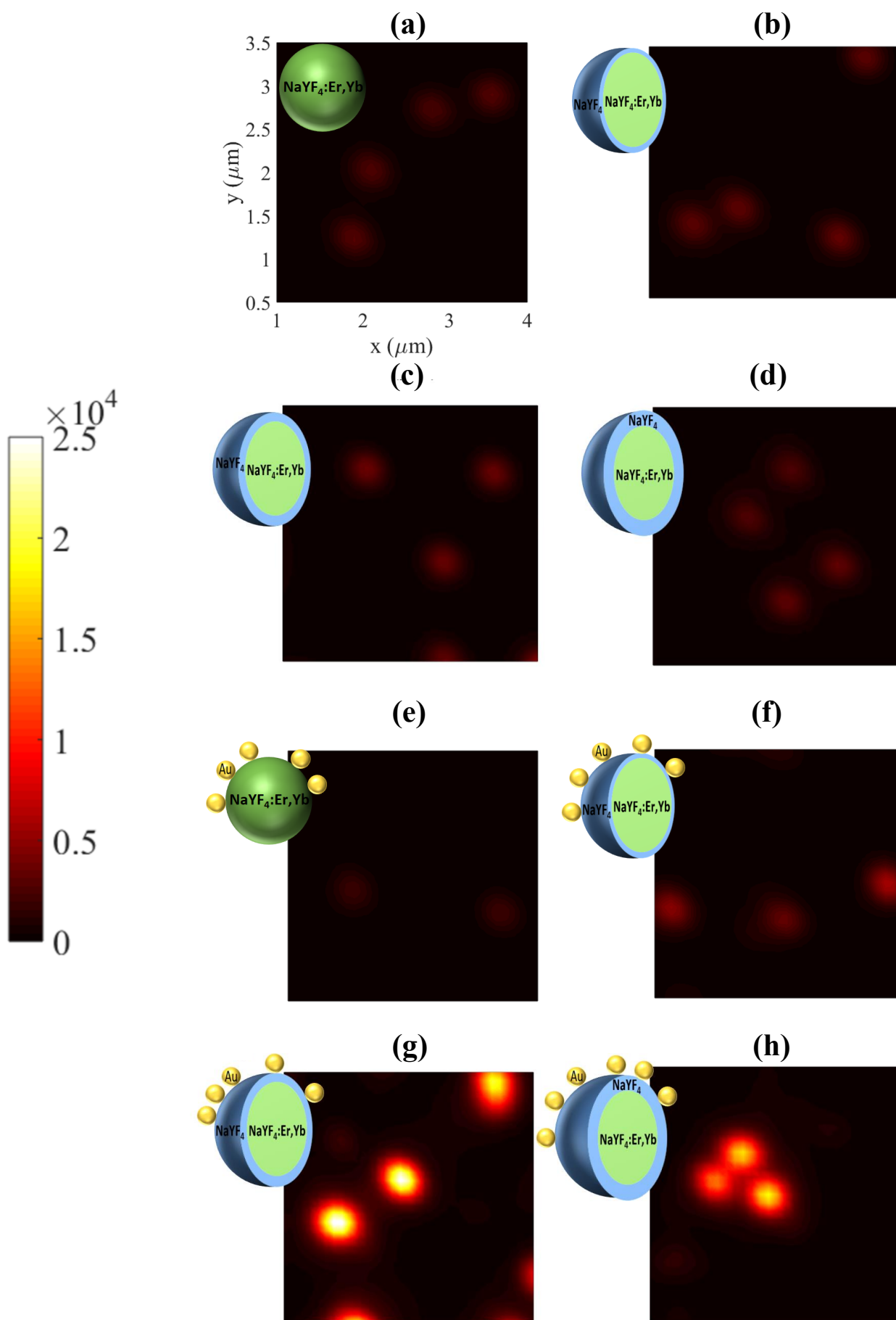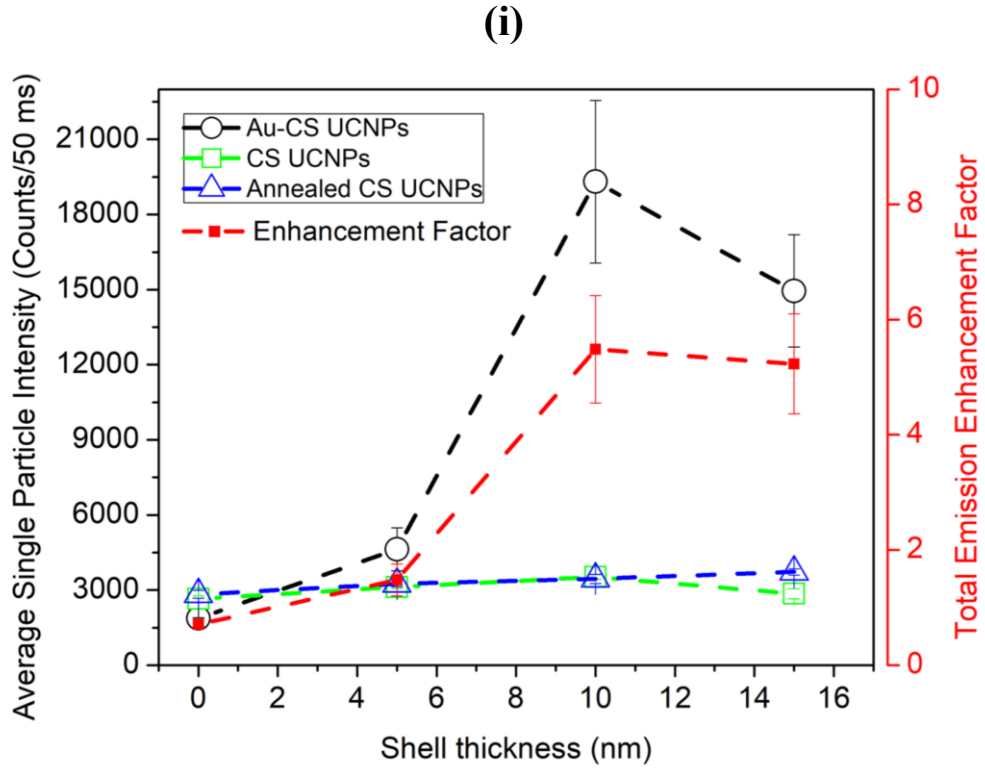
**Figure 5.9** The emission scanning confocal images of the core UCNPs (a), CS UCNPs with a 5 nm, 10 nm and 15 nm inert shell respectively (b-d), core Au-UCNPs (e) and Au-CS UCNPs with a 5 nm, 10 nm and 15 nm inert shell respectively (f-h). Each scanned image is 3 μm × 3 μm as indicated in (a) and the colour bar indicates the emission intensity range of the single UCNPs. Single UCNP total emission intensity and enhancement factor (i) for CS UCNPs (a-d), Au-CS UCNPs (e-h) and annealed CS UCNPs (Figure 5.8 a-d). The laser power was fixed at 20mW, which was measured at the objective back aperture.

**Table 5.1** Comparison of plasmonic metal decorated UCNPs.

| Core UCNP | Spacer | Plasmonic Metal | UCL Enhancement Factor | Ref |
|---|---|---|---|---|
| NaYF$_4$:Yb/Tm | PAA/PAH | Au | ~2.5 | [120] |
| NaYF$_4$:Yb/Er/Gd | - | Au | ~3.9 | [162] |
| NaYF$_4$:Yb/Er | SiO$_2$ | Ag | ~4 | [163] |
| NaYF$_4$:Yb/Er/Tm | Al$_2$O$_3$ | Au | ~5.2/3.5 | [164] |

## 5.2.6 Single Particle Upconversion Lifetime

To investigate the mechanism of the LSPR enhancement on the Au-CS UCNPs, the lifetime of single CS UCNPs and Au-CS UCNPs were measured. It has been reported that the lifetime of the $Yb^{3+}$ $^2F_{5/2}$ energy level increases with inert shell thickness as non-radiative surface quenching processes become passivated more effectively. This increase in the $Yb^{3+}$ $^2F_{5/2}$ lifetime means a higher probability of excitation energy migrating through the nanocrystal to an $Er^{3+}$ activator [80]. This explains the CS UCNPs trend of increasing lifetime with increasing shell thickness displayed in Figure 5.10 (a). Compared to the CS UCNPs there is a significant decrease in lifetime of the Au-CS UCNPs regardless of their shell thickness as shown in Figure 5.10 (b). The 5 nm shell Au-CS UCNPs display the maximum reduction in lifetime decreasing by a factor of 25. This magnitude is clearly shown along with the other CS UCNPs and Au-CS UCNPs lifetimes in the semi-log plot of Figure 5.10 (c). To verify these results the sensitivity of the scanning confocal microscopy system was confirmed by measuring the lifetime of the 976 nm laser which recorded a lifetime of 2.3 μs.

Compared to other plasmonic coupling structures the dramatic reduction in total lifetime observed in the Au-CS UCNPs is consistent with previous research [165] and is among one of the highest recorded [88]. The record in lifetime reduction has recently been claimed by a plasmonic nanocavity structure which reported a 166 fold decrease in lifetime from 20 nm $NaYF_4$: 18% $Yb^{3+}$, 2% $Er^{3+}$ UCNPs achieving sub 2 μs lifetimes [166]. The lifetime result of the Au-CS UCNPs underlies the competition between enhancement and quenching from the Purcell Effect and FRET respectively [167]. For $Er^{3+}$ ions the intrinsic non-radiative recombination rate is higher than the radiative decay rate. When the Purcell Effect spontaneously increases the radiative recombination rate of $Er^{3+}$ ions by increasing the local density of transition states, the emission intensity increases and emission lifetime decreases [164]. In competition to this is FRET where excited $Er^{3+}$ ions transfer energy non-radiatively to the Au nanoparticles, leading to a decrease in both lifetime and emission. FRET is significant when the effective separation distance between the dewetted Au nanoparticles and $Er^{3+}$ activators is below 10 nm [113] especially for these Au-CS UCNPs due to the direct contact of the Au nanoparticles to the surface of the CS UCNP. As a result of this competition, the lifetime of the core Au-UCNPs (11 μs) is longer than that of the

Au-CS UCNPs with shell thicknesses of 5 nm and 10 nm as shown in Figure 5.10 (b). However, as the shell thickness is increased to 15 nm, the influence of FRET starts to diminish and the lifetime recovers, yet the lifetime of the 15 nm shell Au-CS UCNPs is still an order of magnitude lower compared to the lifetime of the 15 nm shell CS UCNPs. This result further reinforces that the Purcell Effect dominates over FRET. Beyond a shell thickness of 10 nm the peak intensity of the Purcell Effect increasing the radiative recombination rate has passed resulting in the decreased intensity in Figure 5.9 (i) and the increased lifetime in Figure 5.10 (b,c) for the 15 nm shell Au-CS UCNPs.

**(a)**
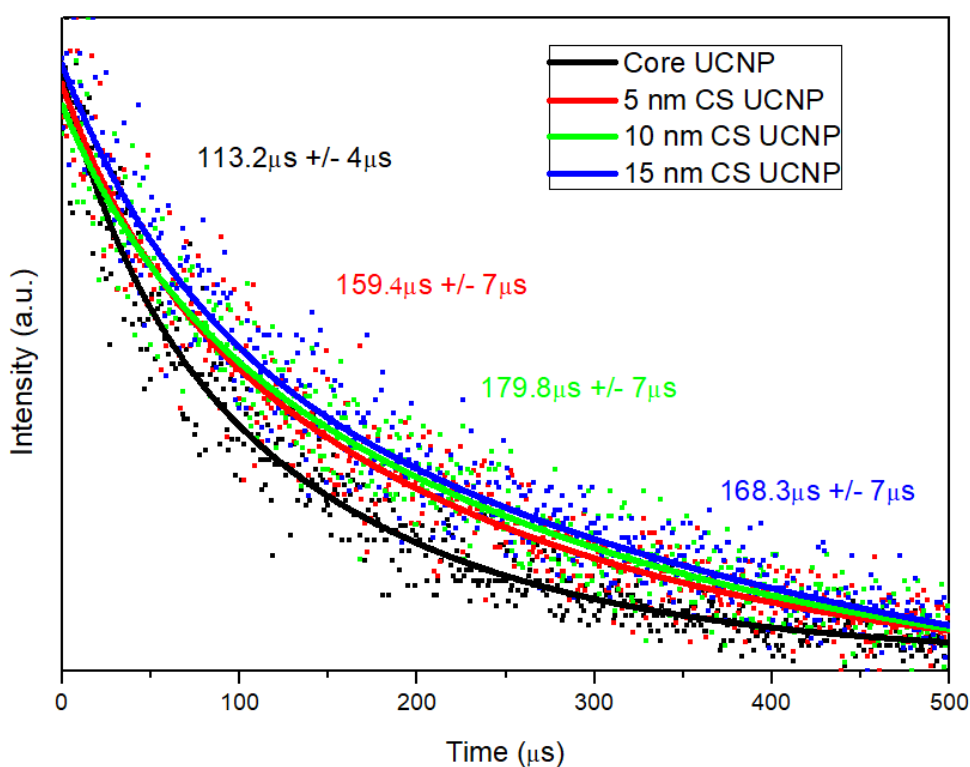
**(b)**
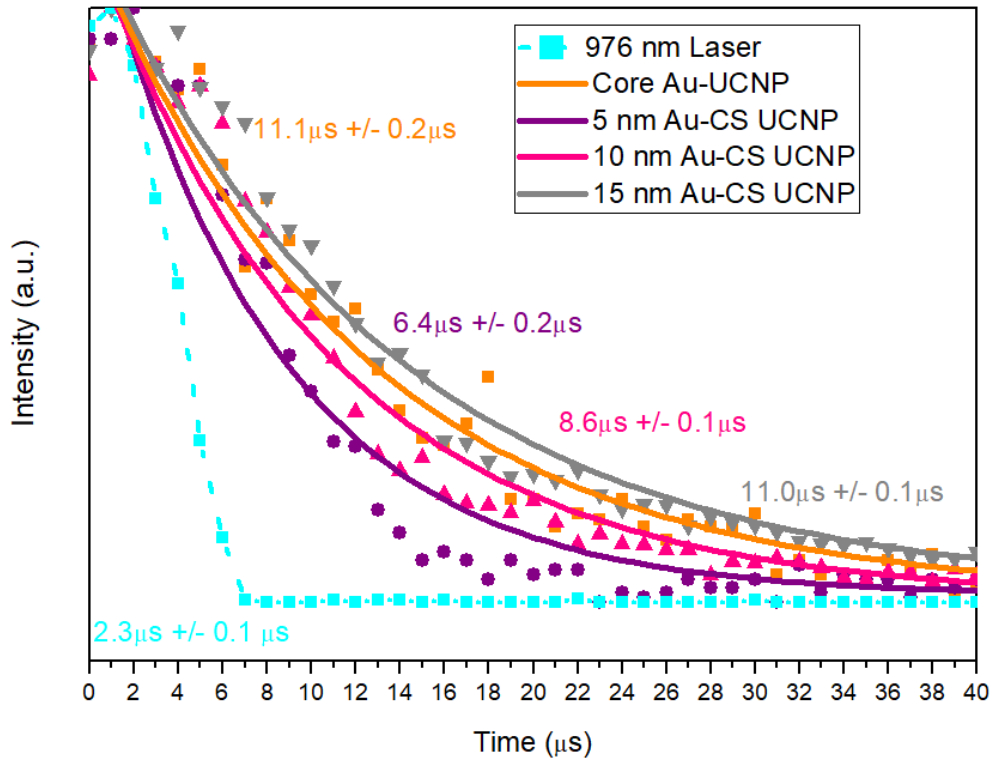


**(c)**
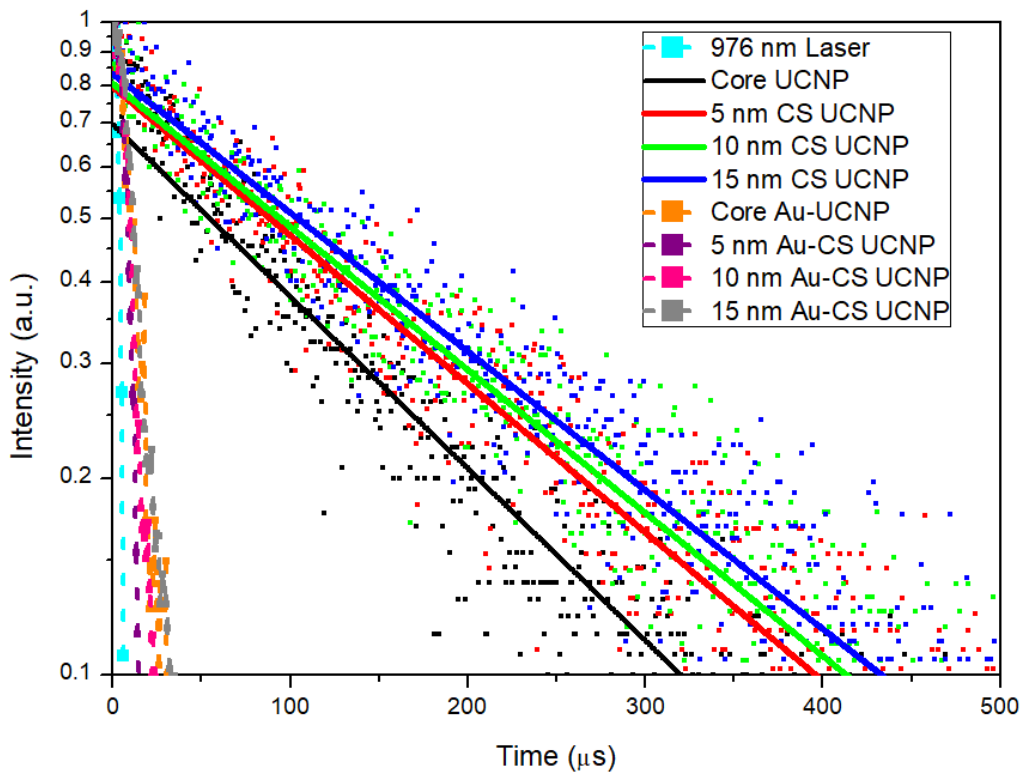
**Figure 5.10** Lifetime measurements of CS UCNPs (a), Au-CS UCNPs (b) and both on semi-log plot (c). The laser power was fixed at 20 mW which was measured at the objective back aperture. The luminescent lifetime of the Au-CS UCNPs decreases by more than an order of magnitude compared to the CS UCNPs.

## 5.2.7 Silver Plasmonic Coupling

Apart from Au, Ag can also be dewetted via rapid annealing to produce Ag nanoparticles [168]. As shown in Figure 5.11 the optimised dewetting parameters produce dewetted Ag nanoparticles with a more intense and wider LSPR compared to the Au nanoparticles which explains the higher upconversion enhancement achieved in plasmonic structures using Ag [164].
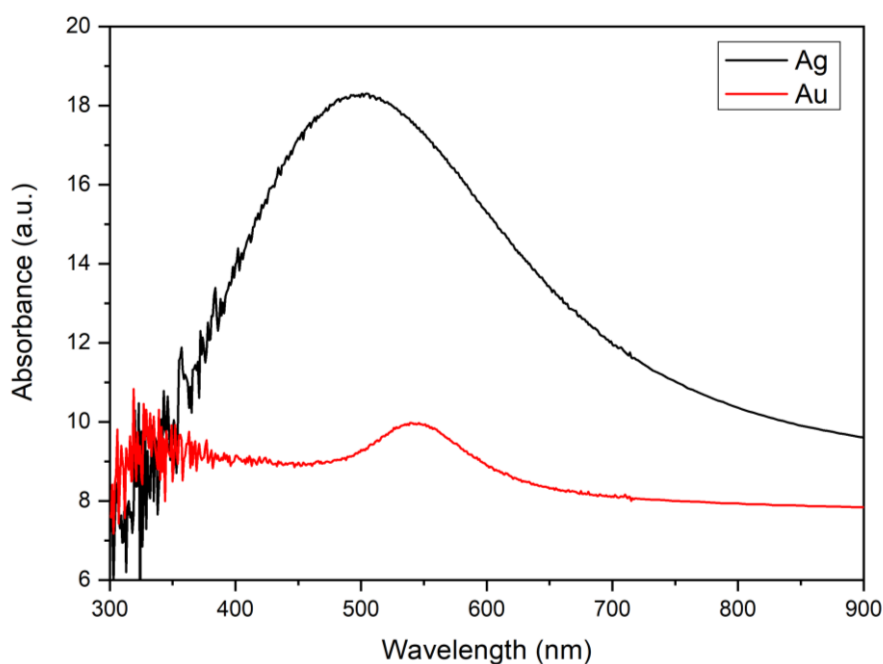


**Figure 5.11** UV-Vis spectra of separate 1 nm films of Au and Ag on glass coverslips after dewetting under nitrogen flow at the optimal parameters of 400 °C for 1 hour and 150 °C for 20 minutes, respectively.

To fabricate the desired decorated core shell structure, the plasmonic nanoparticles are required to be smaller than the UCNPs. Unfortunately for Ag dewetting the ability to control the size of Ag nanoparticles is limited. At the optimal annealing time of 20 minutes the size can only be controlled down to 60 nm [168] and as shown in Figure

5.12 increasing the temperature gives no greater control over shifting the LSPR to the right which would indicate the formation of smaller Ag nanoparticles, instead this only results in decreasing the intensity of the LSPR peak [164]. This issue and the additional problem of the post annealed Ag nanoparticles visibly and rapidly oxidising in air, reducing the LSPR intensity via the formation of a $Ag_2O$ shell [169] were the primary reasons for not proceeding with a Ag-CS UCNP design.
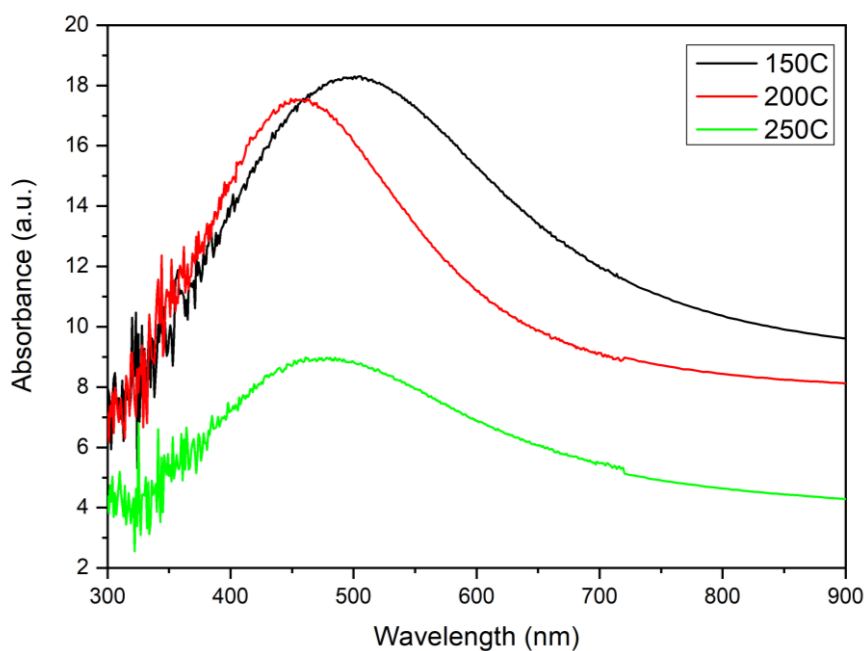


**Figure 5.12** UV-Vis spectra of 1 nm Ag films annealed at 150 °C, 200 °C and 250 °C respectively for 20 minutes under nitrogen flow.

## 5.2.8    Au-CS UCNPs Transfer

Several attempts were made to determine the ability of the Au-CS UCNPs to be transferred or produced on other substrates for application or improved characterisation.

Initially attempts to perform the same dewetting procedure of Au on Cu TEM grids containing UCNPs were attempted as Cu TEM grids are graded stable up to 600 °C and the annealing performed is only 400 °C [170]. However, as shown in Figure 5.13 (a) Au does not effectively dewet on the surface of the Cu TEM grid producing large irregular shaped nanoparticles. It is of interest to note that the UCNPs can still be identified on the Cu TEM grid as circled red in Figure 5.13 (b). These UCNPs

magnified in Figure 5.13 (c,d) show how compared to the Cu TEM grid surface the Au has still been able to dewet uniformly on the $NaYF_4$ surface indicating a dramatic difference in surface energy between the Cu TEM grid and $NaYF_4$ surfaces.
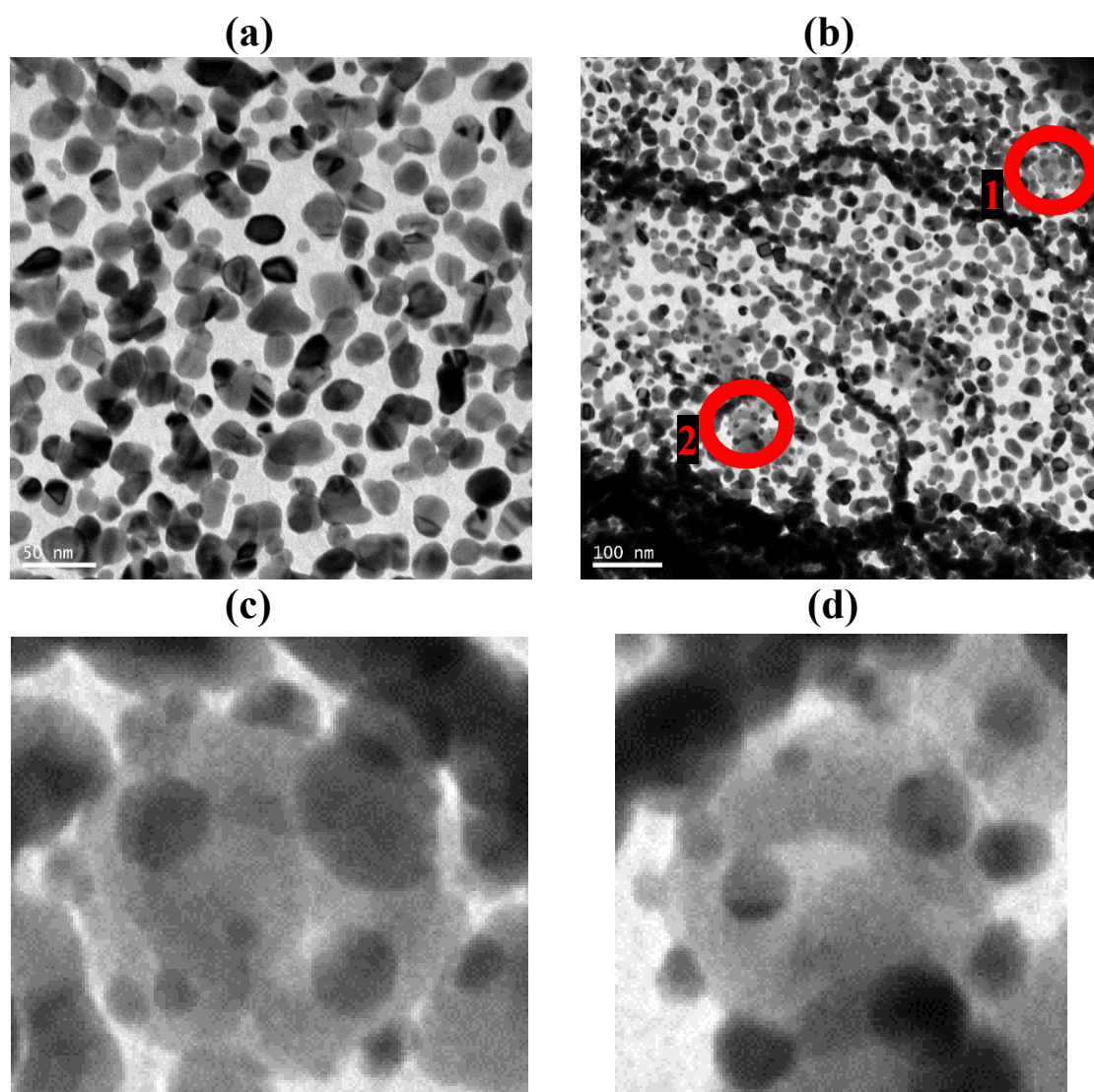


**Figure 5.13** Au dewetted on the surface of a Cu TEM grid (a). UCNPs visible on the Cu TEM at highlighted positions 1 and 2 showing that the Au still dewets effectively on the surface of the UCNP. Magnified positions 1 and 2 in (b) highlighting this contrast in the dewetted Au nanoparticles (c,d).

For application of these Au-CS UCNPs it would be useful for them to be transferred to other substrates as required. To determine if the Au-CS UCNPs were able to be transferred a PMMA spincoat and buffered oxide etch lift-off procedure was attempted [171]. The results of attempting this process highlighted two major issues

the first being evident in the transition between Figure 5.14 (a) to Figure 5.14 (b) where prominent etching has occurred to the UCNPs damaging their uniform morphology. This significant etching of the UCNPs is a result of the concentrated NaOH used for the lift-off of the PMMA. The second issue is the total absence of any Au nanoparticles still attached to the UCNPs after the lift-off indicating the weak nature of the bonding between the bare Au surface to the $NaYF_4$ surface.

**(a)**                                            **(b)**
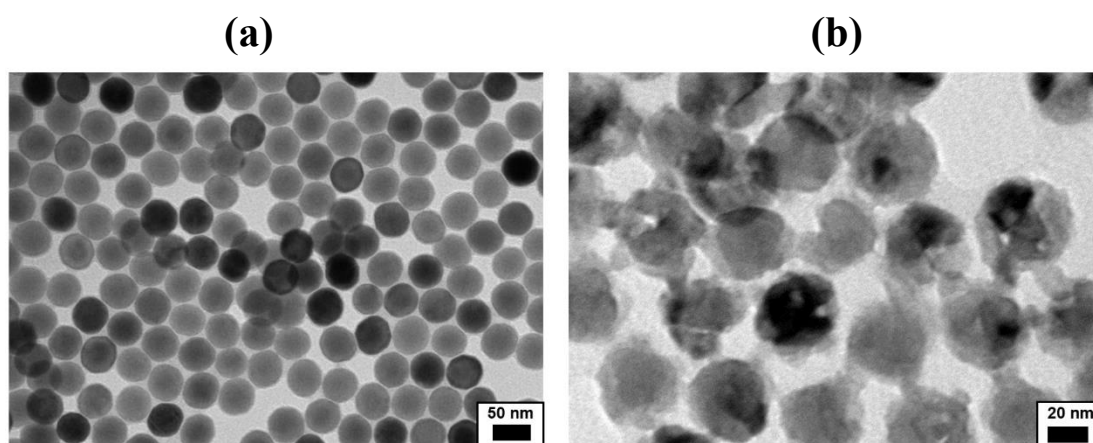


**Figure 5.14** CS UCNPs before PMMA spincoat and buffered oxide etch procedure (a) and Au-CS UCNPs after PMMA spincoat and buffered oxide etch procedure (b).

# 5.3     Summary

Based on the lanthanide distribution findings surface plasmon coupled enhanced UCNPs were designed and fabricated. The upconversion emission intensity of single Au-CS UCNPs were quantitatively characterised using a scanning confocal microscope. The results demonstrate an inert shell thickness dependent enhancement with a maximum emission enhancement factor of 5.5 in total emission intensity achieved by the 10 nm shell Au-CS UCNPs. The Au-CS UCNPs were further investigated by XRD, UV-Vis and NEXAFS to confirm phase retention, emission plasmonic coupling and identify dopant diffusion occurring during fabrication. These results further increase understanding of lanthanide distribution within $NaYF_4$ UCNPs. Investigations into improving the enhancement with this design by using Ag were promising however several issues including particle size and stability ultimately made this infeasible. Additionally, the inability of the Au-CS UCNPs to be transferred effectively for application concluded any further investigations.

# Chapter 6

# 2D Lanthanide-doped NaYF$_4$: Yb$^{3+}$, Er$^{3+}$ Nanosheets

## 6.1    Introduction

Synthesis of new 2D materials can lead to exciting material properties not present in the bulk due to quantum confinement effects. NaYF$_4$ is one of the most efficient host materials for luminescence lanthanide upconversion yet reports of upconversion properties of NaYF$_4$ in two-dimensional (2D) sheet-like structures have been scarce [97, 172]. In this chapter the fabrication of NaYF$_4$: Yb$^{3+}$, Er$^{3+}$ 2D nanosheets using a soft liquid-phase exfoliation method along with their optical and electronic properties are presented.

The possibility that bulk NaYF$_4$ can be exfoliated was modelled initially by means of Density Functional Theory (DFT) calculations performed by Sherif Tawfik within the Vienna Ab initio Simulation Package (VASP) as shown in Figure 6.1 (a). These calculations concluded it is possible for NaYF$_4$ to be cleaved through the (001) plane. Figure 6.1 (b) predicts to cleave the crystal at this facet would require -2.43 eV per unit cell, a challenge considering this energy is two orders of magnitude greater than the energy commonly required to cleave van der Waals crystals [98]. The electronic properties of this theoretical 2D material were also examined by calculating the partial density of states (PDOS) and band structure as shown in Figure 6.1 (c). The main features and dominating states of the bands are similar to those obtained for the bulk β-NaYF$_4$ in Figure 6.1 (d), although the band gap is smaller for the 2D. The band gap calculated for the bulk β-NaYF$_4$ is 7.5 eV, whereas for the 2D NaYF$_4$ the value is 6.0 eV. The narrowing of the band gap could be explained by a transfer of charge on the

surface of the 2D nanosheet [173]. To determine the charge on the surface, Bader charge calculations were performed and the results in Table 6.1 indicate a charge transfer occurring with each of the top and bottom Y atoms of the crystal losing 1-2% more charge in the 2D $NaYF_4$ than the corresponding atoms in the bulk $\beta$-$NaYF_4$. The surface F atoms in the 2D $NaYF_4$ gain 2% more charge than the corresponding atoms in the bulk $\beta$-$NaYF_4$. This amounts to a gain of 0.06|e| in the surface F atoms. This transfer and accumulation of charge on the surface is likely due to a distribution of dangling bonds present after cleavage.

Bottom-up synthesis attempts to produce 2D $NaYF_4$ in an intermediate stage before the formation of self-assembled upconversion nanorods via a low temperature ion exchange method were unsuccessful [97, 172]. However, a top-down exfoliation of bulk $NaYF_4$ microcrystal to produce 2D $NaYF_4$ nanosheets was successful. Using an inherently simple 'soft' liquid phase exfoliation method [174] that does not require intensive ultrasonication like other reported liquid phase exfoliation methods [175, 176] bulk $NaYF_4$: $Yb^{3+}$, $Er^{3+}$ microparticles were cleaved to produce 2D $NaYF_4$: $Yb^{3+}$, $Er^{3+}$ nanosheets.



**(a)**

**(b)**



**(c)**

**(d)**
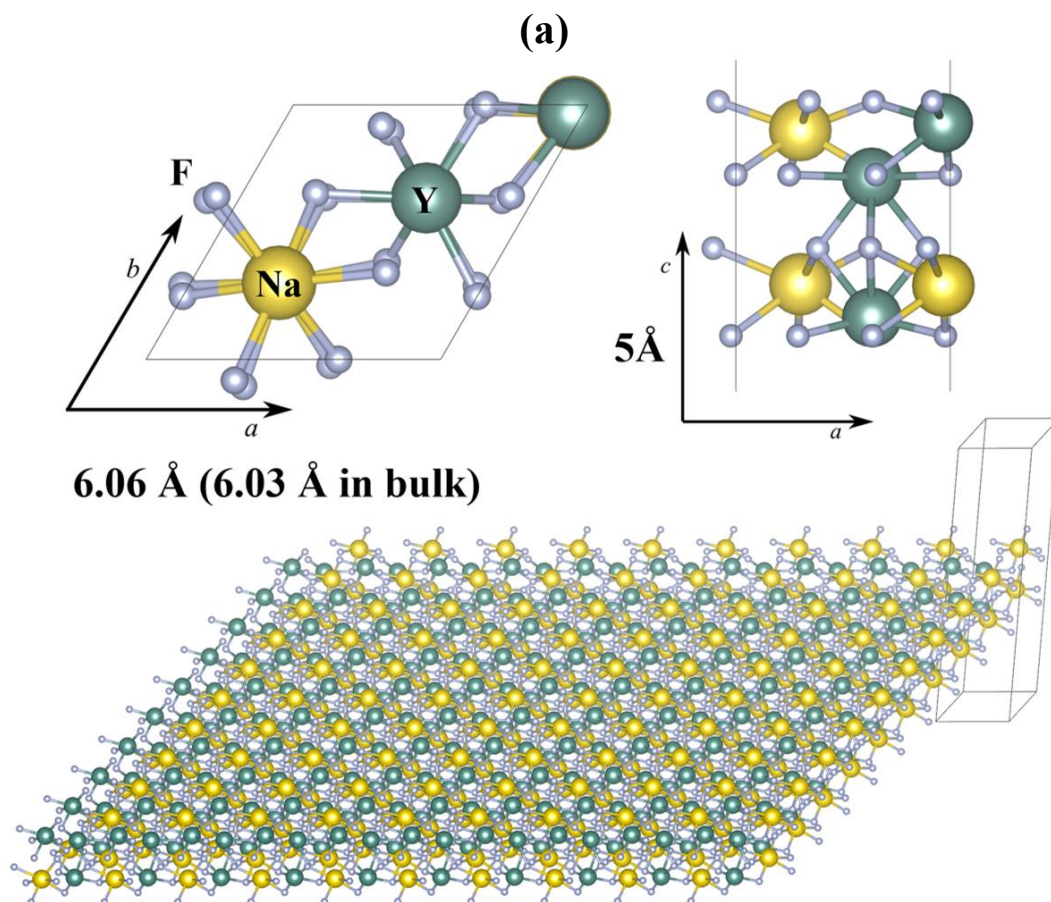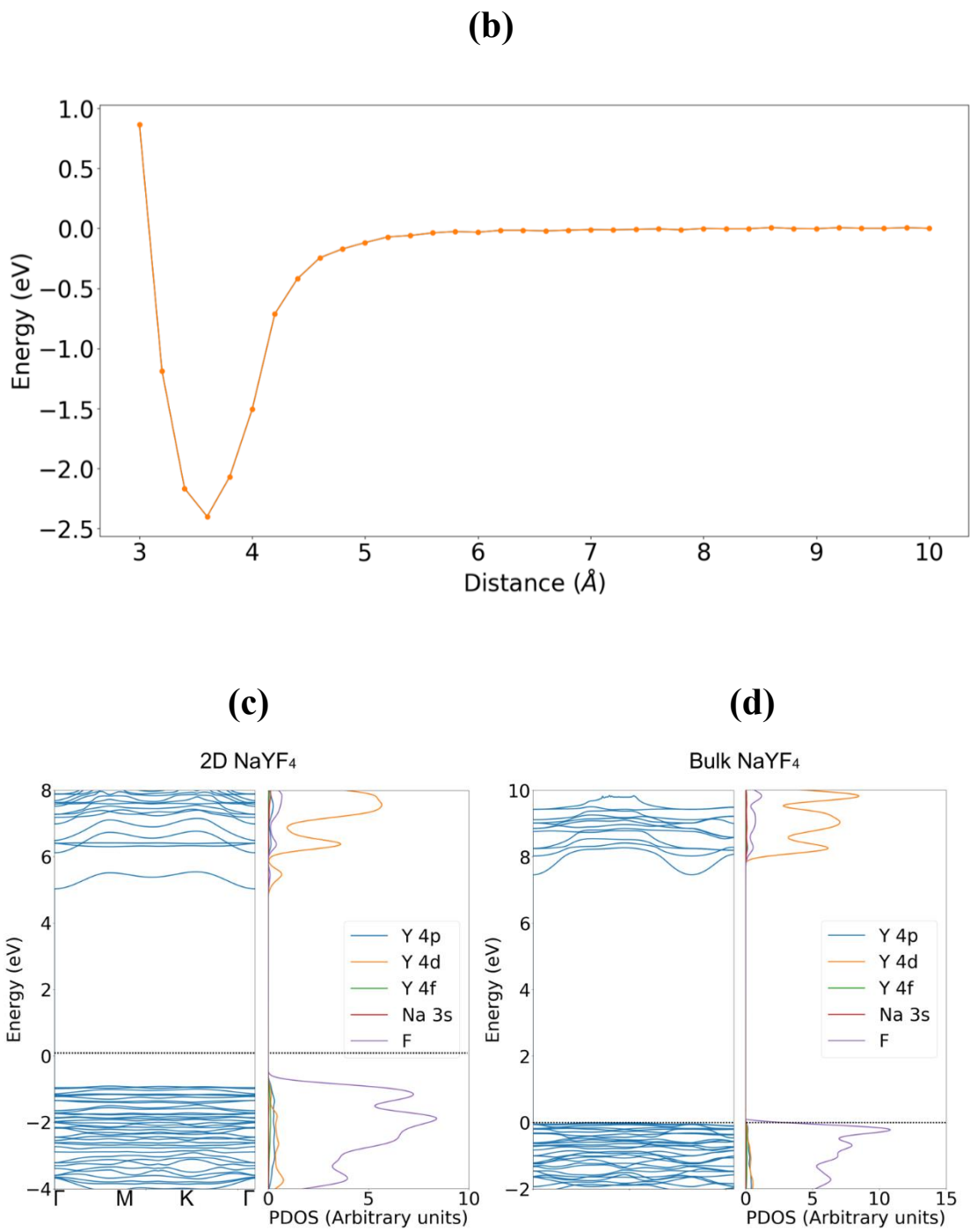


**Figure 6.1** Modelled crystal structure of a 2D (001) β-NaYF$_4$ monolayer, which has a thickness of 0.5 nm after geometry optimization (a). Cleave energy along the (001) plane (b). Band structure and partial density of states of 2D (001) β-NaYF$_4$ (c) and bulk β-NaYF$_4$ (d).

**Table 6.1** The calculated Bader charges on the atoms of the unit cell, comparing those in the 2D (001) $NaYF_4$ unit cell and the bulk $NaYF_4$ crystal. Atoms that lie close to the surface are indicated in bold.

| Atom | 2D $NaYF_4$ | Bulk $NaYF_4$ |
|---|---|---|
| Y (surface) | **-2.350** | -2.320 |
| Y (surface) | **-2.346** | -2.297 |
| Y | -2.350 | -2.358 |
| Na | -0.857 | -0.855 |
| Na | -0.850 | -0.854 |
| Na (surface) | **-0.842** | -0.836 |
| F (surface) | **0.802** | 0.802 |
| F (surface) | **0.799** | 0.802 |
| F (surface) | **0.803** | 0.802 |
| F (surface) | **0.795** | 0.789 |
| F | 0.799 | 0.786 |
| F | 0.802 | 0.796 |
| F | 0.803 | 0.786 |
| F (surface) | **0.794** | 0.790 |
| F | 0.794 | 0.796 |
| F | 0.803 | 0.796 |
| F (surface) | **0.802** | 0.788 |
| F | 0.799 | 0.786 |

# 6.2     Characterisation

## 6.2.1     Morphology

The SEM image of the parent microparticles in Figure 6.2 (a) and the TEM image of a representative exfoliated nanosheet in Figure 6.2 (b) demonstrate the success of the exfoliation method for $NaYF_4$: $Yb^{3+}$, $Er^{3+}$. The images show a clear transformation from faceted microparticles with diameters in the range of 1 μm – 5 μm to $NaYF_4$: $Yb^{3+}$, $Er^{3+}$ nanosheets, which appear to have a thickness of a few atomic layers. The lateral dimensions of the nanosheets is typically hundreds of nanometres to more than

1 μm. High resolution TEM images in Figure 6.2 (c,d) of a single nanosheet reveal a highly ordered atomic structure, with lattice spacings of 0.52 nm and 0.31 nm in different regions, which can be indexed to the β and α phases of $NaYF_4$ respectively [177, 178]. This plane assignment of the nanosheet is further revealed by the corresponding FFT patterns shown in the insets of Figure 6.2 (c,d) with all the diffraction spots assignable to the [100] zone axis and [110] zone axis of the β-hexagonal and α-cubic phases of $NaYF_4$ respectively [178, 179].

**(a)**
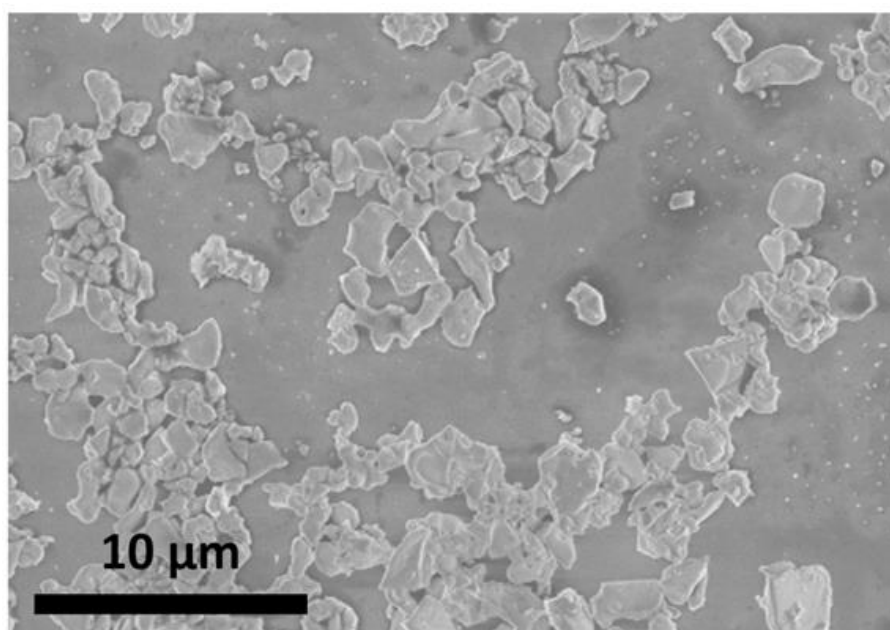


**(b)**
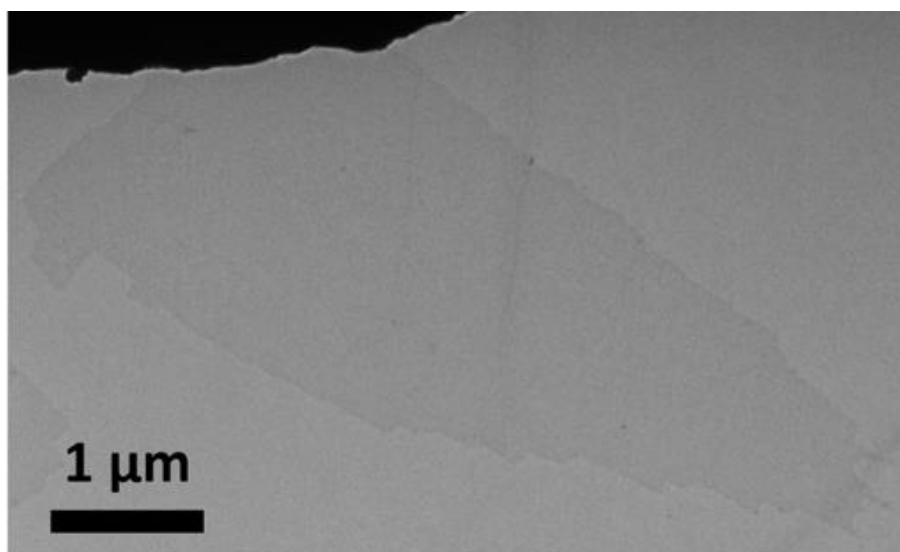
**(c)**
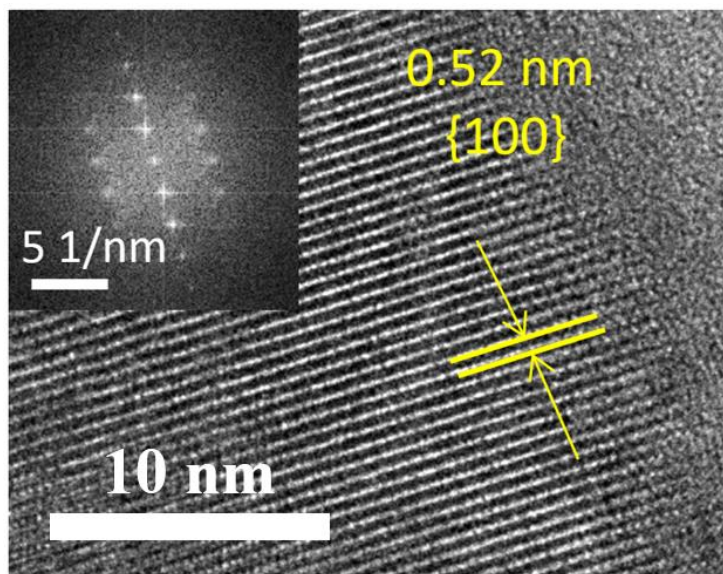


**(d)**
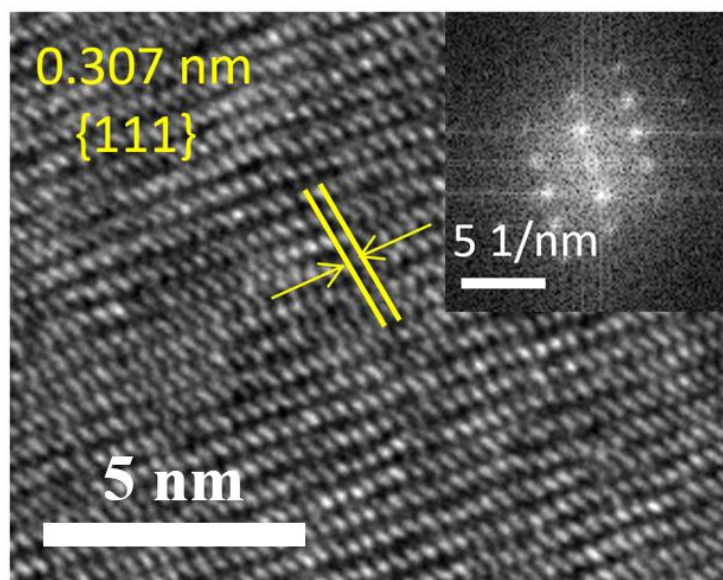


**Figure 6.2** SEM image of faceted bulk NaYF$_4$ microparticles, with sizes in the range of 1 μm – 5 μm, prior to exfoliation (a). TEM image of an exfoliated nanosheet showing constant thickness as evidenced from the uniform contrast (b). High resolution TEM images showing the atomic structure of a single nanosheet, which reveals a highly ordered crystalline 2D structure (c,d). This is also evident from the corresponding FFT patterns (inset).

## 6.2.2    Nanosheet Thickness

To experimentally determine the monolayer thickness AFM measurements were performed. As shown in Figure 6.3, the AFM images of the 2D sample shows a variety of NaYF$_4$: Yb$^{3+}$, Er$^{3+}$ nanosheets with lateral dimensions in the micrometre range and thickness down to 0.9 nm +/- 0.1 nm which approximately matches the thickness of a monolayer calculated by DFT. Thicker nanosheets up to 16 monolayers, as shown in Figure 6.3 (b,c) contain several flat terraces and few-monolayer steps. It is likely these nanosheets are composed of multiple sheets stacked on top of each other. The regions of different thickness within a single nanosheet in some cases are indicative of the transient state of partial delamination during the exfoliation process and is typical of 2D materials obtained from liquid phase exfoliation techniques.

**(a)**



**(b)**
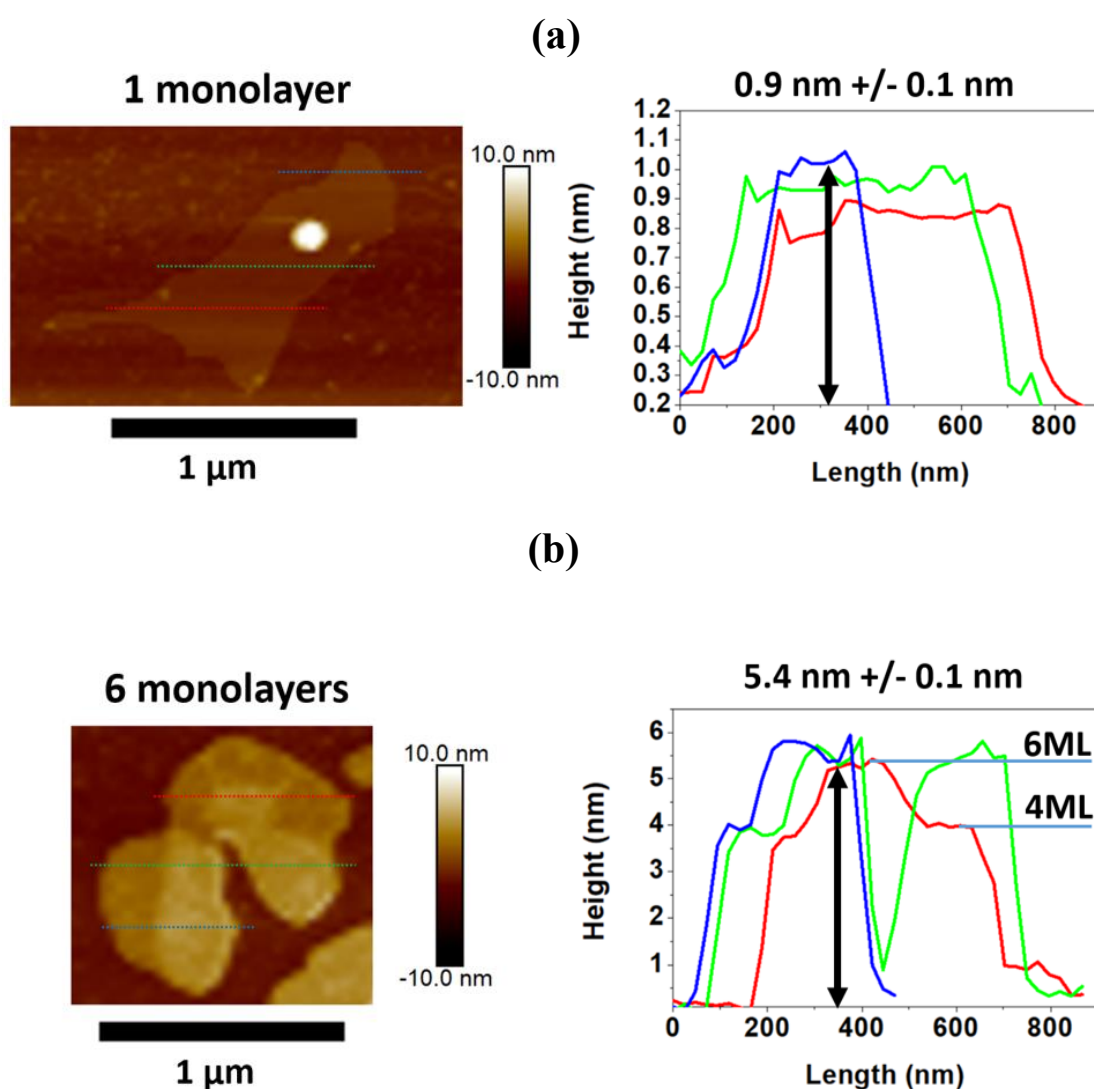
**(c)**
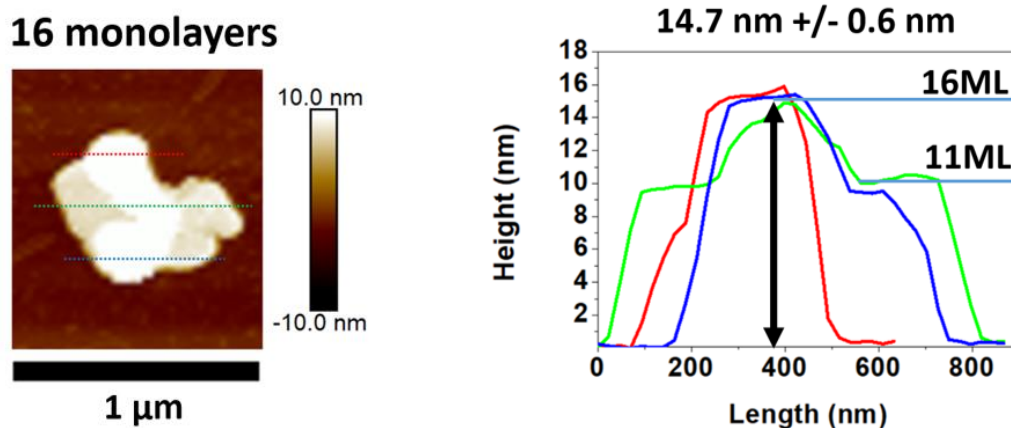


**Figure 6.3** AFM images of several $NaYF_4$: $Yb^{3+}$, $Er^{3+}$ nanosheets with the lateral dimension in the micrometre range and thickness between one and 16 monolayers. The nanosheet in (a) is a monolayer, while nanosheets in (b) and (c) are aggregates composed of several monolayers stacked on top of each other. Height profiles along the red, green and blue dashed lines reveal atomic flat domains with an average surface roughness (~0.1 nm) significantly smaller than the thickness of a $NaYF_4$: $Yb^{3+}$, $Er^{3+}$ monolayer.

## 6.2.3     Crystal Structure

To confirm a single highly crystalline nanosheet can harbour both β and α phases simultaneously, XRD analysis was performed on the samples. Figure 6.4 (a) is the typical XRD spectra of the bulk and exfoliated $NaYF_4$: $Yb^{3+}$, $Er^{3+}$ nanosheets. The two samples exhibit sharp diffraction peaks that can be indexed to a mixture of β-$NaYF_4$ (JCPDS no. 16-0334) along with α-$NaYF_4$ (JCPDS card no. 06-0342). The α-phase is considerably enriched after exfoliation with the ratio of the β-phase (201) diffraction peak to the α-phase (111) diffraction peak increasing by a factor of 2.5. The observed enhancement of the (100) plane as evidenced by the change in the relative intensity to the (110) and (201) peaks along with enhancement of peak broadness highlighted in Figure 6.4 (b) indicates that the $NaYF_4$ crystal is preferentially cleaved along this plane supporting the TEM and FFT results. The

strong XRD (100) peak suggests the exfoliation occurs preferentially by breaking the stacking of NaYF$_4$ basal planes.
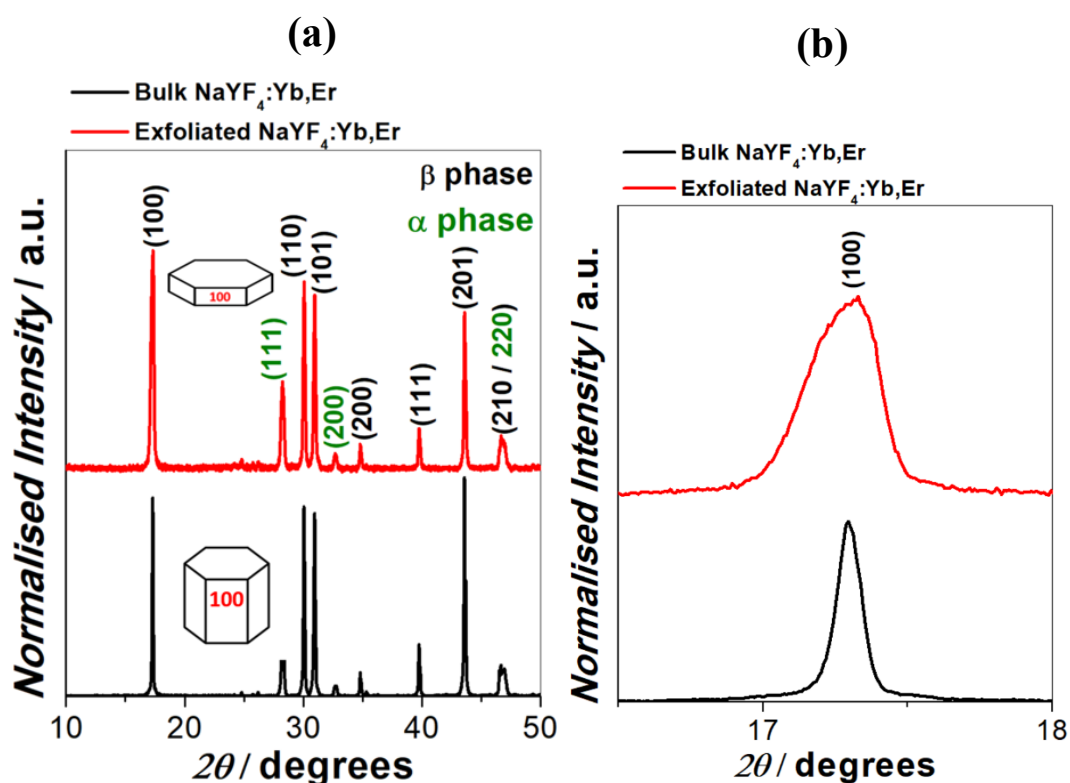


**Figure 6.4** XRD spectra of parent microparticles and nanosheets with the peaks from the β phase (JCPDS no. 16-0334) and α phase (JCPDS no. 06-0342) (a). Magnified XRD spectra at the (100) peaks highlighting the enhanced broadness in the nanosheets spectrum compared to the bulk spectrum (b).

Raman spectroscopy was employed to further investigate the crystal structure of the NaYF$_4$: Yb$^{3+}$, Er$^{3+}$ nanosheets and bulk. Consistent with the XRD data, the Raman spectrum shows that the parent microcrystals are predominantly β-phase along with only a small portion of the α-phase, the Raman spectra of the parent microcrystals and 6 monolayer (ML) nanosheets in Figure 6.5 exhibit sharp peaks at 254 cm$^{-1}$, 299 cm$^{-1}$ and 359 cm$^{-1}$ characteristic of the β-phase while the broad Raman band at 260 cm$^{-1}$ of the α-phase is not observed [50, 180]. The thickness of the nanosheets was estimated by the intensity of the Si Raman signature at 521.7 cm$^{-1}$ from the underlying Si substrate. The Si signature is absent from the bulk spectrum, whereas the Si signature intensifies in the nanosheet spectra as the thickness reduces from 6 ML to 1 ML. For

the 6 ML nanosheet, the sharp Raman bands associated with the β-phase in the bulk start to broaden, whereas for the single ML nanosheet that appeared as a near-transparent monolayer under the optical microscope, only the broad peaks characteristic of the α-phase are observed. The strong Raman band at 260 cm$^{-1}$ in the 1 ML nanosheet signifies the dominant α-phase [180] and a phase transition from beta to alpha as the nanosheets are thinned towards a single monolayer. Therefore, XRD and Raman studies validate that during exfoliation the mixed-phase NaYF$_4$: Yb$^{3+}$, Er$^{3+}$ crystals tend to preference α-phase post exfoliation.
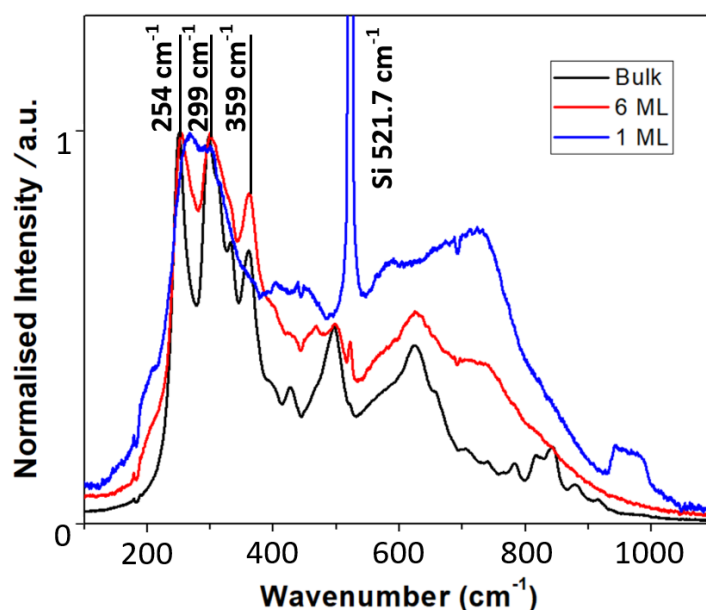


**Figure 6.5** Normalised Raman spectra of bulk and 2D NaYF$_4$: Yb$^{3+}$, Er$^{3+}$ nanosheets estimated to comprise of 1 and 6 monolayers (ML).

## 6.2.4    Revised DFT

Given that the experimental results indicate that the exfoliation occurs preferentially along the (100) plane (as revealed by TEM/FFT and confirmed by XRD/Raman), the structural and electronic properties of an undoped NaYF$_4$ (100) plane monolayer were recalculated by Sherif Tawfik using DFT as a tool to validate the experimental results. For these calculations to create a nanosheet, the bulk is cleaved along the (100) plane producing a stoichiometric (100) surface orientated β-NaYF$_4$ layer with a thickness of two-unit cells that is a pristine 2D system which is not passivated on either side. The electronic structure of the surface of the system is similar to 2D materials that are not

derived from van der Waals solids such as silicene and germanene. In these materials, according to DFT, broken bonds result in the re-distribution of electronic charge throughout the solid. This means that some broken bonds will have a localised electron density (dangling bonds) while others will not. In a realistic environment, the dangling bonds are likely to bind with ambient gas molecules. This is in contrast to most other van der Waals 2D materials but is not an exception [181]. 2D metal-free graphitic-$C_3N_4$ nanosheets with retained dangling bonds produced from liquid exfoliation of bulk material have been reported [182]. The dangling bonds on these nanosheets were demonstrated to induce ferromagnetism in the material. Considering this example, it is possible that the dangling bonds are retained on the non-van der Waals 2D $NaYF_4$.

The thickness of a nanosheet after cleavage and geometrical structure optimisation of the atoms is found to be 0.914 nm which is in agreement with the measured AFM value for a monolayer. It is of interest to note that the resultant relaxed structure of Figure 6.6 (d) shows significant deviation from the beta phase. While the relaxed monolayer is not perfectly alpha phase this result further confirms that as the $NaYF_4$ lattice is restricted to the 2D it will relax away from the beta phase towards the alpha phase. The optimised structure of the monolayer is displayed along three main axes in Figure 6.6 (a-c), with lattice parameters $b = 6.087$, $c = 7.252$, $\alpha = 90.0°$, $\beta = 90.1°$, $\gamma = 125.4°$. The cohesive energy of this structure is -5.34 eV/atom, which is close to the cohesive energy of -5.45 eV/atom for the bulk system.

**(a)**

**(b)**



**(c)**



**(d)**
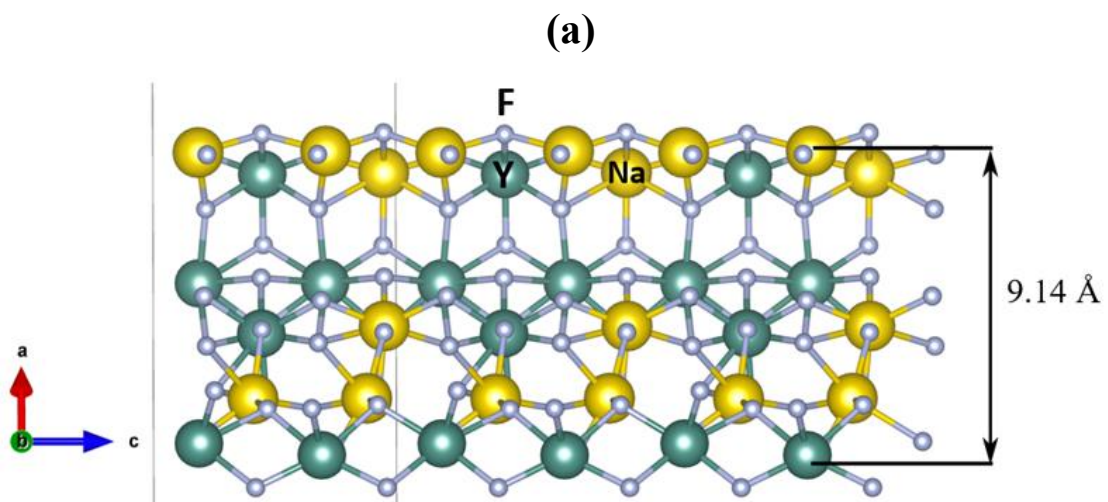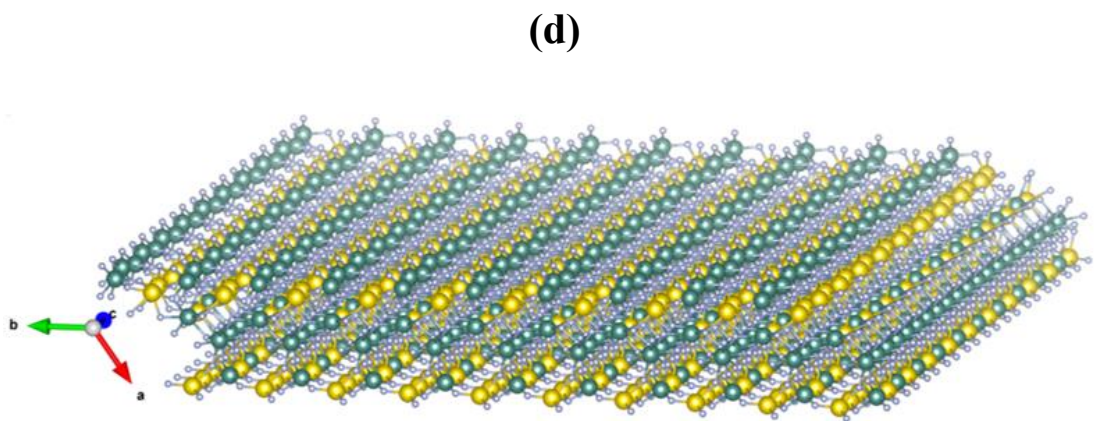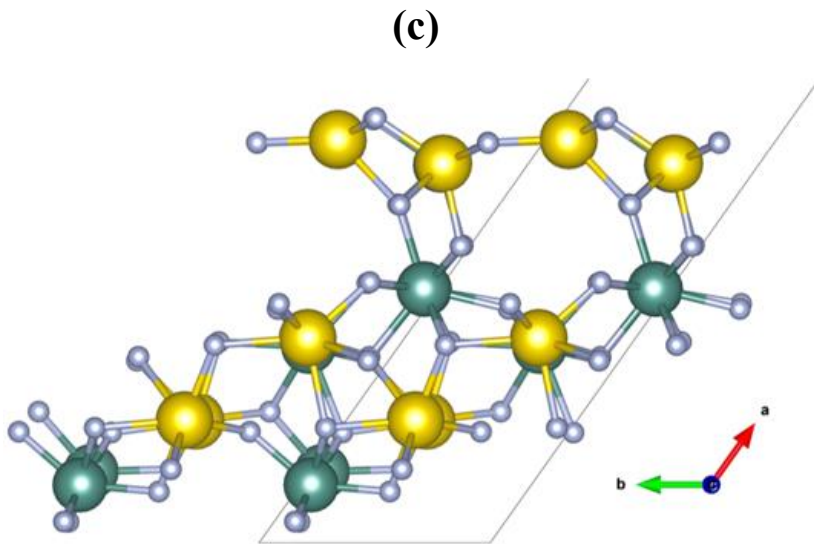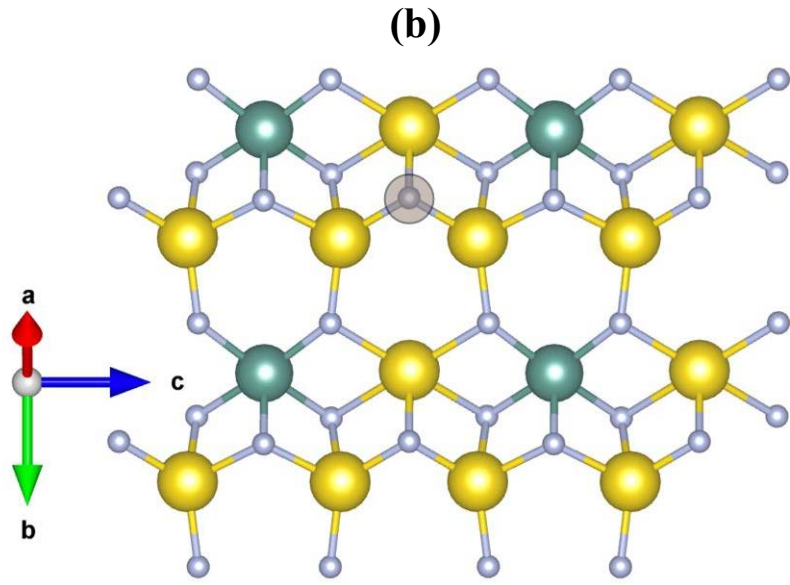
**Figure 6.6** Modelled crystal structure of (100) β-NaYF$_4$ monolayer viewed along three main crystal axes (a-c). The monolayer has a thickness of 9.14 Å after geometry optimisation. After cleavage, the surface F atom (lightly shaded and highlighted grey in (b) relaxes inwards, while two Na atoms in the second layer relaxes upwards, resulting in a bonding coordination defect. Perspective view of the nanosheet after geometry relaxation (d).

## 6.2.5    Chemical Structure

The high-resolution EDS maps of Na, Y, F, Er and Yb in Figure 6.7 (a) and corresponding EDS spectra in Figure 6.7 (b) confirms that the nanosheets and bulk are NaYF$_4$ and that both dopant ions (Er$^{3+}$ and Yb$^{3+}$) are still present across the nanosheet after exfoliation however it appears that the Yb$^{3+}$, Er$^{3+}$ and Y$^{3+}$ ions have been preferentially depleted relative to Na$^+$ and F$^-$ ions after exfoliation. Variations in the spectra are a consequence of different microscopes being used: Zeiss Supra 55VP SEM with an acceleration voltage of 10 kV for the microcrystals and Jeol 2100F TEM with an acceleration voltage of 80 kV for the nanosheet.

This result indicates that the soft exfoliation method allows the nanosheets to retain both dopants ions, signifying that the nanosheets are potentially optically active with both upconversion and downconversion emission present under the correct laser excitation.
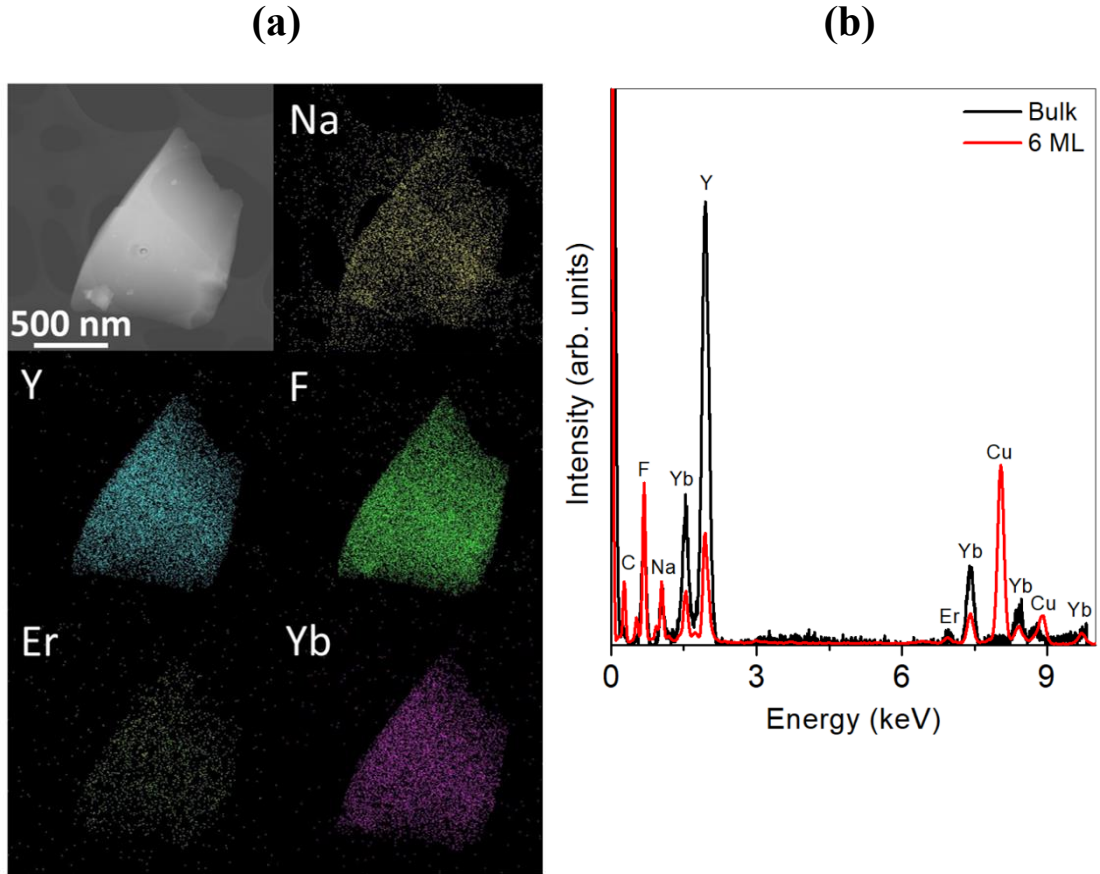
**Figure 6.7** EDS elemental maps of Na, Y, F, Er and Yb, showing uniform distributions of the dopant ions across the nanosheet (a). EDS spectra of nanosheet and bulk (b).

## 6.2.6 Optical Emission

To optically characterise the lanthanide sensitizer and activator ions of the bulk $NaYF_4$: $Yb^{3+}$, $Er^{3+}$ and 2D nanosheets PL measurements were performed under different excitation wavelengths. All PL spectra in Figure 6.8 highlight the significant quenching in both downconversion and upconversion emission intensity after exfoliation. Under 532 nm laser excitation, the spectra of a single bulk microcrystal and a 6 ML nanosheet shown in Figure 6.8 (a,b) display emissions at 654 nm, 840 nm and 980 nm while the 1 ML nanosheet only displays an emission at 654 nm. The emissions at 654 nm and 840 nm can be attributed to the $^4F_{9/2} \rightarrow {}^4I_{15/2}$ and $^4S_{3/2} \rightarrow {}^4I_{13/2}$ transitions of $Er^{3+}$ respectively, while the emission at 980 nm arises from the $Er^{3+}$ $^4I_{11/2} \rightarrow {}^4I_{15/2}$ and $Yb^{3+}$ $^2F_{5/2} \rightarrow {}^2F_{7/2}$ transitions [183, 184]. Additionally, under

532 nm excitation the peak ratio of the 980 nm to 840 nm emissions is significantly reduced in the 6 ML nanosheet compared with that of the microcrystals, indicating that $Yb^{3+}$ ions are preferentially depleted during exfoliation. Under 785 nm excitation the strong emission at 980 nm by the microcrystal and 6 ML nanosheet in Figure 6.8 (c) is due to the 785 nm excitation mode closely matching the $Er^{3+}$ $^4I_{9/2} \rightarrow {}^4I_{15/2}$ energy level transition which allows non-radiative energy transfer to the $^4I_{11/2}$ level enabling the $Er^{3+}$ $^4I_{11/2} \rightarrow Yb^{3+}$ $^2F_{5/2}$ to $^2F_{5/2} \rightarrow {}^2F_{7/2}$ emission [77]. This energy pathway enables the 1 ML nanosheet at 785 nm excitation to display a broad emission centred at ~1000 nm in Figure 6.8 (c) which was absent under 532 nm excitation.

Overall these results indicate that $Yb^{3+}$ ions are heavily depleted in the nanosheets and that the 1 ML nanosheet contains a negligible amount of either $Er^{3+}$ or $Yb^{3+}$ ions, a result which is increasingly being recognised in thin 2D materials where the low dimensionality tends to suppress the doping of foreign species requiring new doping methods such as surface charge transfer doping [185, 186]. Using this method lanthanide upconverting molecular and supramolecular complexes could be attached to the surface of the 2D $NaYF_4$ to overcome this depletion [187, 188].

Accordingly, upconversion emission under 980 nm excitation was achieved only in the 6 ML nanosheets which display the characteristic green and red peaks via the energy transfer upconversion of $Yb^{3+} \rightarrow Er^{3+}$ transitions $(^2H_{11/2}, {}^4S_{3/2}) \rightarrow {}^4I_{15/2}$ and $^4F_{9/2} \rightarrow {}^4I_{15/2}$ respectively in Figure 6.8 (d) [3]. The 6 ML nanosheets have a two orders of magnitude lower intensity compared to the bulk microparticles Figure 6.8 (e). This severe quenching is the result of several factors which have been revealed including:

(i)     the exfoliated nanosheets preferentially transform into α-phase, which typically exhibits a luminescence efficiency one order of magnitude lower than that of the β-phase [48].

(ii)    The increase in the surface area of the nanosheets compared to the bulk increases the probability of energy loss at the surface.

(iii)   $Er^{3+}$ emitter and $Yb^{3+}$ sensitizer ions are present in lower concentrations in the nanosheets as a result of dopant depletion during the exfoliation process.
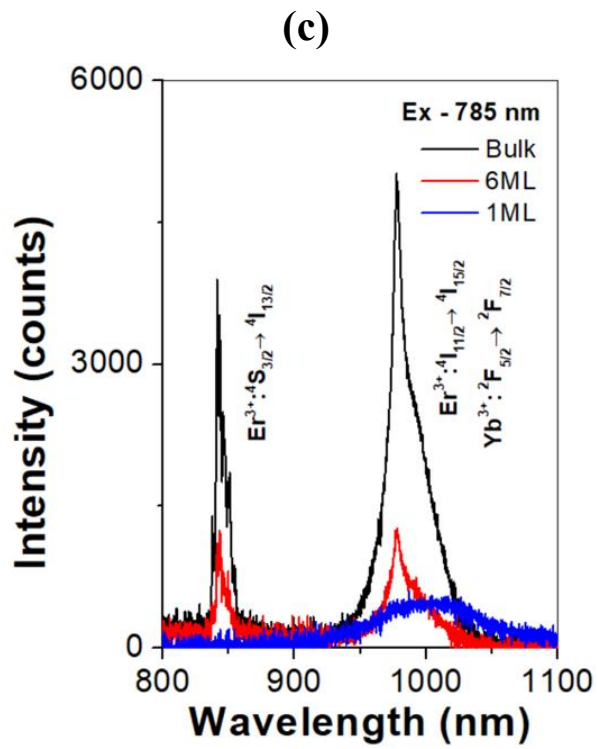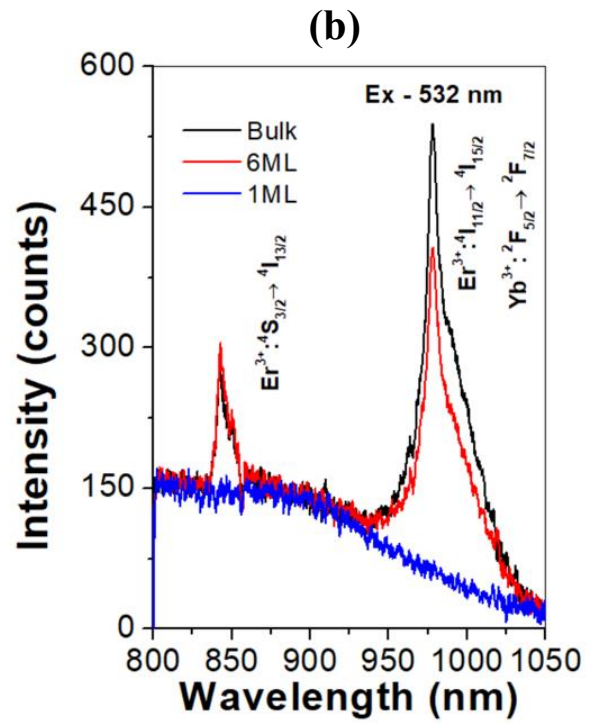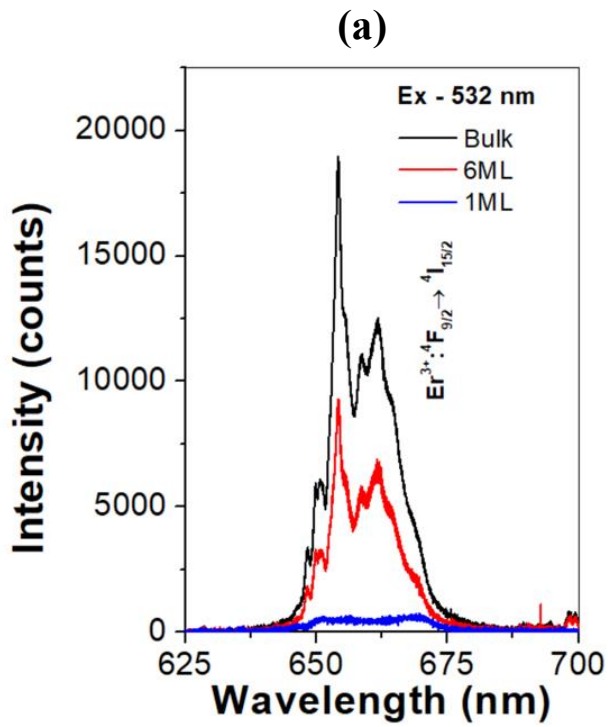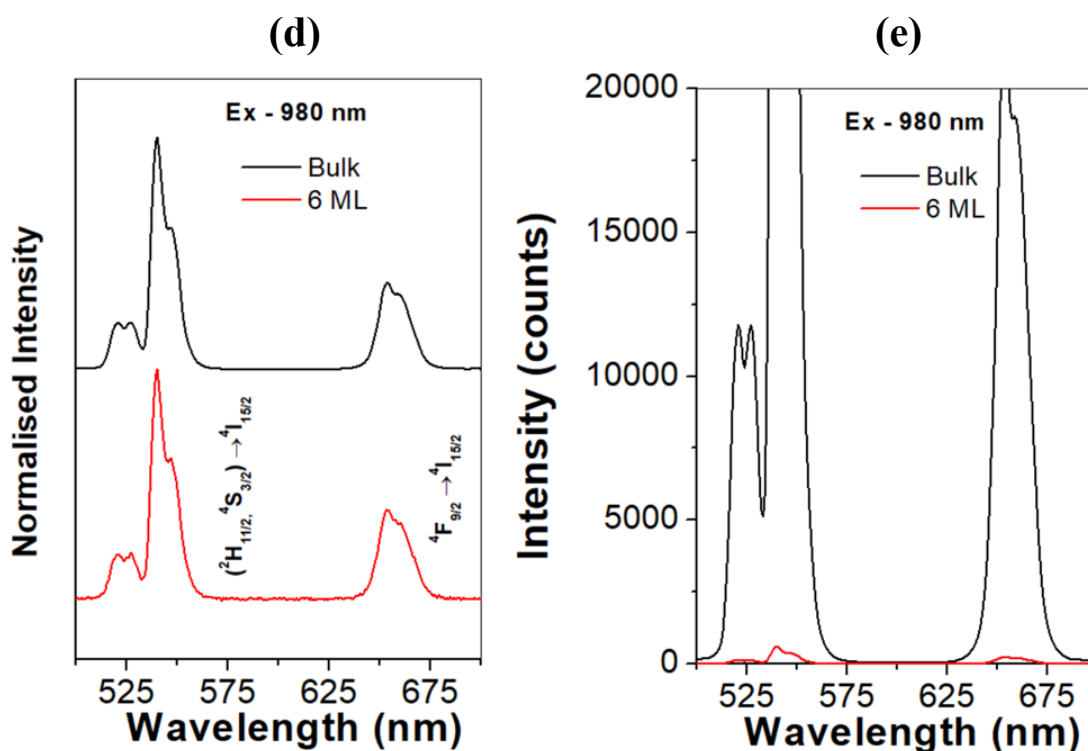
**Figure 6.8** Photoluminescence spectra of bulk and 2D NaYF$_4$: Yb$^{3+}$, Er$^{3+}$ nanosheets comprised of 1 and 6 monolayers under (a,b) 532 nm excitation, (c) 785 nm excitation and (d,e) 980 nm excitation respectively. PL spectra were acquired on same particles on which Raman studies were performed.

## 6.2.7 Electronic Structure

The electronic properties of this new 2D material were explored in-depth by Sherif Tawfik using DFT by first recalculating the partial density of states (PDOS) as displayed in Figure 6.9 (a). Compared to the PDOS of the bulk β-NaYF$_4$ crystal displayed in Figure 6.9 (b), there are several differences. The main difference is the introduction of a new state within the band gap region which is composed primarily of F 2p states. This state arises as a result of the introduction of a surface defect state which is attributed to the F atom shaded in Figure 6.6 (b). This state arises from the change in coordination of this surface F atom after the creation of the nanosheet. Specifically, the F atom relaxes along the c-axis while the two Na atoms in the second layer relax upwards. This results in the F atom bonding to three Na atoms and hence

changing its coordination. Secondly, the band gap of the 2D nanosheet (7.09 eV) is found to be smaller than that of the bulk (8.27 eV). This smaller band gap in the 2D than the bulk is an exception to other materials which typically display a larger band gap when restricted to the 2D [189]. This narrowing in the band gap can be explained by a mechanism known as decharge transfer which is triggered from the formation of the surface F atom defect and the accumulation of charge on the surface due to the distribution of dangling bonds after cleavage [173].

The DFT predicted reduced band gap when restricted to the 2D can be observed experimentally in the XPS maximum valence band energy spectra as shown in Figure 6.9 (c) which displays a 0.5 eV shift closer to the Fermi level for the 2D nanosheets compared to the bulk. As the DFT model does not include the presence of $Er^{3+}$ and $Yb^{3+}$ ions, the valence band onset peak is dominated by Yb 4f, instead of F 2p as indicated by the PDOS due to the spectral line of Yb 4f being of greater intensity than both the F 2p and Er 4f line [190, 191]. As the concentration of the $Yb^{3+}$ and especially $Er^{3+}$ ions are low ($Er^{3+}$ 3%, $Yb^{3+}$ 20%) they have been omitted from the DFT calculations due to the size of the model and hence the computational demand required to compute the low concentrations.

Additionally, the calculated shift in the conduction band edge is observable in the NEXAFS spectra of Na, Y, F, Er and Yb shown in Figure 6.9 (d-h) which display a specific shift from the bulk for only Y, Er and Yb. NEXAFS measurements are highly sensitive to the conduction band edge states and any shift in the position of the conduction band edge should be identifiable in the NEXAFS spectra of the dominating state [192]. For the PDOS of $NaYF_4$ in Figure 6.9 (a,b) the conduction band edge of both the bulk and 2D is completely dominated by the Y 4d state. This should explain the shift of the Y L-edge (a measurement of the 2p to 4d transition) and the shift of the Er and Yb $M_{4,5}$-edges (a measurement of the 3p to 4f transition) (due to the nature of doping in $NaYF_4$ the Y atom is substituted in the lattice for the lanthanide dopants being of similar ionic size and charge [49]. The shift in the NEXAFS spectra implies both the Er and Yb atoms would also contribute to the conduction band edge). However, the shift between the bulk and 2D $NaYF_4$: $Yb^{3+}$, $Er^{3+}$ nanosheets in the NEXAFS spectra is substantially smaller compared to the expected PDOS estimation and the direction seems to be inconsistent. DFT predicts a reduced band gap for the 2D nanosheets, however, the NEXAFS peaks shift to higher

photon energy suggesting an upward movement of conduction band edge or potentially increased band gap for the 2D nanosheets.

This is in part due to a limitation of the NEXAFS measurement. NEXAFS probes the electronic positions of a sample in an excited state with the position of the absorption edge representing the difference between the core level and conduction band state. Any shift in the NEXAFS spectra is due to shifts in unoccupied states and/or the corresponding core levels. However, it is assumed that core level binding energies are constant and that excitonic effects that can mask the edge are absent which may affect the position of the edges in each sample differently due to the differing material properties at differing information depths of the 2D and bulk $NaYF_4$: $Yb^{3+}$, $Er^{3+}$ samples [192]. Furthermore, the complete information about the conduction edge position is contained in a full set of NEXAFS spectra not in individual element specific spectra. Even if certain elements have a large contribution to the conduction band edge such as Y in the case of 2D $NaYF_4$, the position of the absorption edge can still be independent of stoichiometry. According to this idea there is a local electronic environment around each atom which can be independent of stoichiometry with the optically measurable band gap of the material only becoming evident at macroscopic levels. Therefore, assigning shifts in the positions of the absorption edges to local electronic structure with certainty is not reliable.

Apart from this limit in the NEXAFS measurement influences effecting the position of the edge from effects such as charge transfer and structural changes in the interlayer spacing, in-plane bond length and bond strength from the bulk to the 2D are also responsible for the shift [193]. Additionally, absorbed gas molecules bound to the surface of the nanosheet from the ambient atmosphere before ultrahigh vacuum can shift the conduction band [194, 195]. Due to these reasons and the inability to measure the optical band gap of 2D $NaYF_4$ without using a high energy UV synchrotron source [52] the NEXAFS measurements are supplementary to the XPS valence spectra for identifying shrinkage in the band gap. Regardless, the NEXAFS spectra of Yb and Er confirm the presence of the doping ions in the exfoliated nanosheets and the identical NEXAFS profiles before and after exfoliation indicate that the Yb and Er dopants remain in substitutional Y sites of the $NaYF_4$ lattice with a 3+ valence state [3].

**(a)**
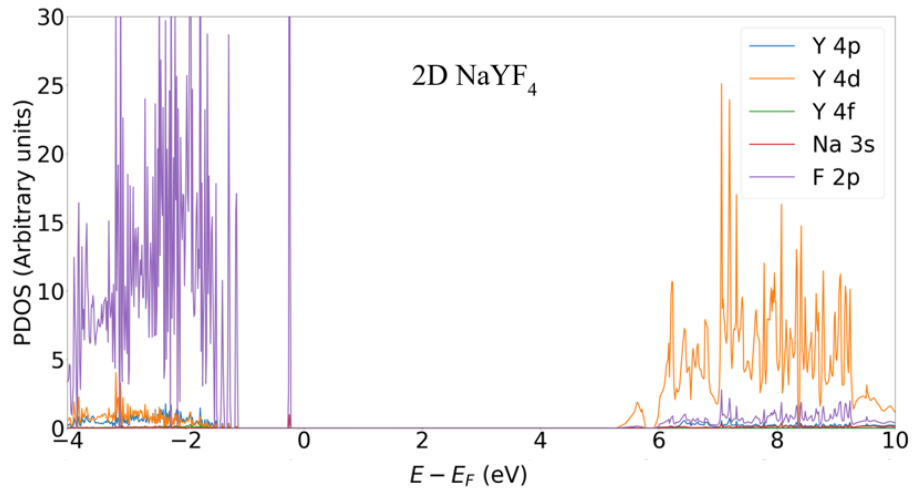


**(b)**
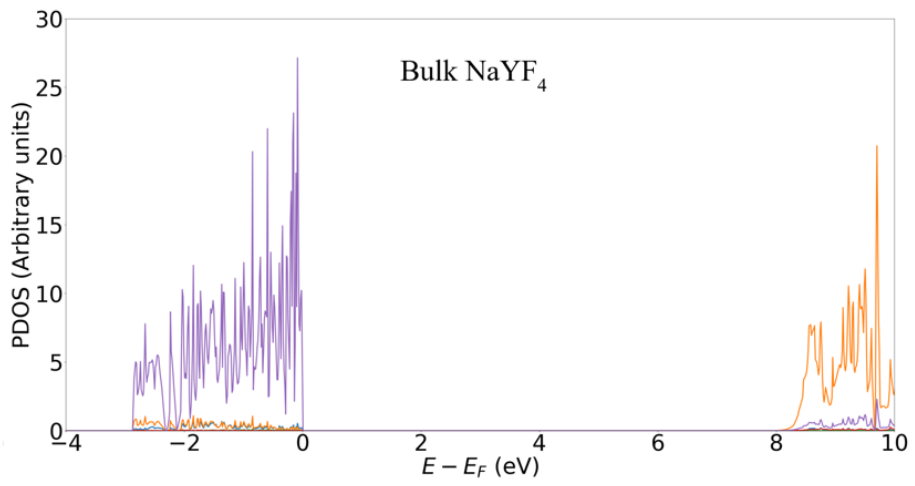


**(c)**
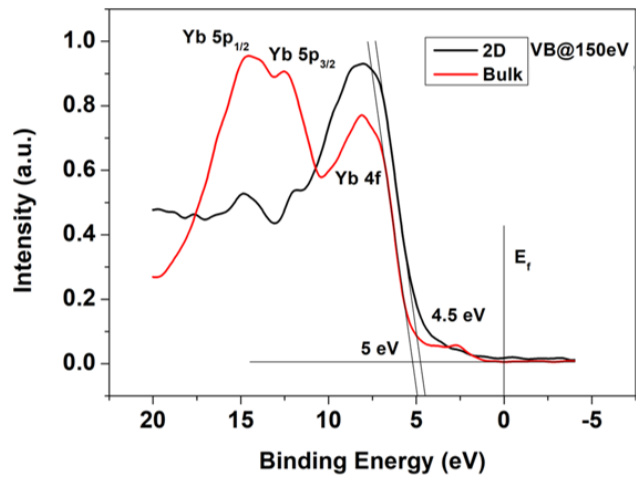
**(d)**
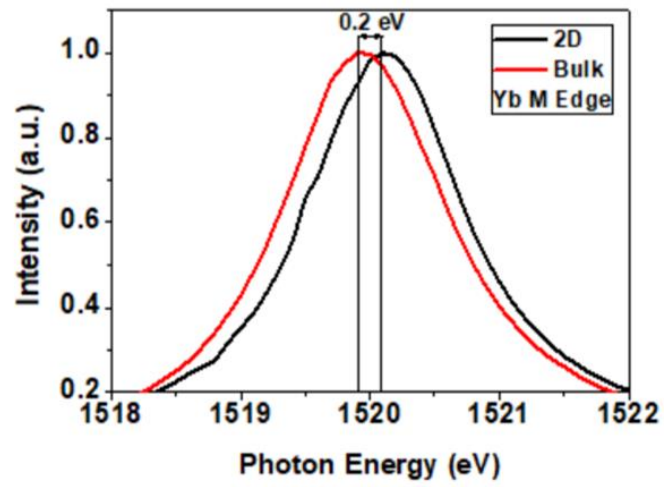


**(e)**
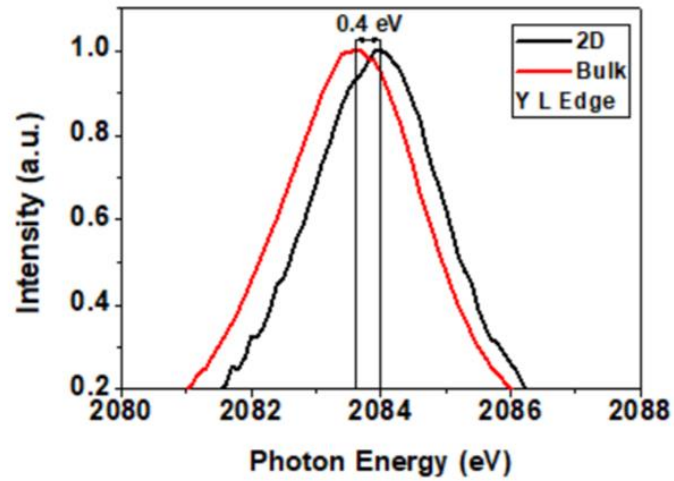


**(f)**
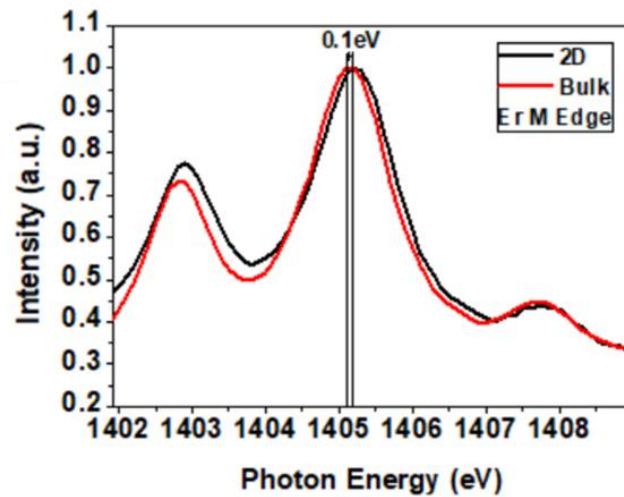
**(g)**
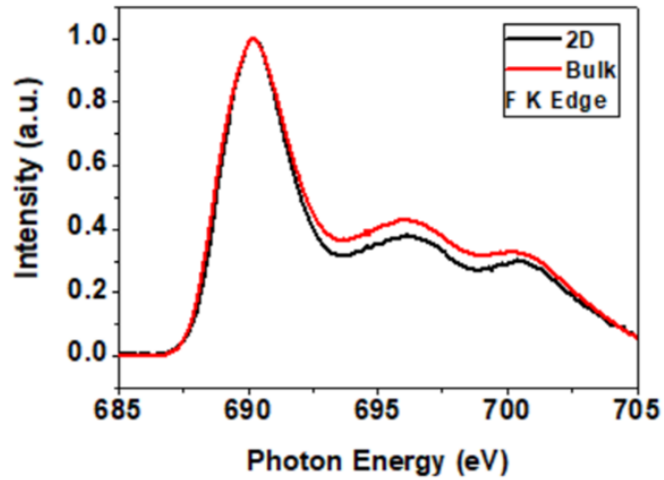


**(h)**
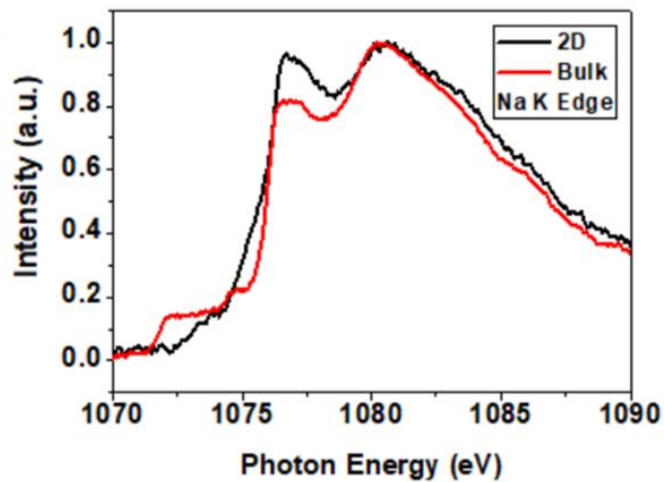


**Figure 6.9** Partial density of states for one monolayer and bulk β-NaYF$_4$, showing new empty electronic states close to the conduction band minimum, which leads to band gap narrowing (a,b). A defect level at 0.2 eV below the Fermi level is found, arising from the relaxation of the F atom shown in Figure 6.6 (b). Valence band spectra of NaYF$_4$: Yb$^{3+}$, Er$^{3+}$ nanosheets and bulk acquired at hν = 150 eV, which shows a shift of the valence band onset by 0.5 eV (c). NEXAFS spectra of NaYF$_4$: Yb$^{3+}$, Er$^{3+}$ nanosheets and bulk of the Yb M-edge, Y L-edge, Er M-edge, F K-edge and Na K-edge, showing a peak shift of 0.2, 0.4 eV and 0.1 eV for Yb, Y and Er respectively (d-h).

# 6.3    Summary

The exfoliated 2D NaYF$_4$: Yb$^{3+}$, Er$^{3+}$ nanosheets have a thickness of a few atomic layers, with a predominantly (100) surface orientation. Photoluminescence studies of the nanosheets show they are optically active and exhibit optical downconversion and upconversion properties similar to those of the parent microparticles prior to exfoliation, albeit with reduced intensity. Microscopic and Raman analysis reveals the non-trivial transition of β-phase in the bulk crystals to α-phase in the monolayer NaYF$_4$. Further exploration of their electronic structure by Density Functional Theory and photoelectron spectroscopy reveals the defect and charge transfer occurring in nanosheets, which diminishes the band gap by more than 1 eV. These findings will trigger further interest in 2D upconversion nanomaterials.

# Chapter 7

# Conclusions and Outlook

## 7.1 Conclusion

Overall the aims of the project have been achieved. This thesis firstly systematically investigated the distribution of the sensitizer $Yb^{3+}$ ions within $NaYF_4$ UCNPs. The up to 10 nm depth resolved XPS and EDS mapping revealed a gradient distribution of $Yb^{3+}$ in ratio to $Y^{3+}$ from the centre to the surface of the UCNPs by a factor of less than 0.01 to greater than 0.75. This distribution for each UCNP was the same regardless of the size or $Yb^{3+}$ doping concentration. The heterogeneous distribution pattern promotes increased emission efficiency in smaller UCNPs with a higher proportion of $Yb^{3+}$ sensitizer ions found in the core that avoid surface quenching effects.

Secondly, the novel combination of CS UCNP synthesis and Au dewetting was explored to produce Au-CS UCNPs that exhibit optimised plasmonic enhanced single particle upconversion emission. This integrated method achieving a 5.5 times enhanced upconversion emission is due to emission plasmonic coupling occurring from the overlap between the LSPR of the Au nanoparticles and the emission of the $Er^{3+}$ ions. The design and large-scale integrated method for the fabrication of these Au-CS UCNPs represents a new direction in research for plasmonic enhancement of upconversion emission.

Finally, the 2D $NaYF_4$ work provides the first experimental evidence of atomically-thin upconversion nanosheets of $NaYF_4$:Yb,Er via liquid phase cleaving bulk crystal along the (100) plane. A non-trivial phase transition from the β-phase in the bulk crystals to α-phase in the monolayer $NaYF_4$ and a significant narrowing of the band gap, as evident from both theoretical calculations (reduced by 1.18 eV) and

synchrotron analysis techniques (reduced by 0.5 eV) is observed in this new 2D material.

The understanding gained from this thesis gives a clearer idea about how and why issues like concentration quenching and quantum yield limit the optical properties of UCNPs. Fundamentally concentration quenching is a sign of the limit in the ability to control the distribution of the lanthanide ions within the nanocrystal. The XPS/NEXAFS/EDS studies of the sensitizer ions location and distribution patterns in a variety of UCNPs with different size and/or doping concentrations contributes to solving the concentration quenching issue further demonstrating methods that allow measurement of this distribution. The quantum yield limit is intrinsic to lanthanide ions and the enhancement methods explored in this thesis such as the surface plasmonic coupling enhancement to improve emission efficiency are mandatory for overcoming this limit.

# 7.2 Outlook

Further lanthanide distribution studies are required to investigate the nucleation thermodynamics and kinetics for a wider range of $NaYF_4$ UCNPs including that of core shell UCNPs as recent studies have further demonstrated similar gradients exists in core shell UCNPs [196]. Investigations should focus on the epitaxial growth of different shells with different compositions to precisely control dopant distributions across single UCNPs allowing for greater control of spatial arrangements of sensitizers and activators. The research presented in this thesis indicates that the assumption of uniform lanthanide distribution across the nanocrystal host is incorrect. Lanthanide ions doped within the $NaYF_4$ host are not uniformly distributed but distributed in a radial pattern, which affects the energy transfer between the sensitizers and emitters. The XPS/NEXAFS/EDS investigations on UCNPs at the atomic scale further implies that future research will have to conduct similar studies to confirm and enable the fine tuning of doping for highly efficient UCNPs.

Although the plasmon coupling approach studied in this thesis is restricted to the substrate it still has practical application. One of the most ideal applications would be

its use in enhancing the efficiency of solar cells. This could be achieved by introducing a layer of these Au-CS UCNPs into the assembly of a solar cell, allowing it to upconvert and absorb solar radiation outside of the sensitive range of the cell.

Primarily the synthesis of the new 2D $NaYF_4$ material within this thesis represents a new and exciting avenue for research possibility expanding the degree of control in the morphology of $NaYF_4$. The ability to produce 2D $NaYF_4$ represents a new class of 2D upconversion materials is possible opening pathways for a wider range of non-van Waal 2D materials [197, 198]. Although at this current stage the optical emission intensities are reduced significantly further studies will be required on this material to optimise its properties and commonly used enhancement methods to improve performance of $NaYF_4$ UCNPs can be ported and adapted for 2D $NaYF_4$. Future studies to increase the efficiency and brightness of the 2D $NaYF_4$ could investigate exfoliating highly doped bulk material for producing sandwich layers of high and low lanthanide concentrations for better control over the energy migration between lanthanide ions. Additionally, surface quenching could be minimised by sandwiching the optically active 2D $NaYF_4$ with inert nanosheets of $NaYF_4$ devoid of lanthanide dopants. Combining 2D $NaYF_4$ and the gold dewetting method developed in this thesis is another enhancement strategy that could allow for greater upconversion emission from the 2D $NaYF_4$. By forming gold nanoparticles directly onto the surface of 2D $NaYF_4$ nanosheets the plasmon produced at the interface of the nanosheet and gold nanoparticle could result in a greatly enhanced emission from the lanthanide ions in the nanosheet.

Concurrently research on the application of 2D $NaYF_4$ is recommended. The large surface area of this material leads itself towards surface functionalisation with biomolecules and dyes for use in photovoltaics and bioassays. Enhanced 2D $NaYF_4$ could be surface functionalised for binding to cancer cells. Essentially wrapping the cell in a net of the 2D $NaYF_4$ which, upon excitation, would act as a form of specific photothermal therapy. The unique electronic properties of 2D $NaYF_4$ can also be combined with other existing 2D materials like $WS_2$ and h-BN for optoelectronic device fabrication. Finally, the method used to produce this new class of 2D material opens up the possibility for further material development potentially to produce new classes of 2D quantum dots [199].

# Appendix

## Phononic Enhancement of UCNPs for Anti-Counterfeiting

DFT modelling of surface phonon vibrational stretches produced from OA bonded to Y and Yb predicted oxygen chelating with $Yb^{3+}$ ions (Yb-O) could greatly enhance upconversion emission at high temperatures in $Tm^{3+}$ doped $NaYF_4$ UCNPs. The role of the surface (Yb-O) phonons in this mechanism is to form new sensitizer – activator pairs with underutilized $Tm^{3+}$ ions at the surface of the UCNP at high temperature [2].

Experimental emission results recorded enormous enhancement at elevated temperatures as new more efficient Yb-O upconversion channels transferred energy to $Tm^{3+}$ activator ions. This enhancement relies on an active core UCNP structure which matches with the experimentally determined lanthanide distribution within UCNPs. The three orders of magnitude enhancement gained in the ultra-small 9 nm $Tm^{3+}$ doped UCNPs named thermal dots was significant and practical for use in an anti-counterfeiting application as a new type of temperature responsive security ink.

A modified HP Deskjet 3632 inkjet printer shown in Figure A.1 (a) was used to print the UCNP inks. Using the original black ink cartridges for the printer and removing the ink plus the filter within, the print head of the cartridge as highlighted in Figure A.1 (b) could be directly accessed for printing UCNPs. The $NaYF_4$: $Yb^{3+}/Tm^{3+}$ thermal dots and conventional $NaYF_4$: $Yb^{3+}/Er^{3+}$ UCNPs were prepared in cyclohexane at concentrations of 12 mg/mL and 3 mg/mL respectively for printing. Prior to printing the solutions were sonicated for 10 minutes. The UCNP inks were repeatedly printed up to 40 times onto white A4 paper with each UCNP ink being separately printed through a separate black ink cartridge. Printed designs such as those shown in Figure A.1 (c) were excited under external 980 nm laser excitation at a power density of 0.7 $W/cm^2$ and imaged via a table mounted Canon EOS 70D camera with a macro lens and an 842 nm short pass filter attached to filter the excitation laser out of the image. Images were taken using an exposure time of 60 seconds at room

temperature and 453 K by using a copper holder. The copper holder used for its high thermal conductivity and even heat distribution was mounted on an XYZ stage to ensure the appropriate position. The temperature of the sample was controlled by a heating system assembled with a metal ceramic heater (HT24S2, Thorlabs) and a heater controller (TC200-EC, Thorlabs). This optical set-up as pictured in Figure A.2 (a) was used to recover the covert information of the concealed designs.
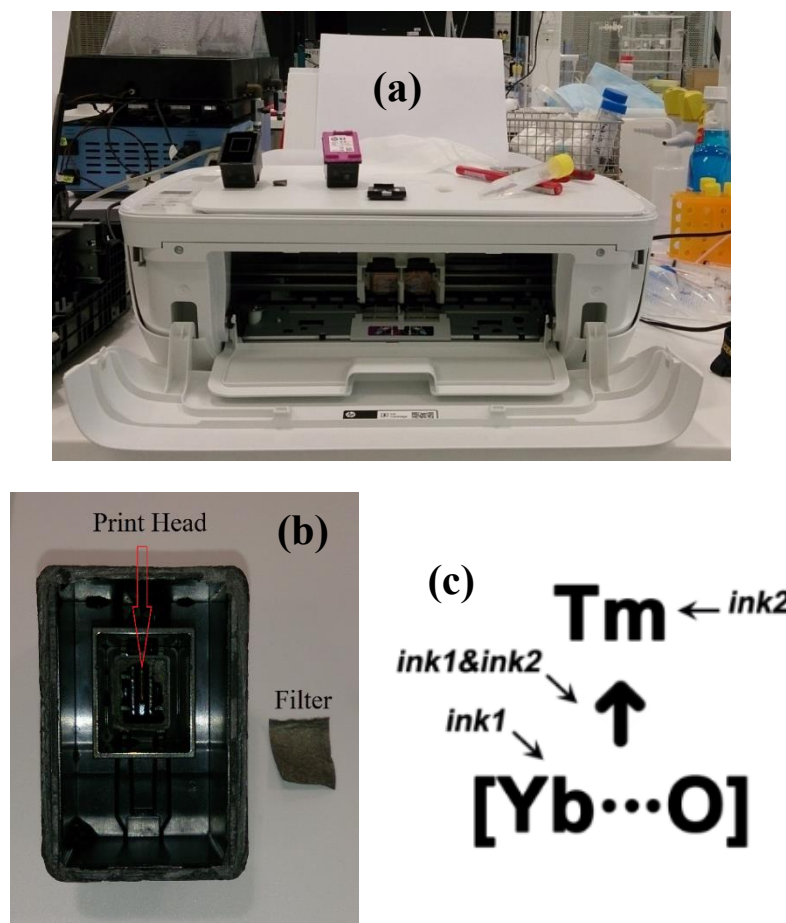


**Figure A.1** HP Deskjet 3632 inkjet printer (a), HP Deskjet 3632 black ink cartridge internal structure with filter removed (ink removed) (b) and printed design pattern (c).

The exceptional luminescence enhancement at high temperature provides a new type of security ink responsive to temperature change. Figure A.2 (b,c) illustrates the covert designs printed on white paper by the inkjet printer using the 9.7 nm thermal dots and conventional 25 nm NaYF$_4$: 20% Yb$^{3+}$, 2% Er$^{3+}$ UCNPs. Under normal white light conditions, the printed patterns are indistinguishable from plain blank white paper however, when increasing the temperature from room temperature to 453

K and applying 980 nm laser excitation, a blue 'Tm' clearly appears against a decreased green '[Yb···O]' and a whitish green arrow '↑' printed with both inks highlighting the mixed enhanced blue upconversion emission and diminished green emission. Similarly, the UTS logo in Figure A.2 (d) reads initially only the letters 'UTS' in green at room temperature having been only printed with the conventional NaYF$_4$: 20% Yb$^{3+}$, 2% Er$^{3+}$ UCNPs however at 453 K the other half of the logo the 'crest' symbol in blue appears overlapping and alongside the UTS characters having been printed with the thermal dots.

An additional level of coincidental security is built into these thermal dots whereby emission enhancement is diminished for all subsequent elevated temperature cycles. This means that an intended recipient could perform their own temperature cycle and easily identify if the concealed information had been compromised due to the pronounced visible reduction in emission enhancement from the thermal dots at high temperature.
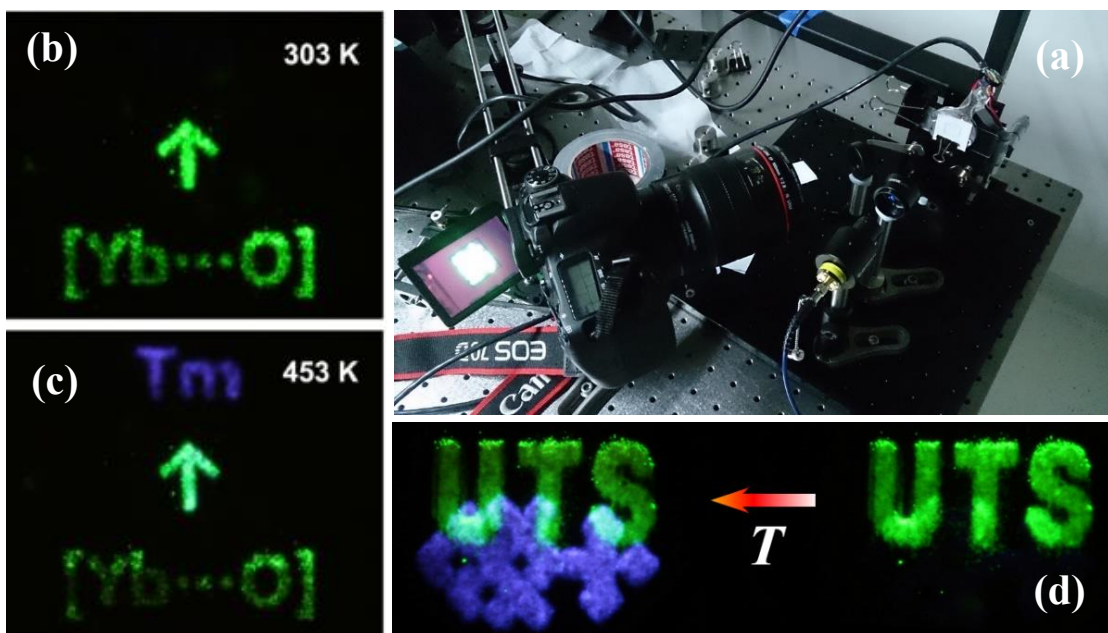


**Figure A.2** Optical set-up for imaging (a) and images of 1 cm × 1 cm temperature-responsive anti-counterfeiting security ink printed designs under continuous wave 0.7 W/cm$^2$ 980 nm laser excitation at 303 K (b), 453 K (c) and 303 K to 453 K (d).

This phononic enhancement cohesively confirms that the internal dopant distribution greatly influences the essential role of the nanoscale surface in accessing underutilised inactive sensitizer ions and activators. The strategy not only provides a powerful solution for turning on more efficient energy pathways of ultra-small UCNPs, but also suggests a new research direction to build highly efficient upconversion systems for practical applications such as this proof of concept anti-counterfeiting security ink.

This phononic enhancement work relying on a highly concentrated active core was successfully demonstrated in use as an anti-counterfeiting security ink displaying an upconverted blue emission enhancement of ~2,000 fold for 9.7 nm $Yb^{3+}$/$Tm^{3+}$ co-doped $NaYF_4$ thermal dots at 453 K. Further comprehensive characterisation and applications are necessary to gain more insights into the phononic enhancement phenomena observed. This enhancement in which the surface-area-to-volume ratio plays an essential role is particularly useful for ultra-small UCNPs. The enhanced brightness at high temperature allows for a variety of applications other than anti-counterfeiting with opportunities in elevated temperature sensing and optoelectronics.

# References

1.  Xu, X., C. Clarke, C. Ma, G. Casillas, M. Das, M. Guan, D. Liu, L. Wang, A. Tadich, and Y. Du, *Depth-profiling of Yb 3+ sensitizer ions in NaYF 4 upconversion nanoparticles.* Nanoscale, 2017. **9**(23): p. 7719-7726.

2.  Zhou, J., S. Wen, J. Liao, C. Clarke, S.A. Tawfik, W. Ren, C. Mi, F. Wang, and D. Jin, *Activation of the surface dark-layer to enhance upconversion in a thermal field.* Nature Photonics, 2018. **12**(3): p. 154.

3.  Clarke, C., D. Liu, F. Wang, Y. Liu, C. Chen, C. Ton-That, X. Xu, and D. Jin, *Large-scale dewetting assembly of gold nanoparticles for plasmonic enhanced upconversion nanoparticles.* Nanoscale, 2018. **10**(14): p. 6270-6276.

4.  Ren, W., G. Lin, C. Clarke, J. Zhou, and D. Jin, *Optical Nanomaterials and Enabling Technologies for High-Security-Level Anticounterfeiting.* Advanced Materials, 2019: p. 1901430.

5.  Du, Z., A. Gupta, C. Clarke, M. Cappadona, D. Clases, D. Liu, Z. Yang, P. Doble, W. Price, and X. Xu, *Porous upconversion nanostructures as bimodal biomedical imaging contrast agents.* bioRxiv, 2019: p. 837864.

6.  Nasiri, N. and C. Clarke, *Nanostructured chemiresistive gas sensors for medical applications.* Sensors, 2019. **19**(3): p. 462.

7.  Nasiri, N. and C. Clarke, *Nanostructured Gas Sensors for Medical and Health Applications: Low to High Dimensional Materials.* Biosensors, 2019. **9**(1): p. 43.

8.  Auzel, F., *Upconversion and anti-stokes processes with f and d ions in solids.* Chemical reviews, 2004. **104**(1): p. 139-174.

9.  Gai, S., C. Li, P. Yang, and J. Lin, *Recent progress in rare earth micro/nanocrystals: soft chemical synthesis, luminescent properties, and biomedical applications.* Chemical reviews, 2013. **114**(4): p. 2343-2389.

10. Zhou, B., B. Shi, D. Jin, and X. Liu, *Controlling upconversion nanocrystals for emerging applications.* Nature nanotechnology, 2015. **10**(11): p. 924.

11. Chen, G., H. Qiu, P.N. Prasad, and X. Chen, *Upconversion nanoparticles: design, nanochemistry, and applications in theranostics.* Chemical reviews, 2014. **114**(10): p. 5161-5214.

12. Mahata, M.K., H.C. Hofsäss, and U. Vetter, *Photon-upconverting materials: advances and prospects for various emerging applications*, in *Luminescence-An Outlook on the Phenomena and their Applications*. 2016, InTech.

13. Zhang, F., *Photon upconversion nanomaterials*. Vol. 416. 2015: Springer.

14. Seddon, A.B., Z. Tang, D. Furniss, S. Sujecki, and T.M. Benson, *Progress in rare-earth-doped mid-infrared fiber lasers.* Optics express, 2010. **18**(25): p. 26704-26719.

15. Zhou, P., X. Wang, Y. Ma, H. Lü, and Z. Liu, *Review on recent progress on mid-infrared fiber lasers.* Laser Physics, 2012. **22**(11): p. 1744-1751.

16. Naccache, R., Q. Yu, and J.A. Capobianco, *The Fluoride Host: Nucleation, Growth, and Upconversion of Lanthanide-Doped Nanoparticles.* Advanced Optical Materials, 2015. **3**(4): p. 482-509.

17. Chen, C., C. Li, and Z. Shi, *Current Advances in Lanthanide-Doped Upconversion Nanostructures for Detection and Bioapplication.* Advanced Science, 2016. **3**(10): p. 1600029.

18. Güdel, H.U. and M. Pollnau, *Near-infrared to visible photon upconversion processes in lanthanide doped chloride, bromide and iodide lattices.* Journal of alloys and compounds, 2000. **303**: p. 307-315.

19. Liu, X., X. Kong, Y. Zhang, L. Tu, Y. Wang, Q. Zeng, C. Li, Z. Shi, and H. Zhang, *Breakthrough in concentration quenching threshold of upconversion luminescence via spatial separation of the emitter doping area for bio-applications.* Chemical Communications, 2011. **47**(43): p. 11957-11959.

20. Krämer, K.W., D. Biner, G. Frei, H.U. Güdel, M.P. Hehlen, and S.R. Lüthi, *Hexagonal sodium yttrium fluoride based green and blue emitting upconversion phosphors.* Chemistry of Materials, 2004. **16**(7): p. 1244-1251.

21. Boyer, J.-C. and F.C. Van Veggel, *Absolute quantum yield measurements of colloidal NaYF 4: Er3+, Yb3+ upconverting nanoparticles.* Nanoscale, 2010. **2**(8): p. 1417-1419.

22. Suter, J.D., N.J. Pekas, M.T. Berry, and P.S. May, *Real-time-monitoring of the synthesis of β-NaYF4: 17% Yb, 3% Er nanocrystals using NIR-to-visible upconversion luminescence.* The Journal of Physical Chemistry C, 2014. **118**(24): p. 13238-13247.

23. Ma, C., X. Xu, F. Wang, Z. Zhou, D. Liu, J. Zhao, M. Guan, C.I. Lang, and D. Jin, *Optimal sensitizer concentration in single upconversion nanocrystals.* Nano letters, 2017. **17**(5): p. 2858-2864.

24. Chen, X., L. Jin, W. Kong, T. Sun, W. Zhang, X. Liu, J. Fan, S.F. Yu, and F. Wang, *Confining energy migration in upconversion nanoparticles towards deep ultraviolet lasing.* Nature communications, 2016. **7**: p. 10304.

25. Chen, B., Y. Liu, Y. Xiao, X. Chen, Y. Li, M. Li, X. Qiao, X. Fan, and F. Wang, *Amplifying excitation-power sensitivity of photon upconversion in a NaYbF4: Ho nanostructure for direct visualization of electromagnetic hotspots.* The journal of physical chemistry letters, 2016. **7**(23): p. 4916-4921.

26. Shen, B., S. Cheng, Y. Gu, D. Ni, Y. Gao, Q. Su, W. Feng, and F. Li, *Revisiting the optimized doping ratio in core/shell nanostructured upconversion particles.* Nanoscale, 2017. **9**(5): p. 1964-1971.

27. Zhao, J., D. Jin, E.P. Schartner, Y. Lu, Y. Liu, A.V. Zvyagin, L. Zhang, J.M. Dawes, P. Xi, and J.A. Piper, *Single-nanocrystal sensitivity achieved by enhanced upconversion luminescence.* Nature nanotechnology, 2013. **8**(10): p. 729.

28. Gargas, D.J., E.M. Chan, A.D. Ostrowski, S. Aloni, M.V.P. Altoe, E.S. Barnard, B. Sanii, J.J. Urban, D.J. Milliron, and B.E. Cohen, *Engineering*

*bright sub-10-nm upconverting nanocrystals for single-molecule imaging.* Nature nanotechnology, 2014. **9**(4): p. 300.

29.     Nyk, M., R. Kumar, T.Y. Ohulchanskyy, E.J. Bergey, and P.N. Prasad, *High contrast in vitro and in vivo photoluminescence bioimaging using near infrared to near infrared up-conversion in Tm3+ and Yb3+ doped fluoride nanophosphors.* Nano letters, 2008. **8**(11): p. 3834-3838.

30.     Cheng, L., K. Yang, Y. Li, X. Zeng, M. Shao, S.-T. Lee, and Z. Liu, *Multifunctional nanoparticles for upconversion luminescence/MR multimodal imaging and magnetically targeted photothermal therapy.* Biomaterials, 2012. **33**(7): p. 2215-2222.

31.     Park, Y.I., J.H. Kim, K.T. Lee, K.S. Jeon, H.B. Na, J.H. Yu, H.M. Kim, N. Lee, S.H. Choi, and S.I. Baik, *Nonblinking and nonbleaching upconverting nanoparticles as an optical imaging nanoprobe and T1 magnetic resonance imaging contrast agent.* Advanced Materials, 2009. **21**(44): p. 4467-4471.

32.     Wu, S., G. Han, D.J. Milliron, S. Aloni, V. Altoe, D.V. Talapin, B.E. Cohen, and P.J. Schuck, *Non-blinking and photostable upconverted luminescence from single lanthanide-doped nanocrystals.* Proceedings of the National Academy of Sciences, 2009. **106**(27): p. 10917-10921.

33.     Wang, L., R. Yan, Z. Huo, L. Wang, J. Zeng, J. Bao, X. Wang, Q. Peng, and Y. Li, *Fluorescence resonant energy transfer biosensor based on upconversion-luminescent nanoparticles.* Angewandte Chemie International Edition, 2005. **44**(37): p. 6054-6057.

34.     He, H., C.B. Howard, Y. Chen, S. Wen, G. Lin, J. Zhou, K.J. Thurecht, and D. Jin, *Bispecific antibody-functionalized upconversion nanoprobe.* Analytical chemistry, 2018. **90**(5): p. 3024-3029.

35.     Chen, Y., H.T. Duong, S. Wen, C. Mi, Y. Zhou, O. Shimoni, S.M. Valenzuela, and D. Jin, *Exonuclease III-Assisted Upconversion Resonance Energy Transfer in a Wash-Free Suspension DNA Assay.* Analytical chemistry, 2017. **90**(1): p. 663-668.

36.    Wang, C., L. Cheng, and Z. Liu, *Drug delivery with upconversion nanoparticles for multi-functional targeted cancer cell imaging and therapy.* Biomaterials, 2011. **32**(4): p. 1110-1120.

37.    Tian, G., Z. Gu, L. Zhou, W. Yin, X. Liu, L. Yan, S. Jin, W. Ren, G. Xing, and S. Li, *Mn2+ dopant-controlled synthesis of NaYF4: Yb/Er upconversion nanoparticles for in vivo imaging and drug delivery.* Advanced Materials, 2012. **24**(9): p. 1226-1231.

38.    Idris, N.M., M.K. Gnanasammandhan, J. Zhang, P.C. Ho, R. Mahendran, and Y. Zhang, *In vivo photodynamic therapy using upconversion nanoparticles as remote-controlled nanotransducers.* Nature medicine, 2012. **18**(10): p. 1580.

39.    Lu, Y., J. Zhao, R. Zhang, Y. Liu, D. Liu, E.M. Goldys, X. Yang, P. Xi, A. Sunna, and J. Lu, *Tunable lifetime multiplexing using luminescent nanocrystals.* Nature Photonics, 2014. **8**(1): p. 32.

40.    Goldschmidt, J.C. and S. Fischer, *Upconversion for photovoltaics–a review of materials, devices and concepts for performance enhancement.* Advanced Optical Materials, 2015. **3**(4): p. 510-535.

41.    Wang, F., Y. Han, C.S. Lim, Y. Lu, J. Wang, J. Xu, H. Chen, C. Zhang, M. Hong, and X. Liu, *Simultaneous phase and size control of upconversion nanocrystals through lanthanide doping.* nature, 2010. **463**(7284): p. 1061.

42.    Deng, R., F. Qin, R. Chen, W. Huang, M. Hong, and X. Liu, *Temporal full-colour tuning through non-steady-state upconversion.* Nature nanotechnology, 2015. **10**(3): p. 237.

43.    Chen, C., F. Wang, S. Wen, Q.P. Su, M.C. Wu, Y. Liu, B. Wang, D. Li, X. Shan, and M. Kianinia, *Multi-photon near-infrared emission saturation nanoscopy using upconversion nanoparticles.* Nature communications, 2018. **9**(1): p. 3290.

44.    Liu, Y., Y. Lu, X. Yang, X. Zheng, S. Wen, F. Wang, X. Vidal, J. Zhao, D. Liu, and Z. Zhou, *Amplified stimulated emission in upconversion*

*nanoparticles for super-resolution nanoscopy.* Nature, 2017. **543**(7644): p. 229.

45.     Pokhrel, M., A. kumar Gangadharan, and D.K. Sardar, *High upconversion quantum yield at low pump threshold in Er3+/Yb3+ doped La2O2S phosphor.* Materials Letters, 2013. **99**: p. 86-89.

46.     Han, S., R. Deng, X. Xie, and X. Liu, *Enhancing luminescence in lanthanide-doped upconversion nanoparticles.* Angewandte Chemie International Edition, 2014. **53**(44): p. 11702-11715.

47.     Shannon, R.D., *Revised effective ionic radii and systematic studies of interatomic distances in halides and chalcogenides.* Acta crystallographica section A: crystal physics, diffraction, theoretical and general crystallography, 1976. **32**(5): p. 751-767.

48.     Wang, L., X. Li, Z. Li, W. Chu, R. Li, K. Lin, H. Qian, Y. Wang, C. Wu, and J. Li, *A new cubic phase for a NaYF4 host matrix offering high upconversion luminescence efficiency.* Advanced Materials, 2015. **27**(37): p. 5528-5533.

49.     Mackenzie, L.E., J.A. Goode, A. Vakurov, P.P. Nampi, S. Saha, G. Jose, and P.A. Millner, *The theoretical molecular weight of NaYF 4: RE upconversion nanoparticles.* Scientific reports, 2018. **8**(1): p. 1106.

50.     Klier, D.T. and M.U. Kumke, *Analysing the effect of the crystal structure on upconversion luminescence in Yb 3+, Er 3+-co-doped NaYF 4 nanomaterials.* Journal of Materials Chemistry C, 2015. **3**(42): p. 11228-11238.

51.     Huang, B., H. Dong, K.-L. Wong, L.-D. Sun, and C.-H. Yan, *Fundamental view of electronic structures of β-NaYF4, β-NaGdF4, and β-NaLuF4.* The Journal of Physical Chemistry C, 2016. **120**(33): p. 18858-18870.

52.     Chong, K., T. Hirai, T. Kawai, S. Hashimoto, and N. Ohno, *Optical properties of Bi3+ ions doped in NaYF4.* Journal of luminescence, 2007. **122**: p. 149-151.

53. Fedorov, P., S. Kuznetsov, V. Voronov, I. Yarotskaya, and V. Arbenina, *Soft chemical synthesis of NaYF 4 nanopowders.* Russian Journal of Inorganic Chemistry, 2008. **53**(11): p. 1681-1685.

54. Sokolov, V., A. Zvyagin, S. Igumnov, S. Molchanova, M. Nazarov, A. Nechaev, A. Savelyev, A. Tyutyunov, E. Khaydukov, and V.Y. Panchenko, *Determination of the refractive index of β-NaYF 4/Yb 3+/Er 3+/Tm 3+ nanocrystals using spectroscopic refractometry.* Optics and Spectroscopy, 2015. **118**(4): p. 609-613.

55. Li, Z. and Y. Zhang, *An efficient and user-friendly method for the synthesis of hexagonal-phase NaYF(4):Yb, Er/Tm nanocrystals with controllable shape and upconversion fluorescence.* Nanotechnology, 2008. **19**(34): p. 345606.

56. Mai, H.-X., Y.-W. Zhang, R. Si, Z.-G. Yan, L.-d. Sun, L.-P. You, and C.-H. Yan, *High-quality sodium rare-earth fluoride nanocrystals: controlled synthesis and optical properties.* Journal of the American Chemical Society, 2006. **128**(19): p. 6426-6436.

57. Yao, W., Q. Tian, J. Liu, Z. Wu, S. Cui, J. Ding, Z. Dai, and W. Wu, *Large-scale synthesis and screen printing of upconversion hexagonal-phase NaYF4:Yb3+,Tm3+/Er3+/Eu3+ plates for security applications.* Journal of Materials Chemistry C, 2016. **4**(26): p. 6327-6335.

58. You, W., D. Tu, W. Zheng, X. Shang, X. Song, S. Zhou, Y. Liu, R. Li, and X. Chen, *Large-Scale Synthesis of Uniform Lanthanide-Doped NaREF4 Upconversion/Downshifting Nanoprobes for Bioapplications.* Nanoscale, 2018.

59. Ma, C., X. Xu, F. Wang, Z. Zhou, S. Wen, D. Liu, J. Fang, C.I. Lang, and D. Jin, *Probing the interior crystal quality in the development of more efficient and smaller upconversion nanoparticles.* The journal of physical chemistry letters, 2016. **7**(16): p. 3252-3258.

60. Mai, H.-X., Y.-W. Zhang, L.-D. Sun, and C.-H. Yan, *Highly efficient multicolor up-conversion emissions and their mechanisms of monodisperse*

*NaYF4: Yb, Er core and core/shell-structured nanocrystals.* The Journal of Physical Chemistry C, 2007. **111**(37): p. 13721-13729.

61.     Liu, X., X. Zhang, G. Tian, W. Yin, L. Yan, L. Ruan, Z. Yang, D. Xiao, and Z. Gu, *A simple and efficient synthetic route for preparation of NaYF 4 upconversion nanoparticles by thermo-decomposition of rare-earth oleates.* CrystEngComm, 2014. **16**(25): p. 5650-5661.

62.     Ostrowski, A.D., E.M. Chan, D.J. Gargas, E.M. Katz, G. Han, P.J. Schuck, D.J. Milliron, and B.E. Cohen, *Controlled synthesis and single-particle imaging of bright, sub-10 nm lanthanide-doped upconverting nanocrystals.* ACS nano, 2012. **6**(3): p. 2686-2692.

63.     Gee, A., *SURFACE MODIFICATION AND FUNCTIONALISATION OF UPCONVERSION NANOPARTICLES.* 2018, University of Technology Sydney.

64.     Zhai, X., Y. Wang, X. Liu, S. Liu, P. Lei, S. Yao, S. Song, L. Zhou, J. Feng, and H. Zhang, *A Simple Strategy for the Controlled Synthesis of Ultrasmall Hexagonal-Phase NaYF4: Yb, Er Upconversion Nanocrystals.* ChemPhotoChem, 2017. **1**(8): p. 369-375.

65.     Abel, K.A., J.-C. Boyer, and F.C.v. Veggel, *Hard proof of the NaYF4/NaGdF4 nanocrystal core/shell structure.* Journal of the American Chemical Society, 2009. **131**(41): p. 14644-14645.

66.     Li, X., R. Wang, F. Zhang, and D. Zhao, *Engineering homogeneous doping in single nanoparticle to enhance upconversion efficiency.* Nano letters, 2014. **14**(6): p. 3634-3639.

67.     Chen, H., Y. Lang, D. Zhao, C. He, and W. Qin, *Enhanced high-order upconversion luminescence of hexagonal phase NaYF4: Yb3+, Tm3+ crystals coated with homogeneous shell.* Journal of Fluorine Chemistry, 2015. **174**: p. 70-74.

68. Dong, C., J. Pichaandi, T. Regier, and F.C. van Veggel, *Nonstatistical dopant distribution of Ln3+-doped NaGdF4 nanoparticles.* The Journal of Physical Chemistry C, 2011. **115**(32): p. 15950-15958.

69. Abel, K.A., J.-C. Boyer, C.M. Andrei, and F.C. van Veggel, *Analysis of the shell thickness distribution on NaYF4/NaGdF4 core/shell nanocrystals by EELS and EDS.* The Journal of Physical Chemistry Letters, 2011. **2**(3): p. 185-189.

70. D hnen, S. and M. Haase, *Study on the intermixing of core and shell in NaEuF4/NaGdF4 core/shell nanocrystals.* Chemistry of Materials, 2015. **27**(24): p. 8375-8386.

71. Liu, D., X. Xu, Y. Du, X. Qin, Y. Zhang, C. Ma, S. Wen, W. Ren, E.M. Goldys, and J.A. Piper, *Three-dimensional controlled growth of monodisperse sub-50 nm heterogeneous nanocrystals.* Nature communications, 2016. **7**: p. 10254.

72. Bloembergen, N., *Solid state infrared quantum counters.* Physical Review Letters, 1959. **2**(3): p. 84.

73. Auzel, F. and O. Deutschbein, *Fluorescence anti-Stokes de l'Er3+ et du Tm3+ par transfert d'energie.* Zeitschrift für Naturforschung A, 1969. **24**(10): p. 1562-1568.

74. Ovsyakin, V. and P. Feofilov, *Cooperative sensitization of luminescence in crystals activated with rare earth ions.* Soviet Journal of Experimental and Theoretical Physics Letters, 1966. **4**: p. 317.

75. Zhang, W., S. Yang, J. Li, W. Gao, Y. Deng, W. Dong, C. Zhao, and G. Lu, *Visible-to-ultraviolet Upconvertion: Energy transfer, material matrix, and synthesis strategies.* Applied Catalysis B: Environmental, 2017. **206**: p. 89-103.

76. Wang, F. and X. Liu, *Recent advances in the chemistry of lanthanide-doped upconversion nanocrystals.* Chemical Society Reviews, 2009. **38**(4): p. 976-989.

77.     Chan, E.M., G. Han, J.D. Goldberg, D.J. Gargas, A.D. Ostrowski, P.J. Schuck, B.E. Cohen, and D.J. Milliron, *Combinatorial discovery of lanthanide-doped nanocrystals with spectrally pure upconverted emission.* Nano letters, 2012. **12**(7): p. 3839-3845.

78.     Carnall, W.T., *The absorption and fluorescence spectra of rare earth ions in solution.* Handbook on the physics and chemistry of rare earths, 1979. **3**: p. 171-208.

79.     Huang, P., W. Zheng, S. Zhou, D. Tu, Z. Chen, H. Zhu, R. Li, E. Ma, M. Huang, and X. Chen, *Lanthanide-Doped LiLuF4 Upconversion Nanoprobes for the Detection of Disease Biomarkers.* Angewandte Chemie International Edition, 2014. **53**(5): p. 1252-1257.

80.     Fischer, S., N.D. Bronstein, J.K. Swabeck, E.M. Chan, and A.P. Alivisatos, *Precise tuning of surface quenching for luminescence enhancement in core–shell lanthanide-doped nanocrystals.* Nano letters, 2016. **16**(11): p. 7241-7247.

81.     Assaaoudi, H., G.-B. Shan, N. Dyck, and G.P. Demopoulos, *Annealing-induced ultra-efficient NIR-to-VIS upconversion of nano-/micro-scale α and β NaYF4: Er 3+, Yb 3+ crystals.* CrystEngComm, 2013. **15**(23): p. 4739-4746.

82.     Dyck, N.C., F.C. van Veggel, and G.P. Demopoulos, *Size-dependent maximization of upconversion efficiency of citrate-stabilized β-phase NaYF4: Yb3+, Er3+ crystals via annealing.* ACS applied materials & interfaces, 2013. **5**(22): p. 11661-11667.

83.     Wang, H.-Q., R.D. Tilley, and T. Nann, *Size and shape evolution of upconverting nanoparticles using microwave assisted synthesis.* CrystEngComm, 2010. **12**(7): p. 1993-1996.

84.     Zhao, C., X. Kong, X. Liu, L. Tu, F. Wu, Y. Zhang, K. Liu, Q. Zeng, and H. Zhang, *Li+ ion doping: an approach for improving the crystallinity and upconversion emissions of NaYF4: Yb 3+, Tm 3+ nanoparticles.* Nanoscale, 2013. **5**(17): p. 8084-8089.

85. Fan, S., S. Wang, W. Xu, M. Li, H. Sun, and L. Hu, *Enormously enhanced upconversion emission in β-NaYF4: 20Yb, 2Er microcrystals via Na+ ion exchange.* Journal of materials science, 2017. **52**(2): p. 869-877.

86. Gupta, A., T. Sakthivel, and S. Seal, *Recent development in 2D materials beyond graphene.* Progress in Materials Science, 2015. **73**: p. 44-126.

87. Zou, W., C. Visser, J.A. Maduro, M.S. Pshenichnikov, and J.C. Hummelen, *Broadband dye-sensitized upconversion of near-infrared light.* Nature Photonics, 2012. **6**(8): p. 560.

88. Wu, D.M., A. García-Etxarri, A. Salleo, and J.A. Dionne, *Plasmon-enhanced upconversion.* The journal of physical chemistry letters, 2014. **5**(22): p. 4020-4031.

89. Hyppänen, I., S. Lahtinen, T.   ritalo, J. Mäkelä, J. Kankare, and T. Soukka, *Photon upconversion in a molecular lanthanide complex in anhydrous solution at room temperature.* ACS Photonics, 2014. **1**(5): p. 394-397.

90. Wang, Q., Q. Zhang, X. Zhao, X. Luo, C.P.Y. Wong, J. Wang, D. Wan, T. Venkatesan, S.J. Pennycook, and K.P. Loh, *Photoluminescence upconversion by defects in hexagonal boron nitride.* Nano letters, 2018. **18**(11): p. 6898-6905.

91. Tran, T.T., B. Regan, E.A. Ekimov, Z. Mu, Y. Zhou, W.-b. Gao, P. Narang, A.S. Solntsev, M. Toth, and I. Aharonovich, *Anti-Stokes excitation of solid-state quantum emitters for nanoscale thermometry.* Science advances, 2019. **5**(5): p. eaav9180.

92. Bai, G., S. Yuan, Y. Zhao, Z. Yang, S.Y. Choi, Y. Chai, S.F. Yu, S.P. Lau, and J. Hao, *2D Layered Materials of Rare-Earth Er-Doped MoS2 with NIR-to-NIR Down-and Up-Conversion Photoluminescence.* Advanced Materials, 2016. **28**(34): p. 7472-7477.

93. Li, Y., Z. Song, Z. Yin, Q. Kuang, R. Wan, Y. Zhou, Q. Liu, J. Qiu, and Z. Yang, *Investigation on the upconversion emission in 2D BiOBr: Yb3+/Ho3+*

*nanosheets.* Spectrochimica Acta Part A: Molecular and Biomolecular Spectroscopy, 2015. **150**: p. 135-141.

94. Takasugi, S., R. Iida, K. Tomita, M. Iwaoka, K. Katagiri, M. Osada, and M. Kakihana, *Synthesis of green emission upconversion phosphor nanosheets (LaNb2O7) doped with Er3+ and Yb3+.* Journal of Luminescence, 2016. **173**: p. 130-134.

95. Qing, L., Y. Xiaohong, C. Yuan, and W. Xiangfu, *Upconversion emission of SrYbF5: Er3+ nanosheets modified by Tm3+ ions.* Journal of Rare Earths, 2013. **31**(11): p. 1053-1058.

96. Ye, X., J. Chen, M. Engel, J.A. Millan, W. Li, L. Qi, G. Xing, J.E. Collins, C.R. Kagan, and J. Li, *Competition of shape and interaction patchiness for self-assembling nanoplates.* Nature chemistry, 2013. **5**(6): p. 466.

97. Shao, B., Q. Zhao, Y. Jia, W. Lv, M. Jiao, W. Lü, and H. You, *A novel synthetic route towards monodisperse β-NaYF 4: Ln 3+ micro/nanocrystals from layered rare-earth hydroxides at ultra low temperature.* Chemical Communications, 2014. **50**(84): p. 12706-12709.

98. Jung, J.H., C.-H. Park, and J. Ihm, *A rigorous method of calculating exfoliation energies from first principles.* Nano letters, 2018. **18**(5): p. 2759-2765.

99. Zong, H., X. Mu, and M. Sun, *Physical principle and advances in plasmon-enhanced upconversion luminescence.* Applied Materials Today, 2019. **15**: p. 43-57.

100. Barnes, W.L., A. Dereux, and T.W. Ebbesen, *Surface plasmon subwavelength optics.* nature, 2003. **424**(6950): p. 824.

101. Schietinger, S., T. Aichele, H.-Q. Wang, T. Nann, and O. Benson, *Plasmon-enhanced upconversion in single NaYF4: Yb3+/Er3+ codoped nanocrystals.* Nano letters, 2009. **10**(1): p. 134-138.

102. Feng, W., L.-D. Sun, and C.-H. Yan, *Ag nanowires enhanced upconversion emission of NaYF4: Yb, Er nanocrystalsvia a direct assembly method.* Chemical Communications, 2009(29): p. 4393-4395.

103. Zhang, H., D. Xu, Y. Huang, and X. Duan, *Highly spectral dependent enhancement of upconversion emission with sputtered gold island films.* Chemical Communications, 2011. **47**(3): p. 979-981.

104. Paudel, H.P., L. Zhong, K. Bayat, M.F. Baroughi, S. Smith, C. Lin, C. Jiang, M.T. Berry, and P.S. May, *Enhancement of near-infrared-to-visible upconversion luminescence using engineered plasmonic gold surfaces.* The Journal of Physical Chemistry C, 2011. **115**(39): p. 19028-19036.

105. Esteban, R., M. Laroche, and J.-J. Greffet, *Influence of metallic nanoparticles on upconversion processes.* Journal of Applied Physics, 2009. **105**(3): p. 033107.

106. Mohammadi, A., V. Sandoghdar, and M. Agio, *Gold nanorods and nanospheroids for enhancing spontaneous emission.* New Journal of Physics, 2008. **10**(10): p. 105015.

107. Giannini, V., A.I. Fernández-Domínguez, S.C. Heck, and S.A. Maier, *Plasmonic nanoantennas: fundamentals and their use in controlling the radiative properties of nanoemitters.* Chemical reviews, 2011. **111**(6): p. 3888-3912.

108. Kang, F., J. He, T. Sun, Z.Y. Bao, F. Wang, and D.Y. Lei, *Plasmonic Dual-Enhancement and Precise Color Tuning of Gold Nanorod@ SiO2 Coupled Core–Shell–Shell Upconversion Nanocrystals.* Advanced Functional Materials, 2017. **27**(36): p. 1701842.

109. Fischer, S., F. Hallermann, T. Eichelkraut, G. von Plessen, K.W. Krämer, D. Biner, H. Steinkemper, M. Hermle, and J.C. Goldschmidt, *Plasmon enhanced upconversion luminescence near gold nanoparticles–simulation and analysis of the interactions.* Optics express, 2012. **20**(1): p. 271-282.

110. Fischer, S., D. Kumar, F. Hallermann, G. von Plessen, and J.C. Goldschmidt, *Enhanced upconversion quantum yield near spherical gold nanoparticles–a comprehensive simulation based analysis.* Optics express, 2016. **24**(6): p. A460-A475.

111. Förster, T., *Zwischenmolekulare energiewanderung und fluoreszenz.* Annalen der physik, 1948. **437**(1-2): p. 55-75.

112. Dexter, D.L., *A theory of sensitized luminescence in solids.* The Journal of Chemical Physics, 1953. **21**(5): p. 836-850.

113. Liu, X. and D.Y. Lei, *Simultaneous excitation and emission enhancements in upconversion luminescence using plasmonic double-resonant gold nanorods.* Scientific reports, 2015. **5**: p. 15235.

114. Zhang, F., G.B. Braun, Y. Shi, Y. Zhang, X. Sun, N.O. Reich, D. Zhao, and G. Stucky, *Fabrication of Ag@ SiO2@ Y2O3: Er nanostructures for bioimaging: tuning of the upconversion fluorescence with silver nanoparticles.* Journal of the American Chemical Society, 2010. **132**(9): p. 2850-2851.

115. Ge, W., X. Zhang, M. Liu, Z. Lei, R. Knize, and Y. Lu, *Distance dependence of gold-enhanced upconversion luminescence in Au/SiO2/Y2O3: Yb3+, Er3+ nanoparticles.* Theranostics, 2013. **3**(4): p. 282.

116. Zhang, C. and J.Y. Lee, *Synthesis of Au nanorod@ amine-modified silica@ rare-earth fluoride nanodisk core–shell–shell heteronanostructures.* The Journal of Physical Chemistry C, 2013. **117**(29): p. 15253-15259.

117. Li, L.L., R. Zhang, L. Yin, K. Zheng, W. Qin, P.R. Selvin, and Y. Lu, *Biomimetic surface engineering of lanthanide-doped upconversion nanoparticles as versatile bioprobes.* Angewandte Chemie, 2012. **124**(25): p. 6225-6229.

118. Kannan, P., F. Abdul Rahim, R. Chen, X. Teng, L. Huang, H. Sun, and D.-H. Kim, *Au nanorod decoration on NaYF4: Yb/Tm nanoparticles for enhanced emission and wavelength-dependent biomolecular sensing.* ACS applied materials & interfaces, 2013. **5**(9): p. 3508-3513.

119. Wang, Z., W. Gao, R. Wang, J. Shao, Q. Han, C. Wang, J. Zhang, T. Zhang, J. Dong, and H. Zheng, *Influence of SiO 2 layer on the plasmon quenched upconversion luminescence emission of core-shell NaYF 4: Yb, Er@ SiO 2@ Ag nanocomposites.* Materials Research Bulletin, 2016. **83**: p. 515-521.

120. Shen, J., Z. Li, Y. Chen, X. Chen, Y. Chen, Z. Sun, and S. Huang, *Influence of SiO2 layer thickness on plasmon enhanced upconversion in hybrid Ag/SiO2/NaYF4: Yb, Er, Gd structures.* Applied Surface Science, 2013. **270**: p. 712-717.

121. Hinamoto, T., H. Takashina, H. Sugimoto, and M. Fujii, *Controlling surface plasmon resonance of metal nanocap for upconversion enhancement.* The Journal of Physical Chemistry C, 2017. **121**(14): p. 8077-8083.

122. Johnson, N.J. and F.C. van Veggel, *Lanthanide-Based Heteroepitaxial Core–Shell Nanostructures: Compressive versus Tensile Strain Asymmetry.* ACS nano, 2014. **8**(10): p. 10517-10527.

123. Qiu, H., C. Yang, W. Shao, J. Damasco, X. Wang, H. Ågren, P.N. Prasad, and G. Chen, *Enhanced upconversion luminescence in Yb3+/Tm3+-codoped fluoride active core/active shell/inert shell nanoparticles through directed energy migration.* Nanomaterials, 2014. **4**(1): p. 55-68.

124. Gee, A. and X. Xu, *Surface Functionalisation of Upconversion Nanoparticles with Different Moieties for Biomedical Applications.* Surfaces, 2018. **1**(1): p. 96-121.

125. Huang, X., *Broadband dye-sensitized upconversion: A promising new platform for future solar upconverter design.* Journal of Alloys and Compounds, 2017. **690**: p. 356-359.

126. Chen, G., J. Damasco, H. Qiu, W. Shao, T.Y. Ohulchanskyy, R.R. Valiev, X. Wu, G. Han, Y. Wang, and C. Yang, *Energy-cascaded upconversion in an organic dye-sensitized core/shell fluoride nanocrystal.* Nano letters, 2015. **15**(11): p. 7400-7407.

127. Garfield, D.J., N.J. Borys, S.M. Hamed, N.A. Torquato, C.A. Tajon, B. Tian, B. Shevitski, E.S. Barnard, Y.D. Suh, and S. Aloni, *Enrichment of molecular antenna triplets amplifies upconverting nanoparticle emission.* Nature Photonics, 2018: p. 1.

128. Zhu, X., W. Feng, J. Chang, Y.-W. Tan, J. Li, M. Chen, Y. Sun, and F. Li, *Temperature-feedback upconversion nanocomposite for accurate photothermal therapy at facile temperature.* Nature communications, 2016. **7**: p. 10437.

129. Liu, D., X. Xu, F. Wang, J. Zhou, C. Mi, L. Zhang, Y. Lu, C. Ma, E. Goldys, and J. Lin, *Emission stability and reversibility of upconversion nanocrystals.* Journal of Materials Chemistry C, 2016. **4**(39): p. 9227-9234.

130. Wu, S., Y. Ning, J. Chang, and S. Zhang, *Upconversion photoluminescence enhancement and modulation of NaYF4: Yb, Er through using different ligands.* Journal of Luminescence, 2013. **143**: p. 492-497.

131. Xue, X., S. Uechi, R.N. Tiwari, Z. Duan, M. Liao, M. Yoshimura, T. Suzuki, and Y. Ohishi, *Size-dependent upconversion luminescence and quenching mechanism of LiYF 4: Er 3+/Yb 3+ nanocrystals with oleate ligand adsorbed.* Optical Materials Express, 2013. **3**(7): p. 989-999.

132. Li, D., Q. Shao, Y. Dong, and J. Jiang, *Anomalous temperature-dependent upconversion luminescence of small-sized NaYF4: Yb3+, Er3+ nanoparticles.* The Journal of Physical Chemistry C, 2014. **118**(39): p. 22807-22813.

133. Liu, G., X. Chen, H. Zhuang, S. Li, and R. Niedbala, *Confinement of electron–phonon interaction on luminescence dynamics in nanophosphors of Er3+: Y2O2S.* Journal of Solid State Chemistry, 2003. **171**(1-2): p. 123-132.

134. UNIT, U.M.A. 2019; Available from: https://www.uts.edu.au/about/faculty-science/microstructural-analysis-unit/our-facilities.

135. Giordano, M., S. Schmid, M. Arjmandi, and M. Ramezani, *Abrasive wear of polymer fibers investigated by reciprocal scratching in an atomic force microscope.* Journal of Tribology, 2018. **140**(2): p. 021604.

136.   Qi, D.-C., W. Chen, and A.T. Wee, *NEXAFS studies of molecular orientations at molecule-substrate interfaces*. 2013, Wiley Online Library. p. 119-151.

137.   Powell, C.J. and A. Jablonski, *Consistency of calculated and measured electron inelastic mean free paths.* Journal of Vacuum Science & Technology A: Vacuum, Surfaces, and Films, 1999. **17**(4): p. 1122-1126.

138.   Tougaard, S., *QUASES-IMFP-TPP2M program.* Quases-Tougaard Inc, 2002.

139.   Moulder, J., W. Stickle, P. Sobol, and K. Bomben, *Handbook of X-ray Photoelectron Spectroscopy*. 1992.

140.   LeBlanc, G. 2008; Available from: http://archive.synchrotron.org.au/synchrotron-science/what-is-a-synchrotron.

141.   Kresse, G. and J. Furthmüller, *Efficient iterative schemes for ab initio total-energy calculations using a plane-wave basis set.* Physical review B, 1996. **54**(16): p. 11169.

142.   Perdew, J.P., K. Burke, and M. Ernzerhof, *Generalized gradient approximation made simple.* Physical review letters, 1996. **77**(18): p. 3865.

143.   Blöchl, P.E., *Projector augmented-wave method.* Physical review B, 1994. **50**(24): p. 17953.

144.   Grimme, S., J. Antony, S. Ehrlich, and H. Krieg, *A consistent and accurate ab initio parametrization of density functional dispersion correction (DFT-D) for the 94 elements H-Pu.* The Journal of chemical physics, 2010. **132**(15): p. 154104.

145.   Henkelman, G., A. Arnaldsson, and H. Jónsson, *A fast and robust algorithm for Bader decomposition of charge density.* Computational Materials Science, 2006. **36**(3): p. 354-360.

146.   Wang, F., J. Wang, and X. Liu, *Direct evidence of a surface quenching effect on size-dependent luminescence of upconversion nanoparticles.* Angewandte Chemie, 2010. **122**(41): p. 7618-7622.

147.    Chen, D. and P. Huang, *Highly intense upconversion luminescence in Yb/Er: NaGdF 4@ NaYF 4 core–shell nanocrystals with complete shell enclosure of the core.* Dalton transactions, 2014. **43**(29): p. 11299-11304.

148.    Chen, D., L. Liu, P. Huang, M. Ding, J. Zhong, and Z. Ji, *Nd3+-sensitized Ho3+ single-band red upconversion luminescence in core–shell nanoarchitecture.* The journal of physical chemistry letters, 2015. **6**(14): p. 2833-2840.

149.    Wen, S., J. Zhou, K. Zheng, A. Bednarkiewicz, X. Liu, and D. Jin, *Advances in highly doped upconversion nanoparticles.* Nature communications, 2018. **9**(1): p. 2415.

150.    Zhang, H., Y. Li, Y. Lin, Y. Huang, and X. Duan, *Composition tuning the upconversion emission in NaYF4: Yb/Tm hexaplate nanocrystals.* Nanoscale, 2011. **3**(3): p. 963-966.

151.    Wang, F. and X. Liu, *Upconversion multicolor fine-tuning: visible to near-infrared emission from lanthanide-doped NaYF4 nanoparticles.* Journal of the American Chemical Society, 2008. **130**(17): p. 5642-5643.

152.    Pichaandi, J., G.K. Das, N.J. Johnson, T. Regier, and F.C. van Veggel, *Probing the structure of NaYF4 nanocrystals using synchrotron-based energy-dependent X-ray photoelectron spectroscopy.* The Journal of Physical Chemistry C, 2014. **118**(37): p. 21639-21646.

153.    Lang, W., B. Padalia, L. Watson, D. Fabian, and P. Norris, *Multiplet structure in X-ray photoelectron spectra of rare earth elements and their surface oxides.* Faraday Discussions of the Chemical Society, 1975. **60**: p. 37-43.

154.    Yeh, J. and I. Lindau, *Atomic subshell photoionization cross sections and asymmetry parameters: 1⩽Z⩽103.* Atomic data and nuclear data tables, 1985. **32**(1): p. 1-155.

155.    Müller, C.M. and R. Spolenak, *Microstructure evolution during dewetting in thin Au films.* Acta materialia, 2010. **58**(18): p. 6035-6045.

156.  Gupta, R., M. Dyer, and W. Weimer, *Preparation and characterization of surface plasmon resonance tunable gold and silver films.* Journal of Applied Physics, 2002. **92**(9): p. 5264-5271.

157.  Worsch, C., M. Kracker, W. Wisniewski, and C. Rüssel, *Optical properties of self assembled oriented island evolution of ultra-thin gold layers.* Thin Solid Films, 2012. **520**(15): p. 4941-4946.

158.  Kracker, M., C. Worsch, C. Bocker, and C. Rüssel, *Optical properties of dewetted thin silver/gold multilayer films on glass substrates.* Thin Solid Films, 2013. **539**: p. 47-54.

159.  Li, X., D. Shen, J. Yang, C. Yao, R. Che, F. Zhang, and D. Zhao, *Successive layer-by-layer strategy for multi-shell epitaxial growth: shell thickness and doping position dependence in upconverting optical properties.* Chemistry of Materials, 2012. **25**(1): p. 106-112.

160.  Johnson, N.J., A. Korinek, C. Dong, and F.C. van Veggel, *Self-focusing by Ostwald ripening: a strategy for layer-by-layer epitaxial growth on upconverting nanocrystals.* Journal of the American Chemical Society, 2012. **134**(27): p. 11068-11071.

161.  Barr, T.L. and S. Seal, *Nature of the use of adventitious carbon as a binding energy standard.* Journal of Vacuum Science & Technology A: Vacuum, Surfaces, and Films, 1995. **13**(3): p. 1239-1246.

162.  Li, Z., S. Chen, J. Li, Q. Liu, Z. Sun, Z. Wang, and S. Huang, *Plasmon-enhanced upconversion fluorescence in NaYF4: Yb/Er/Gd nanorods coated with Au nanoparticles or nanoshells.* Journal of Applied Physics, 2012. **111**(1): p. 014310.

163.  Deng, W., L. Sudheendra, J. Zhao, J. Fu, D. Jin, I.M. Kennedy, and E.M. Goldys, *Upconversion in NaYF4: Yb, Er nanoparticles amplified by metal nanostructures.* Nanotechnology, 2011. **22**(32): p. 325604.

164.  Saboktakin, M., X. Ye, S.J. Oh, S.-H. Hong, A.T. Fafarman, U.K. Chettiar, N. Engheta, C.B. Murray, and C.R. Kagan, *Metal-enhanced upconversion*

*luminescence tunable through metal nanoparticle–nanophosphor separation.* ACS nano, 2012. **6**(10): p. 8758-8766.

165. Lu, D., S.K. Cho, S. Ahn, L. Brun, C.J. Summers, and W. Park, *Plasmon enhancement mechanism for the upconversion processes in NaYF4: Yb3+, Er3+ nanoparticles: Maxwell versus F rster.* ACS nano, 2014. **8**(8): p. 7780-7792.

166. Wu, Y., J. Xu, E.T. Poh, L. Liang, H. Liu, J.K. Yang, C.-W. Qiu, R.A. Vallée, and X. Liu, *Upconversion superburst with sub-2 µs lifetime.* Nature nanotechnology, 2019: p. 1-6.

167. Park, W., D. Lu, and S. Ahn, *Plasmon enhancement of luminescence upconversion.* Chemical Society Reviews, 2015. **44**(10): p. 2940-2962.

168. Ara jo, A., M.J. Mendes, T. Mateus, A.n. Vicente, D. Nunes, T. Calmeiro, E. Fortunato, H.   guas, and R. Martins, *Influence of the substrate on the morphology of self-assembled silver nanoparticles by rapid thermal annealing.* The Journal of Physical Chemistry C, 2016. **120**(32): p. 18235-18242.

169. Kuzma, A., M. Weis, S. Flickyngerova, J. Jakabovic, A. Satka, E. Dobrocka, J. Chlpik, J. Cirak, M. Donoval, and P. Telek, *Influence of surface oxidation on plasmon resonance in monolayer of gold and silver nanoparticles.* Journal of Applied Physics, 2012. **112**(10): p. 103531.

170. Zhang, Z. and D. Su, *Behaviour of TEM metal grids during in-situ heating experiments.* Ultramicroscopy, 2009. **109**(6): p. 766-774.

171. Liu, Y., R. Cheng, L. Liao, H. Zhou, J. Bai, G. Liu, L. Liu, Y. Huang, and X. Duan, *Plasmon resonance enhanced multicolour photodetection by graphene.* Nature communications, 2011. **2**: p. 579.

172. Shao, B., Q. Zhao, W. Lv, M. Jiao, W. Lü, and H. You, *Two-step ion-exchange synthetic strategy for obtaining monodisperse NaYF 4: Ln 3+ nanostructures with multicolor luminescence properties.* Journal of Materials Chemistry C, 2015. **3**(5): p. 1091-1098.

173. Zhang, C., H. Huang, X. Ni, Y. Zhou, L. Kang, W. Jiang, H. Chen, J. Zhong, and F. Liu, *Band gap reduction in van der Waals layered 2D materials via a de-charge transfer mechanism.* Nanoscale, 2018. **10**(35): p. 16759-16764.

174. Singh, M., E. Della Gaspera, T. Ahmed, S. Walia, R. Ramanathan, J. van Embden, E. Mayes, and V. Bansal, *Soft exfoliation of 2D SnO with size-dependent optical properties.* 2D Materials, 2017. **4**(2): p. 025110.

175. Backes, C., T.M. Higgins, A. Kelly, C. Boland, A. Harvey, D. Hanlon, and J.N. Coleman, *Guidelines for exfoliation, characterization and processing of layered materials produced by liquid exfoliation.* Chemistry of Materials, 2016. **29**(1): p. 243-255.

176. Nicolosi, V., M. Chhowalla, M.G. Kanatzidis, M.S. Strano, and J.N. Coleman, *Liquid exfoliation of layered materials.* Science, 2013. **340**(6139): p. 1226419.

177. Li, X., Z. Guo, T. Zhao, Y. Lu, L. Zhou, D. Zhao, and F. Zhang, *Filtration shell mediated power density independent orthogonal excitations–emissions upconversion luminescence.* Angewandte Chemie International Edition, 2016. **55**(7): p. 2464-2469.

178. Pin, M.W., E.J. Park, S. Choi, Y.I. Kim, C.H. Jeon, T.H. Ha, and Y.H. Kim, *Atomistic evolution during the phase transition on a metastable single NaYF 4: Yb, Er upconversion nanoparticle.* Scientific reports, 2018. **8**(1): p. 2199.

179. Wang, Y., S. Gai, N. Niu, F. He, and P. Yang, *Synthesis of NaYF4 microcrystals with different morphologies and enhanced up-conversion luminescence properties.* Physical Chemistry Chemical Physics, 2013. **15**(39): p. 16795-16805.

180. Wang, G., W. Qin, J. Zhang, L. Wang, G. Wei, P. Zhu, and R. Kim, *Controlled synthesis and luminescence properties from cubic to hexagonal NaYF4: Ln3+ (Ln= Eu and Yb/Tm) microcrystals.* Journal of Alloys and Compounds, 2009. **475**(1-2): p. 452-455.

181. Kang, J., W. Cao, X. Xie, D. Sarkar, W. Liu, and K. Banerjee. *Graphene and beyond-graphene 2D crystals for next-generation green electronics*. in *Micro-*

*and Nanotechnology Sensors, Systems, and Applications VI*. 2014. International Society for Optics and Photonics.

182. Xu, K., X. Li, P. Chen, D. Zhou, C. Wu, Y. Guo, L. Zhang, J. Zhao, X. Wu, and Y. Xie, *Hydrogen dangling bonds induce ferromagnetism in two-dimensional metal-free graphitic-C 3 N 4 nanosheets.* Chemical science, 2015. **6**(1): p. 283-287.

183. Aarts, L., B. Van der Ende, and A. Meijerink, *Downconversion for solar cells in NaYF 4: Er, Yb.* Journal of Applied Physics, 2009. **106**(2): p. 023522.

184. Berry, M.T. and P.S. May, *Disputed mechanism for NIR-to-red upconversion luminescence in NaYF4: Yb3+, Er3+.* The Journal of Physical Chemistry A, 2015. **119**(38): p. 9805-9811.

185. Yang, J.-H. and B. Yakobson, *Dimensionality-suppressed chemical doping in 2D semiconductors: the cases of phosphorene, MoS2, and ReS2 from first-principles.* arXiv preprint arXiv:1711.05094, 2017.

186. Chen, W., D. Qi, X. Gao, and A.T.S. Wee, *Surface transfer doping of semiconductors.* Progress in Surface Science, 2009. **84**(9-10): p. 279-321.

187. Charbonnière, L.J., *Bringing upconversion down to the molecular scale.* Dalton Transactions, 2018. **47**(26): p. 8566-8570.

188. Nonat, A.M. and L.J. Charbonnière, *Upconversion of light with molecular and supramolecular lanthanide complexes.* Coordination Chemistry Reviews, 2020. **409**: p. 213192.

189. Sangwan, V.K. and M.C. Hersam, *Electronic transport in two-dimensional materials.* Annual review of physical chemistry, 2018. **69**: p. 299-325.

190. Teterin, Y.A. and A.Y. Teterin, *Structure of X-ray photoelectron spectra of lanthanide compounds.* Russian Chemical Reviews, 2002. **71**(5): p. 347-381.

191. Schnellbügel, A. and R. Anton, *On background subtraction for quantitative analysis of X-ray photoelectron spectra of rare earth fluorides.* Surface science, 2001. **492**(3): p. 305-314.

192. Johnson, B., J. Klaer, S. Merdes, M. Gorgoi, B. Höpfner, A. Vollmer, and I. Lauermann, *Limitations of near edge x-ray absorption fine structure as a tool for observing conduction bands in chalcopyrite solar cell heterojunctions.* Journal of Electron Spectroscopy and Related Phenomena, 2013. **190**: p. 42-46.

193. Li, X., *Theoretical studies on electronic structure and x-ray spectroscopies of 2D materials.* 2016, KTH Royal Institute of Technology.

194. Yue, Q., Z. Shao, S. Chang, and J. Li, *Adsorption of gas molecules on monolayer MoS 2 and effect of applied electric field.* Nanoscale research letters, 2013. **8**(1): p. 425.

195. Zhao, S., J. Xue, and W. Kang, *Gas adsorption on MoS2 monolayer from first-principles calculations.* Chemical Physics Letters, 2014. **595**: p. 35-42.

196. Hudry, D., D. Busko, R. Popescu, D. Gerthsen, A.M. Abeykoon, C. K bel, T. Bergfeldt, and B.S. Richards, *Direct Evidence of Significant Cation Intermixing in Upconverting Core@ Shell Nanocrystals: Toward a New Crystallochemical Model.* Chemistry of Materials, 2017. **29**(21): p. 9238-9246.

197. Balan, A.P., S. Radhakrishnan, C.F. Woellner, S.K. Sinha, L. Deng, C. de los Reyes, B.M. Rao, M. Paulose, R. Neupane, and A. Apte, *Exfoliation of a non-van der Waals material from iron ore hematite.* Nature nanotechnology, 2018. **13**(7): p. 602.

198. Puthirath Balan, A., S. Radhakrishnan, R. Kumar, R. Neupane, S.K. Sinha, L. Deng, C.A. de los Reyes, A. Apte, B.M. Rao, and M. Paulose, *A Non-van der Waals Two-Dimensional Material from Natural Titanium Mineral Ore Ilmenite.* Chemistry of Materials, 2018. **30**(17): p. 5923-5931.

199. Dhanabalan, S.C., B. Dhanabalan, J.S. Ponraj, Q. Bao, and H. Zhang, *2D–Materials-Based Quantum Dots: Gateway Towards Next-Generation Optical Devices.* Advanced Optical Materials, 2017. **5**(19): p. 1700257.